



UNIVERSIDADE ESTADUAL DE CAMPINAS|
FACULDADE DE ENGENHARIA MECÂNICA
E INSTITUTO DE GEOCIÊNCIAS

JOSUE MAURICIO PLATA CHAVES

**MULTISCALE APPROACH TO CONSTRUCT A CARBONATE
RESERVOIR MODEL WITH KARSTIC FEATURES AND
BRAZILIAN PRE-SALT TRENDS USING NUMERICAL
SIMULATION**

**ABORDAGEM MULTI-ESCALAR PARA A CONSTRUÇÃO DE UM
MODELO DE RESERVATORIO CARBONATICO COM FEIÇÕES
CÁRSTICAS E TENDÊNCIAS DO PRÉ-SAL BRASILEIRO
USANDO SIMULAÇÃO NUMÉRICA**

CAMPINAS

2018

JOSUE MAURICIO PLATA CHAVES

**MULTISCALE APPROACH TO CONSTRUCT A CARBONATE
RESERVOIR MODEL WITH KARSTIC FEATURES AND BRAZILIAN
PRE-SALT TRENDS USING NUMERICAL SIMULATION**

**ABORDAGEM MULTI-ESCALAR PARA A CONSTRUÇÃO DE UM
MODELO DE RESERVATORIO CARBONATICO COM FEIÇÕES
CÁRSTICAS E TENDÊNCIAS DO PRÉ-SAL BRASILEIRO USANDO
SIMULAÇÃO NUMÉRICA**

Dissertation presented to the Mechanical Engineering Faculty and Geosciences Institute of the University of Campinas in partial fulfillment of requirements for the degree of Master in Petroleum Sciences and Engineering in the area of Reservoirs and management.

Dissertação apresentada à Faculdade de Engenharia Mecânica e Instituto de Geociências da Universidade Estadual de Campinas como parte dos requisitos exigidos para obtenção do título de Mestre em Ciências e Engenharia de Petróleo, na área de Reservatórios e Gestão.

Orientador: Prof. Dr. Denis José Schiozer

Este exemplar corresponde à versão final da Dissertação defendida pelo aluno Josue Mauricio Plata Chaves e orientada pelo Prof. Dr. Denis José Schiozer.

Assinatura do Orientador

CAMPINAS

2018

Agência(s) de fomento e nº(s) de processo(s): CAPES, 33003017; FUNCAMP, 2015/00371-4

Ficha catalográfica
Universidade Estadual de Campinas
Biblioteca da Área de Engenharia e Arquitetura
Rose Meire da Silva - CRB 8/5974

Plata Chaves, Josue Mauricio, 1984-
P696m

Multiscale approach to construct a carbonate reservoir model with Karstic features and Brazilian pre-salt trends using numerical simulation

/ Josue Mauricio Plata Chaves. – Campinas, SP : [s.n.], 2018.

Orientador: Denis José Schiozer.

Dissertação (mestrado) – Universidade Estadual de Campinas, Faculdade de Engenharia Mecânica.

1. Reservatórios de petróleo. 2. Reservatório (Cárbonico). 3. Reservatórios Geologia. 4. Engenharia de reservatórios. 5. Simulação computacional. I. Schiozer, Denis José, 1963-. II. Universidade Estadual de Campinas. Faculdade de Engenharia Mecânica. III. Título.

Informações para Biblioteca Digital

Título em outro idioma:

Abordagem multi-escalar para a construção de um modelo de reservatorio carbonatico com feições cársticas e tendências do pré-sal brasileiro usando simulação numérica

Palavras-chave em inglês:

Oil reservoirs

Reservoir (Cárbonico)

Geology reservoirs

Reservoir engineering

Computer simulation

Área de concentração: Reservatórios e Gestão

Titulação: Mestre em Ciências e Engenharia de Petróleo

Banca examinadora:

Denis José Schiozer [Orientador]

Regis Krueel Romeu

Emilson Pereira Leite

Data de defesa: 21-11-2018

Programa de Pós-Graduação: Ciências e Engenharia de Petróleo

UNIVERSIDADE ESTADUAL DE CAMPINAS
FACULDADE DE ENGENHARIA MECÂNICA
E INSTITUTO DE GEOCIÊNCIAS

DISSERTAÇÃO DE MESTRADO ACADÊMICO

**MULTISCALE APPROACH TO CONSTRUCT A CARBONATE
RESERVOIR MODEL WITH KARSTIC FEATURES AND BRAZILIAN
PRE-SALT TRENDS USING NUMERICAL SIMULATION**

**ABORDAGEM MULTI-ESCALAR PARA A CONSTRUÇÃO DE UM
MODELO DE RESERVATORIO CARBONATICO COM FEIÇÕES
CÁRSTICAS E TENDÊNCIAS DO PRÉ-SAL BRASILEIRO USANDO
SIMULAÇÃO NUMÉRICA**

Autor: Josue Mauricio Plata Chaves
Orientador: Prof. Dr. Denis José Schiozer

A Banca Examinadora composta pelos membros abaixo aprovou esta Dissertação:

Prof. Dr. Denis José Schiozer, Presidente
DE / FEM / UNICAMP

Prof. Dr. Emilson Pereira Leite
DGRN / IG / UNICAMP

Dr. Regis Kruel Romeu
PETROBRAS

A ata da defesa com as respectivas assinaturas dos membros encontra-se no processo de vida acadêmica do aluno.

Campinas, 21 de novembro de 2018.

DEDICATION

To my parents, Blanca and Josué, my sister Diana, my brother Vladimir and his family.

To Larissa Silva.

ACKNOWLEDGMENTS

I want to thank my advisor Denis Schiozer for providing me the support and guidance during my research.

To Manuel Gomes Correia for the guidance during the development of this work.

I also want to thank my colleagues, DEP, UNISIM and CEPETRO for the assistance and contributions.

To CAPES and FUNCAMP for the financial support.

All my friends for the special moments shared.

RESUMO

PLATA, Josue Mauricio, *Abordagem multiescalar para a construção de um modelo de reservatório carbonático com feições cársticas e tendências do pré-sal brasileiro usando simulação numérica*, Campinas, Faculdade de Engenharia Mecânica, Universidade Estadual de Campinas, 2018. --- p. Dissertação (Mestrado)

O pré-sal brasileiro é formado principalmente por carbonatos nos quais podem ocorrer cenários de desenvolvimento cárstico. Este tipo de reservatório apresenta um desafio para modelagem e simulação de fluxo, dado seu comportamento multiescalar heterogêneo. O uso de abordagens hierárquicas multiescalar tem mostrado ser útil para representar heterogeneidades em reservatórios complexos. Metodologias relacionadas ao gerenciamento de reservatórios podem ser testadas em modelos sintéticos de reservatórios. No presente trabalho, apresentamos a elaboração de um modelo sintético de reservatório com características do pré-sal brasileiro e feições cársticas, baseado em uma abordagem hierárquica de transferência de escala. O método integra modelagem e transferência de escala entre malhas que possuem diferentes tamanhos de bloco e geometria. O modelo geológico de campo completo, denominado Lira-G, é gerado pela combinação de dois modelos denominados Lira-M e Lira-K. O modelo Lira-M tem as mesmas dimensões de bloco que Lira-G e representa a simulação estocástica de saída usando dados de perfil de dois poços. O Lira-K tem uma resolução maior, os carstes são heterogeneidades em pequena escala além da escala dos blocos Lira-M. O procedimento de transferência de escala foi ajustado através de simulação de fluxo. O processo de validação mostrou a influência das feições cársticas na recuperação no comportamento dinâmico. Usando pseudo-curvas foi possível combinar os dados dinâmicos de produção. Finalmente, Lira-G é transferido para uma malha mais grossa, chamada Lira-S para ser usado em simulação numérica de fluxo.

Este trabalho contribuiu com uma abordagem hierárquica de transferência de escala para construir um modelo geológico cárstico, integrando modelagem e simulação de reservatório.

O modelo proposto Lira-G, acrescenta uma oportunidade para ser utilizado como modelo de referência numa proposta de *benchmark* para avaliar e comparar diferentes metodologias com foco em transferência de escala e simulação numérica de reservatórios.

Palavras-Chave: Reservatórios cársticos, reservatórios carbonáticos, transferência de escala, reservatórios do pré-sal.

ABSTRACT

PLATA, Josue Mauricio, *Multiscale approach to construct a carbonate reservoir model with karstic features and Brazilian pre-salt trends using numerical simulation*, Campinas, Faculdade de Engenharia Mecânica, Universidade Estadual de Campinas, 2018. --- p. Dissertação (Mestrado)

The Brazilian pre-salt is formed mainly by carbonates in which karstic development scenarios can occur. This type of reservoir presents a challenge for modeling and flow simulation given its heterogeneous multiscale behavior. The use of hierarchical upscaling approach has shown to be useful to represent heterogeneities in complex reservoirs.

Methodologies regarding reservoir management can be tested in synthetic reservoir models. In this work, we present the elaboration of a synthetic reservoir model with Brazilian pre-salt characteristics and karst features, based on a hierarchical upscaling approach. The method integrates modeling and scale transfer between grids with different block sizes and geometry. The full field geological model, called Lira-G, is generated by combining two models, Lira-M and Lira-K. Lira-M has the same cell dimensions as Lira-G and represents the output stochastic simulation using well log data. Lira-K has a finer cell resolution; karsts are small-scale heterogeneities beyond the Lira-M cell. The upscale procedure was validated using flow simulation. The validation process showed the influence of karst features in recovery and dynamic behavior. By using pseudo-curves, it was possible to match the dynamic production data. Finally, Lira-G is upscaled to a coarser grid, called Lira-S, to be used in numerical flow simulation.

This work contributed to a hierarchical upscaling approach to construct a karstic geological model, integrating modeling and reservoir simulations. The proposed model provides an opportunity to be used as a *benchmark* to evaluate and compare different methodologies regarding upscaling procedures and reservoir numerical simulation.

Key Word: Karstic reservoir, carbonate reservoir, upscaling, pre-salt reservoirs.

LIST OF FIGURES

Figure 2.1. Basic porosity types in carbonates. After Choquette and Pray, 1970.	23
Figure 2.2 Undergroud karstic system (Loucks., 1999).	24
Figure 2.3 Cave passage (left) and collapsed cave (right). From Loucks, 1999	26
Figure 2.4 Near surface cave geometries of single and multiple passage shown in plan view. From Loucks, 1999.....	27
Figure 2.5 Conceptual porosity-permeability relationship for matrix and non-matrix features. From Medekenova and Jones., 2014.	28
Figure 2.6 Upscaling process.	28
Figure 3.1 Example of facies present in the Santos Basin. (Salamoni, et al., 2010), (Petersohn et al., 2013).	30
Figure 3.2 Main trend of fractures and their role in development of mega-karst. From Carneiro et al., 2015.	33
Figure 3.3 UNISIM-I (left) and UNISIM-II (right) geological synthetic models to benchmark proposals.	35
Figure 4.1 Summary of the methodology.	37
Figure 4.2 Workflow for generating Lira M	39
Figure 4.3 Workflow for generating Lira K.	40
Figure 5.1 Creation of surfaces based on maps of boundary of formations.....	43
Figure 5.2 Creation of fault model based on images of interpreted seismic profiles	43
Figure 5.3 Zig-zag faults (left) and layers following the base (right) in the structural model of Lira-M.....	44
Figure 5.4 Lira-M structural model.	44
Figure 5.5 Facies from composite log and upscaled in a segment of Lira-1 and Lira-2 wells.	45
Figure 5.6 Distribution of facies used as input for Truncated Gaussian simulation.	46
Figure 5.7 Upscale of porosity and permeability from well log to grid, in a segment of Lira-1.	47
Figure 5.8 Definition of the Lira-K grid in relation to Lira-M.....	49
Figure 5.9 Definition of main lineaments for Lira-K, in red dotted lines.	50
Figure 5.10 Workflow for karst distribution modeling.	51
Figure 5.11 Downscaled of permeability from Lira-M to Lira-K, in a horizontal (left) and vertical (right) view.	51
Figure 5.12 Porosity and permeability models in Lira-K.....	52
Figure 5.13 Integration of upscaled Lira-K and Lira-M into Lira-G.....	53
Figure 5.14 Selected zones for validate Lira-G. Top: Zone 2; bottom: Zone 3. Example for Permeability.....	54

Figure 5.15 Karts system continuous in a whole block at Lira-K scale.....	55
Figure 5.16 Relative permeability curves for RT=1 and RT=2 in Lira-K.....	56
Figure 5.17 Comparison of cumulative oil production in Lira-K and Lira-G using the same relative permeability curve for RT=2	56
Figure 5.18 Determination of the RT percentage of the Lira-K contained in the blocks RT = 2 in Lira-G	58
Figure 5.19 Relative permeability pseudo-curve used for RT=2 in Lira-G.	58
Figure 5.20 Comparison of cumulative oil production between Lira-K and Lira-G using the pseudo-curve of relative permeability for RT=2 in Lira-G	59
Figure 5.21 Relative permeability curve used in Lira-S for Zone 1	60
Figure 5.22 Relative permeability curves used in Lira-S for Zone 2	60
Figure 5.23 Relative permeability curves used in Lira-S for Zone 3	60
Figure 6.1 Facies model in Lira-M.....	62
Figure 6.2 Crossplot of porosity and permeability by facies for Zone 1 in Lira-M.....	63
Figure 6.3 Crossplot of porosity and permeability by facies for Zone 2 in Lira-M.....	63
Figure 6.4 Crossplot of porosity and permeability by facies for Zone 3 in Lira-M.....	63
Figure 6.5 Cross section showing the facies, porosity and permeability of Lira-M in Zone 1	64
Figure 6.6 Cross section showing the facies, porosity and permeability of Lira-M in Zone 2	64
Figure 6.7 Cross section showing the facies, porosity and permeability of Lira-M in Zone 3	65
Figure 6.8 Grid of lira-K developed in Zone 2 and Zone 3.....	66
Figure 6.9 Lira-K porosity and permeability model in Zone 2	66
Figure 6.10 Porosity and permeability histograms for Zone 2 of Lira-K.....	66
Figure 6.11 Facies distribution in karst system for Zone 3 of Lira-K.....	67
Figure 6.12 Porosity and permeability histograms for Zone 3 of Lira-K.....	67
Figure 6.13 RT=2 upscaled from Lira-K to Lira-G in Zone 2	68
Figure 6.14 RT=2 upscaled from Lira-K to Lira-G in Zone 3	68
Figure 6.15 Porosity histograms for Lira-K and Lira-G in zones 2 and 3.....	69
Figure 6.16 Comparison of porosity between Lira K and Lira-G RT=1 (left) and Lira-G RT=2 (right) in Zone 2.....	69
Figure 6.17 Comparison of porosity between Lira K and Lira-G RT=1 (left) and Lira-G RT=2 (right) in Zone 3.....	70
Figure 6.18 Permeability histograms for Lira-K and Lira-G in zones 2 and 3.....	70
Figure 6.19 Comparison of permeability between Lira K and Lira-G RT=1 (left) and Lira-G RT=2 (right) in Zone 2.	70
Figure 6.20 Comparison of permeability between Lira K and Lira-G RT=1 (left) and Lira-G RT=2 (right) in Zone 3.	71
Figure 6.21 Crossplot of porosity and permeability by rock type in validation zones 2 and 3 in Lira-G.	71

Figure 6.22 NS cross section of Lira-G showing karstic influence in Zone 2	72
Figure 6.23 NS cross section of Lira-G showing karstic influence in Zone 3	72
Figure 6.24 Flow simulation on the Lira-K in Zone 2.....	73
Figure 6.25 Flow simulation on the Lira-K in Zone 3.....	74
Figure 6.26 Reservoir pressure, oil production, water cut and oil rate comparing the Lira-K and Lira-G in Zone 2 after validation.....	75
Figure 6.27 Reservoir pressure, oil production, water cut and oil rate comparing the Lira-K and Lira-G in Zone 3 after validation.....	75
Figure 6.28 Comparison of water saturation between Lira-K and Lira-G in Zone 2 at six months of simulation.	76
Figure 6.29 Comparison of water saturation between Lira-K and Lira-G in Zone 2 at five years of simulation	76
Figure 6.30 Comparison of water saturation between Lira-K and Lira-G in Zone 2 at ten years of simulation.....	77
Figure 6.31 Comparison of water saturation between Lira-K and Lira-G in Zone 3 at six months of simulation	77
Figure 6.32 Comparison of water saturation between Lira-K and Lira-G in Zone 3 at five years of simulation	78
Figure 6.33 Comparison of water saturation between Lira-K and Lira-G in Zone 3 at ten years of simulation.....	78
Figure 6.34 Oil production and water cut comparing production wells adjust in Lira-K and Lira-G in Zone 2 after validation.....	79
Figure 6.35 Oil production and water cut comparing production wells adjust in Lira-K and Lira-G in Zone 2 after validation.....	79
Figure 6.36 Oil production and water cut comparing production wells adjust in Lira-K and Lira-G in Zone 3 after validation.....	80
Figure 6.37 Oil production and water cut comparing production wells adjust in Lira-K and Lira-G in Zone 3 after validation.....	80
Figure 6.38 Porosity histograms comparing Lira-G and Lira-S in a region with karst influence in zones 2 and 3.	81
Figure 6.39 Permeability histograms comparing Lira-G and Lira-S in a region with karst influence in zones 2 and 3.	81
Figure 6.40 Comparison of porosity between Lira G and Lira-S RT=1 (left) and Lira-S RT=2 (right) in Zone 2.....	82
Figure 6.41 Comparison of porosity between Lira G and Lira-S RT=1 (left) and Lira-S RT=2 (right) in Zone 3.....	82
Figure 6.42 Comparison of porosity between Lira G and Lira-S RT=1 (left) and Lira-S RT=2 (right) in Zone 2.....	82
Figure 6.43 Comparison of porosity between Lira G and Lira-S RT=1 (left) and Lira-S RT=2 (right) in Zone 3.....	83
Figure 6.44 Porosity model in Lira-G and Lira-S	83

Figure 6.45 Horizontal permeability model in Lira-G and Lira-S	83
Figure 6.46 Vertical permeability model in Lira-G and Lira-S.....	84
Figure 6.47 NTG model in Lira-G and Lira-S.....	84
Figure 6.48 Porosity of full field Lira-G and Lira-S by zone.....	85
Figure 6.49 Permeability of full field Lira-G and Lira-S by zone.....	85
Figure 6.50 Cross section showing the RT, porosity and permeability of Lira-S in Zone 1....	86
Figure 6.51 Cross section showing the RT, porosity and permeability of Lira-S in Zone 2....	87
Figure 6.52 Cross section showing the RT, porosity and permeability of Lira-S in Zone 3....	87
Figure 6.53 Comparison of oil production, oil production rate, water cut and reservoir pressure between Lira-G and Lira-S in Zone 1 after validation.	88
Figure 6.54 Comparison of oil production, oil recovery factor, water cut and reservoir pressure between Lira-G and Lira-S in Zone 2 after validation.	89
Figure 6.55 Comparison of oil production, oil recovery factor, water cut and reservoir pressure between Lira-G and Lira-S in Zone 3 after validation	89
Figure 6.56 Comparison of water saturation between Lira-G and Lira-S in Zone 1 at ten years of simulation.	90
Figure 6.57 Comparison of water saturation between Lira-G and Lira-S in Zone 1 at thirty years of simulation	90
Figure 6.58 Comparison of water saturation between Lira-G and Lira-S in Zone 2 at ten years of simulation.....	91
Figure 6.59 Comparison of water saturation between Lira-G and Lira-S in Zone 2 at thirty years of simulation	91
Figure 6.60 Comparison of water saturation between Lira-G and Lira-S in Zone 3 at ten years of simulation.....	92
Figure 6.61 Comparison of water saturation between Lira-G and Lira-S in Zone 3 at thirty years of simulation	92
Figure 6.62 Oil production and water cut comparing production wells adjust in Lira-G and Lira-S in Zone 2 after validation.	93
Figure 6.63 Oil production and water cut comparing production wells adjust in Lira-G and Lira-S in Zone 2 after validation.	93
Figure 6.64 Oil production and water cut comparing production wells adjust in Lira-G and Lira-S in Zone 3 after validation.	94
Figure 6.65 Oil production and water cut comparing production wells adjust in Lira-G and Lira-S in Zone 3 after validation.	94
Figure 6.66 Influence of karsts features on the water advance in Lira-G, Zone 2 at ten years of simulation	95
Figure 6.67 Influence of karsts features on the water advance in Lira-G, Zone 2 at twenty years of simulation	95
Figure 6.68 Influence of karsts features on the water advance in Lira-S, Zone 2 at ten years of simulation	96

Figure 6.69 Influence of karsts features on the water advance in Lira-S, Zone 2 at thirty years
of simulation96

LIST OF TABLES

Table 2.1 Classification of carbonate rocks in Brazilian basins. Summary of Salamoni, et al. 2010.	23
Table 3.1 Briefly description of the interest formations present in the Santos Basin	29
Table 5.1 Summary of Lira models	42
Table 5.2. Fault transmissibility multipliers.	44
Table 5.3 Parameters used in generation of porosity model in Lira-M.....	47
Table 5.4 Parameters used in generation of permeability model in Lira-M.....	48
Table 5.5 Vertical permeability multiplier calculated by zone	48
Table 5.6 Summary of parameters for karst object modeling	50
Table 5.7 Petrophysical properties assigned for karst modeling	52
Table 5.8 Rock-fluid properties and parameters of validation model	55
Table 6.1 Comparison of zones selected for validation of Lira-G	74
Table 6.2 Volume comparison between Lira-G and Lira-S	86
Table 6.3 Pore volume comparison between Lira-G and Lira-S in validation regions of zones 1, 2 and 3.	88

SUMMARY

1	INTRODUCTION	18
1.1	Motivation	20
1.2	Objectives	21
2	THEORETICAL FOUNDATION	22
2.1	Carbonates: Formation and composition	22
2.2	Classification of carbonate rocks	22
2.3	Petrophysical classification	23
2.4	Karst and karstification	24
2.4.1	Spatial distribution	25
2.4.2	Cave	26
2.4.3	Petrophysical of mega-karst	27
2.5	Multiscale heterogeneities	27
3	LITERATURE REVIEW	29
3.1	Brazilian pre-Salt	29
3.2	Karstified carbonate reservoirs	31
3.3	Hierarchical multiscale approaches	33
3.4	Benchmark cases	34
4	METHODOLOGY	36
4.1	Lira-M	37
4.2	Lira-K	38
4.2.1	Lira-G	40
4.2.2	Validation of Lira-G	41

4.3	Lira-S.....	41
4.3.1	Validation of Lira-S	41
5	APPLICATION.....	42
5.1	Lira-M	42
5.1.1	Structural model	43
5.1.2	Facies model	44
5.1.3	Petrophysical model.....	46
5.2	Lira-K.....	48
5.2.1	Facies Model	49
5.2.2	Petrophysical model.....	51
5.3	Generation of LIRA-G.....	52
5.4	Validation of Lira-G.....	53
5.4.1	Simulation in Lira-K.....	54
5.4.2	Flow adjustment.....	56
5.5	Upscale to Simulation grid Lira-S	57
5.5.1	Validation of Lira-S	59
6	RESULTS AND DISCUSSIONS.....	62
6.1	Lira-M	62
6.2	Lira-K.....	65
6.3	Lira-G.....	67
6.4	Validation of LIRA-G.....	73
6.4.1	Simulation in Lira-K.....	73
6.4.2	Flow adjustment.....	74
6.5	Lira-S.....	81

6.5.1 Validation of Lira-S	88
7 CONCLUSIONS.....	98

1 INTRODUCTION

Carbonate reservoirs are considered to be very complex, given the development of structures at different scales due the dissolution and diagenesis which affect the reservoir properties. A product of these processes is the development of karst, an environment with an underground drainage system that forms due to the great solubility in water of certain rock (Simms, 2005). In a karst reservoir, a spectrum of voids, ranging in scale from vugs to caves, dynamically communicate with a rock matrix (Jones, 2015). When forming, the drainage system involves fluids that can enhance preexisting permeability networks or can reduce them. Karst features can be divided broadly into two types: (1) micro-karst associated with vuggy pore throats in excess of 10-20 mm and (2) mega-karst, describing conduits and caves above 30 cm aperture (Trice, 2005). This work focuses on representing mega karst features.

Ion dissociation is the basic process of karst dissolution. Secondary permeability supports their development (Simms, 2005). Karst structures can occur along different structural patterns related to the main trend of fractures that allow fracture concentration and dissolution development (Carneiro et al, 2015) and also can be associated with subaerial exposure surfaces (Lucia, 2007).

Observations on subsurface karst reservoir lack detail due the low resolution of seismic images and the limited lateral coverage of well observations (Loucks, 2001). According to Medekenova and Jones (2014), to detail a karst image at the seismic scale is required a large population of sub-seismic scale features. A significant scale gap between these seismic and well scales generates uncertainty in the characterization at intermediate scales (Strijker, et al 2012). However, the use of conceptual models, outcrop analogs and cave maps provide essential trends for karst modeling (Jones, 2015; Medekenova and Jones, 2014; Neillo et al., 2014; Loucks, 1999).

Property data collection associated with karst features is challenging. Permeability in karsts is highly uncertain and cannot be measured in the laboratory. Medekenova and Jones (2014) presented a general distribution of porosity and permeability for non-matrix features in carbonates where they predicted a higher permeability of karst blocks when compared to fracture dominated blocks.

The use of hierarchical scale approaches helps to model complex and heterogeneous carbonated reservoirs. Works such as those of Strijker et al., (2012), Gomez et al., (2015), and

Mikes et al., (2006) show the usefulness of the multiscale approach to represent heterogeneities at different scales.

Several methodologies regarding reservoir management can be tested in synthetic models with characteristics of real reservoirs in the absence of a real geological field model. Synthetic models have been used as reference models in *benchmark* proposals (Avansi and Schiozer 2015; Correia et al., 2015) which provided the opportunity to evaluate methodologies about oil exploitation strategies and reservoir development.

Pre-Salt reservoirs in the Santos Basin, Brazil are important recent oil discoveries, composed mainly of carbonated formations with great potential for accumulation of hydrocarbons. There is an increasing interest in these reservoirs related to the challenges during modeling, development, and production forecasting. Pre-salt formations can be associated with events related to karst development, such as the presence of carbonate rocks, faulting, and stratigraphic discontinuity surfaces. Thus, we propose a synthetic geological model of a field with karstic features development. In a global way, this synthetic model introduces the pre-salt fields as the information of two wells, including facies and porosity. Permeability logs from two fields in the Santos Basin were used for its elaboration. Additionally, maps of surface formations and images of faults for a field in the Santos Basin were also used. Part of the information is supplied by the national oil and gas bio-fuels agency - ANP, and another part is public access.

As this model is a combination of depositional matrix with karst features, two models are developed and combined into a full geological model. The first model represents the depositional matrix without the influence of karst, and is based on the logs from two wells. The second model represents the karst distribution. The trends for karst modeling are based on the regional structural framework, represented by the orientation of faults and fractures in the field. The karsts are populated using object modeling technique constrained to the orientation, width, height, and length of the karst.

The scale of heterogeneities is a function of the simulation grid block (Bourbiaux, 2010). The scale hierarchy depends on the full model dimension as the number of blocks affects the computer performance. The block size of the full field model proposed in this work is above the dimension of karst, particularly in width and length. Decreasing the block volume in full field model represents an increase in the number of blocks generated, which would be undesirable given the dimensions of the complete field. The karst model has a higher resolution than the full field model because of karst scale.

In this work we follow a workflow that integrates modeling with hierarchical upscaling, integrating two grid sizes: (1) a refined grid for karst model and (2) a full field geological grid. The synthetic full field generated is then upscaled to a coarser simulation grid due to computational limitations and flow simulators limitation. The reduction of time consumed in simulations is essential for the analysis of uncertainties, given the high number of realizations required (Correia, 2014). The process of upscaling between models is validated by flow simulation, first creating a reference response in the fine model and then adjusting the response of the coarse model with the reference model. The hierarchical scale approach enables sequential control over statics and dynamics results during upscaling procedures (Correia et al., 2015).

The synthetic geological model created can be used as a reference model with a known response, from which to generate simulation models to test, compare and validate methodologies of reservoir management during different phases of field development.

1.1 Motivation

Brazilian pre-salt reservoirs are a recent oil discovery which represents a great opportunity for research development related to stages of field modeling, development and production forecasting. The methodologies related to reservoir management applications can be tested in synthetic models with characteristics of real reservoirs. The increasing interest in pre-salt reservoirs creates the need to generate synthetic models that represent the geological characteristics in the pre-salt. The development of karst features is possible, that would generate heterogeneities at different scales.

The use of hierarchical upscaling approaches has shown to be useful to model complex and heterogeneous reservoirs (Gomez et al., 2015; Strijker et al., 2012; Jones, 2015, Mikes et al., 2006). The methods are meaningful when they are connected to the underlying geological controls (Strijker, 2012). Conceptual models, outcrop analogs and cave maps add essential trends to karstic modeling (Jones, 2015; Medekenova and Jones, 2014; Neillo et al, 2014; Loucks, 1999). An integrated application of these two approaches can be useful to generate accurate synthetic models considering multiscale heterogeneities, as is the case of karstic reservoirs.

The absence of synthetic models of a carbonate reservoir regarding the development of karst features which present a petrophysical behavior close to Brazilian pre-salt encourages this work. The model created can be used as a reference to evaluate different challenges related to reservoir development that may be close to those present in the Brazilian pre-salt. This adds an

opportunity for developing research regarding Brazilian pre-salt reservoirs, associated to karstic environments.

1.2 Objectives

The purpose of this work is to build a synthetic reservoir model based on a hierarchical upscaling approach, which represents a (1) a carbonate reservoir with Brazilian pre-salt trends and (2) karstic features. This model is built to be used as a reference model in future works regarding reservoir simulation and reservoir management approaches so, uncertainty modelling approach is not addressed in this work.

To support this, we apply a multiscale approach to combine heterogeneities at different scales and conceptual models to help in modeling with limited information.

The following tasks are developed:

- Build a geological and petrophysical model based on well log data that represent Brazilian pre-salt reservoirs (Lira-M).
- Create a model of karst distribution and petrophysical properties (Lira-K).
- Generate the full field geological model that integrates the information from Lira-M and Lira-K models (Lira-G).
- Upscale of Lira-G to a coarser grid and validate to use in flow simulation (Lira-S).

2 THEORETICAL FOUNDATION

This chapter describes the necessary concepts for generating the understanding and development of the work.

2.1 Carbonates: Formation and composition

Carbonate rocks are composed of more than 50% carbonate minerals, mainly calcite and dolomite. The main components of most modern carbonate sediments are bioclastic skeletal grains, ooids and other subrounded grains, intraclast, carbonate mud and cement.

There are carbonate rocks that are formed by transport and deposition of carbonate particles, as happens with siliciclastic rocks. Others can be formed in situ by the growth of skeletons or by microbial mats that trap and bind sediment. They can display a range of primary and secondary sedimentary structures (laminations, cross-bedding, graded bedding, bioturbation) or the structures may be absent. They also can show others structures that are strongly related to carbonate rocks, including vugs and cavities, hardgrounds, paleokarst surfaces, stromatolites and framework reef structures (Stow, 2005).

2.2 Classification of carbonate rocks

There are many classification schemes for carbonate rocks. Folk (1962) presents a compositional classification, distinguishing three principal components: allochems, matrix, and cement. Dunham (1962) presents a classification based on depositional texture (matrix-grain relationship). Various other classifications were proposed after these two classifications of Folk and Dunham, such as the classification of Embry and Klovan in 1971, for bio-constructed carbonates and the Riding (2000) classification proposed exclusively for microbial carbonates. Salamoni, et al. 2010 proposed a new classification of carbonate rocks to cover the entire spectrum of their occurrence in Brazilian basins. The carbonate rocks were divided into four groups according to their depositional texture. Table 2.1 shows a summary. The details are in Salamoni, et al. 2010.

Table 2.1 Classification of carbonate rocks in Brazilian basins. Summary of Salamoni, et al. 2010.

Depositional texture	Nomeclature [English]	Nomenclature [Portuguese]	Depositional texture	Nomeclature [English]	Nomenclature [Portuguese]
Components not bounding during formation	Mudstone	Mudstone	Original components bound together during formation - In situ	Boundstone	Boundstone
	Wackestone	Wackestone		Stromatolite	Estromatolito
	Packstone	Packstone		Thrombolite	Trombolito
	Grainstone	Grainstone		Dendrolite	Dendrolito
	Floatstone	Floatstone		Leiolite	Leiolito
	Rudstone	Rudstone		Spherulite	Esferulito
	Bioaccumulated	Bioacumulado		Travertine	Travertino
	Breccia	Brecha	Unrecognizable original texture	Crystalline limestone	Calcário cristalino
Laminite	Laminito	Dolomite		Dolomito	

2.3 Petrophysical classification

The petrophysical classification describes the relationship between carbonate rock fabrics and petrophysical properties. Choquette and Pray, 1970, presented a classification that highlights the incidence of the genesis of the porous space, dividing it into selective and non-selective porous space. Selective texture includes intergranular, intercrystalline, intraparticle and moldic porosity. The non-selective pore textures include fractures and cavities of varying sizes (vugs, caverns) (Figure 2.1). Lucia (2007) classified the vugular pore space by dividing it into connected or touching (fractures and caverns) and, separated vugular space.

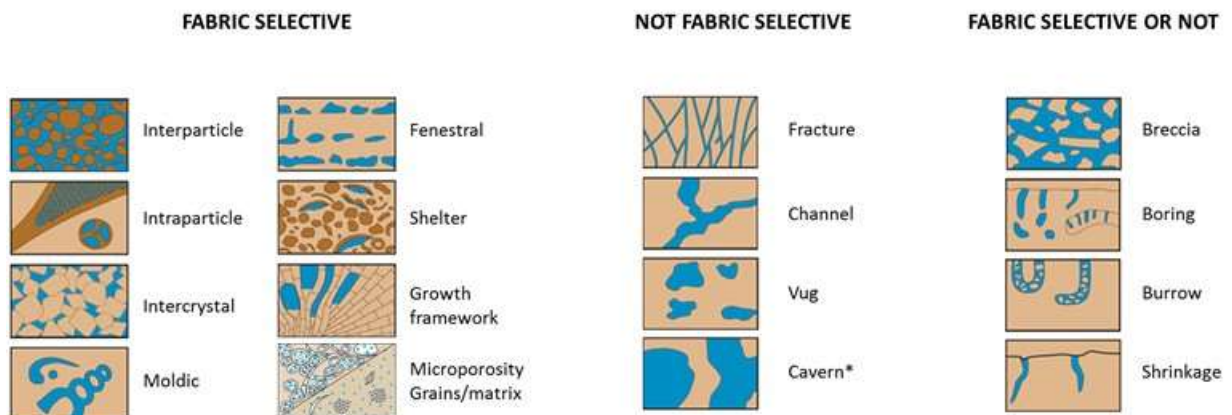


Figure 2.1. Basic porosity types in carbonates. After Choquette and Pray, 1970.

2.4 Karst and karstification

The term karst is applied to an environment with an underground drainage system that grows up due the solubility in water of certain rock types, particularly limestone (Simms, 2005) (Figure 2.2).

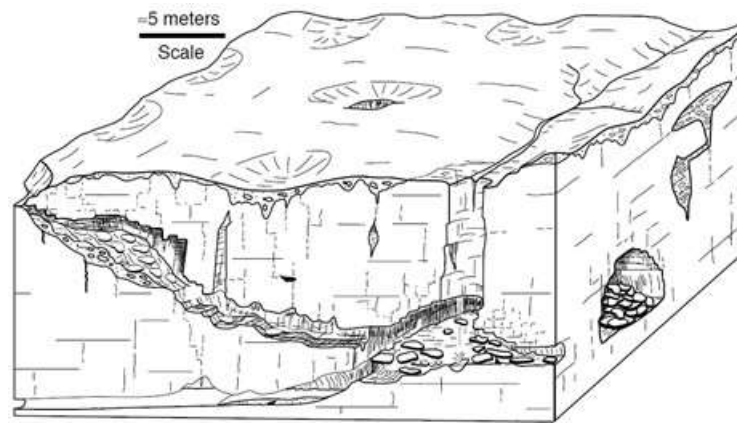


Figure 2.2 Underground karstic system (Loucks., 1999).

The basic process of karst dissolution is related to ion dissociation. A common product in this environment is cave development. The near-surface process (epigenetic) is driven by the hydrologic cycle. Water readily absorbs CO_2 from the atmosphere and soil to form carbonic acid, which infiltrates and reacts with carbonate. Between the earth's surface and the underground water table, the pore space is partially saturated with air. This zone is called the vadose zone. Flow in this zone occurs during rainfall and flooding and is focused at fracture intersections dominantly in a downward direction. Below the water table, in the phreatic zone, the pore space is saturated with water. Flow in this zone can be lateral and downward and is focused along fractures and dissolved passageways. The location of the boundary of these two zones is not constant, it moves up and down based on the water recharge. Dissolution is focused in the vadose, high phreatic and mixing zones. There are also other types of karst that were probably dissolved by sulfuric acid derived from deep crustal sources by upwelling flow and they are known as hypogenic karst (Klimchouk et al, 2016).

When forming, the system involves fluids that can enhance preexisting permeability networks by dissolution and mechanical erosion or can reduce them by sedimentation and cementation (Trice, 2005).

A karstic carbonate reservoir is characterized by a spectrum of voids, ranging in scale from vugs to caves dynamically communicate with a variety of matrixes (Jones, 2015). Karst features can be divided broadly into two types: (1) micro-karst associated with vuggy pore throats in excess of 10-20 mm, and (2) mega-karst describing karst products that include

conduits and caves above 300 mm aperture (Trice, 2005). This work is focused on mega-karst modeling.

2.4.1 Spatial distribution

Massive dissolution creates large, connected voids called as touching vugs. The geometry of touching-vug pore space system in the karst development environment is controlled by preexisting tectonic fracture patterns (Lucia, 2007). Depositional textures have little control over the distribution of large-scale karst dissolution. A good secondary permeability supports the development of karst because it assists the drainage into specific conduits through the rock (Simms, 2005). Cave maps commonly show that fracture system, faults, and joints have a strong control over cave geometry development (Lucia, 2007; Klimchouk et al, 2015). Subaerial exposure surfaces can also be directly associated with karst development, acting as points of entry of water into the underground system. However, the cavern can be formed hundreds of feet below the underground system (Lucia, 2007). Karst structures can occur along different structural patterns related to the main trend of fractures. These structural patterns allow the fracture concentration and karst dissolution development (Carneiro et al., 2015; Lucia, 2007). Some of this arrangements are the interconnection of fractures, the center and termination of fractures, dendritic, and mixed pattern.

Observations on subsurface karst reservoir lack in detail due the low resolution of seismic images and the limited lateral coverage of well observations (Loucks, 2001).

From seismic modeling only the largest karst features or stacked series of smaller karst features can be imaged and identified as structural lineaments with a seismic amplitude anomaly (Medekenova and Jones., 2014; Neilo et al., 2014). According to Medekenova and Jones (2014), a large population of sub-seismic scale features is required to detail a karst image at a seismic scale. At well bore scale, the description of the porous medium in dissolution features can be made from cores and borehole images. The most significant dissolution features are: (1) vugs, (2) caverns from centimeter to decimeter size, (3) conduits as tube-like elongated, in some cases horizontal cavities, and (4) collapsed breccias (Neilo et al.,2014). The image log description can be used qualitatively to provide geometries and abundance of dissolution features at well scale.

A significant scale gap between these seismic and well scales generates uncertainty in the characterization at intermediate scales (Strijker, et al 2012). However, the use of conceptual models, outcrop analogs and cave maps provide essential trends for karst modeling (Jones, 2015; Medekenova and Jones, 2014; Neillo et al, 2014; Loucks, 1999)

2.4.2 Cave

A cave passage is the cavernous conduit, including his adjacent wall and ceiling rocks (Figure 2.3). It can be a simple passage or be composed of multiple passages (Loucks, 1999; Xinbian, 2014) (Figure 2.4). Karst can be of the order of 2-4% bulk volume of host rock with some cases varying up to 10% (Trice, 2015).

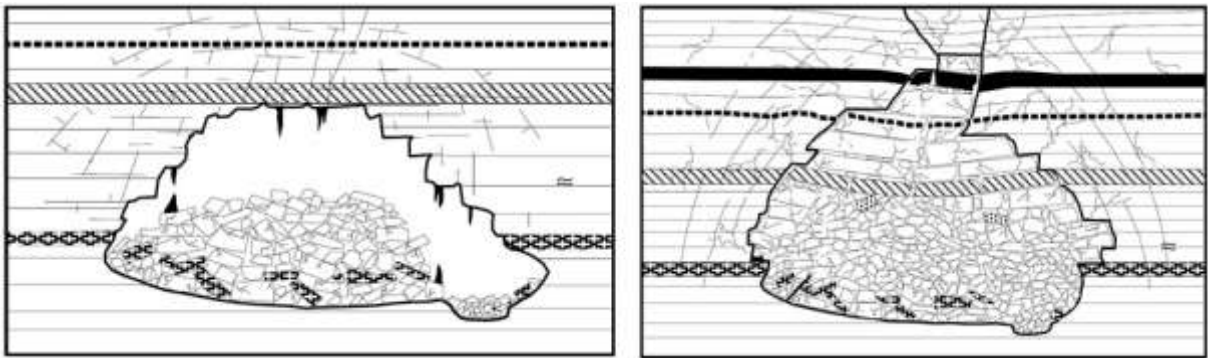


Figure 2.3 Cave passage (left) and collapsed cave (right). From Loucks, 1999

The collapse of caves is an integral part of karst evolution. Cave ceilings and walls are under stress from the weight of overlying strata making collapsing the remaining cave passages (Figure 2.3 right) (Loucks, 1999). Major products of collapse evolution are crackle breccia, chaotic breccia, and cave sediment. There are cavern systems that did not collapse and were kept as open (Figure 2.3 left). These structures are interpreted indirectly by severe mud losses and bit drops on scaling of meters during drilling of wells (Louks, 1999; Trice, 2005; Medekenova and Jones, 2014). Once a karst drainage system is developed, it has the potential for further enhancement or occlusion from subsequent meteoric dissolution and or deep late burial diagenesis (Trice, 2015).

Cave systems have been discovered that extend from one square kilometer to regions of tens of kilometers long and wide. Most of the cave passages are less than 8 m wide and high (Loucks, 1999).

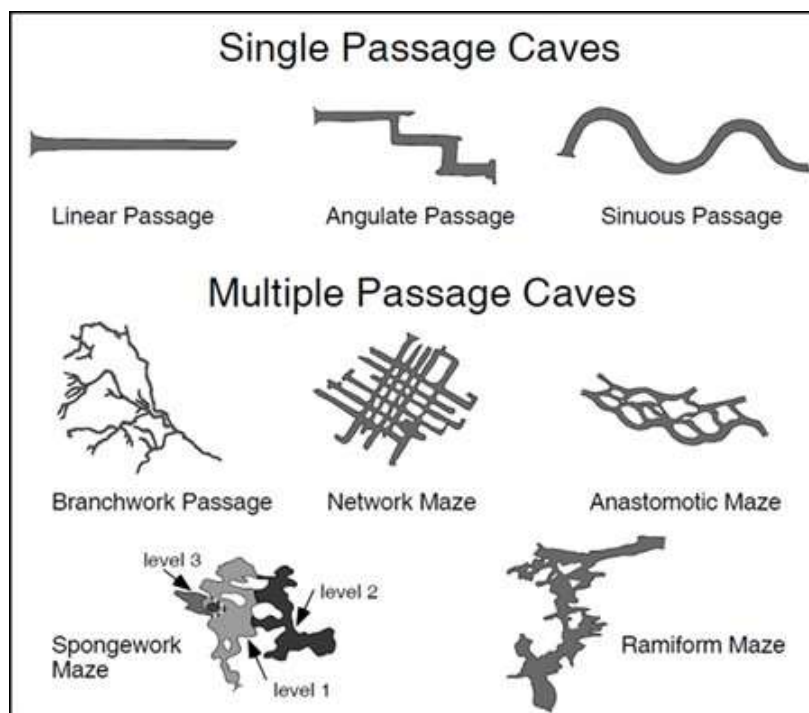


Figure 2.4 Near surface cave geometries of single and multiple passage shown in plan view. From Loucks, 1999

2.4.3 Petrophysical of mega-karst

Large-scale dissolution creates a touching-vug pore system that has little relationship to depositional patterns and cannot be related to interparticle or separate-vug porosity. (Lucia, 2007). Property data collection associated with non-depositional is challenging. Permeability in karsts is highly uncertain and cannot be measured in laboratory. It should be interpreted from well logs or well testing. The fluid flow is concentrated in the touching vug pore system more than in matrix because the pore sizes are typically very large and transmit fluid easily. The flow in touching vugs can be more than 100 times higher than flow in the matrix (Lucia, 2007). Medekenova and Jones (2014) presented a general distribution of porosity and permeability for non-matrix features in carbonates (Figure 2.5), predicting permeability of karst-dominated blocks to be much higher than fracture-dominated blocks.

2.5 Multiscale heterogeneities

The action of depositional, tectonic and diagenetic processes creates heterogeneities in the reservoirs in a wide range of scales that vary from microscopic to the field scale. In general, four levels are determined: pore, lithofacies, geomodel and simulation model (Ringrose and Bentley, 2015). The volume change involved in scale transition is around 18 orders of magnitude when moving from the rock pore to the simulation reservoir model (Curtis, 2015).

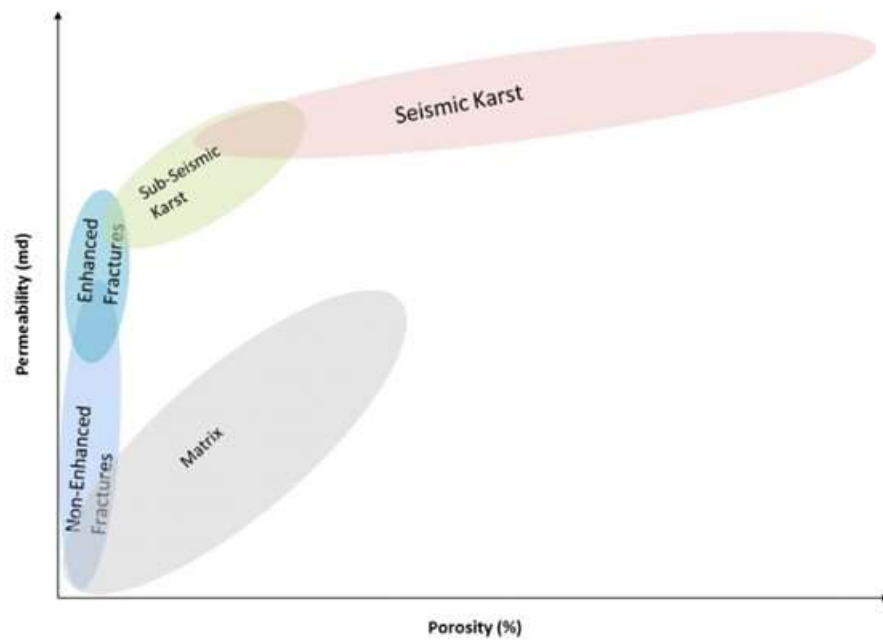


Figure 2.5 Conceptual porosity-permeability relationship for matrix and non-matrix features. From Medekenova and Jones., 2014.

In the multiscale modeling approach, the geological concepts are used to make the transition from smaller scale measurements to large-scale estimates (Ringrose and Bentley, 2015). The main challenge is to incorporate small structures in reservoir models on a larger scale. Due to the hierarchical nature of the geological structures, the upscaling procedure must follow a scale hierarchy (Mikes et al. 2006).

The upscaling process consists in the transfer of property information between grids with different block sizes (Figure 2.6). Upscaling involves a numerical or analytical method for estimating equivalent properties at a larger scale from smaller-scale rock properties (Mikes et al., 2006). Downscaling estimates properties at fine grid from a larger scale property (Ringrose and Bentley, 2015). Upscaling procedures include the application of statistical averages, flow simulation, streamlines, finite differences, boundary condition dependents, among others methods (Mikes et al. 2006; Curtis, 2015).

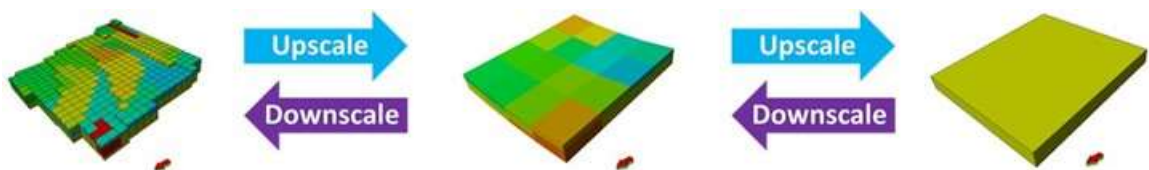


Figure 2.6 Upscaling process.

3 LITERATURE REVIEW

This chapter aims to present practical cases related to the objective of this work.

3.1 Brazilian pre-Salt

The pre-salt in Brazil is a sequence of sedimentary rocks composed mainly of carbonate formed during the separation of American and African continents started about 150 million years ago. These formations are found deep lying under a thick layer of salt that currently reaches 2000 m in thickness, in a distribution about 800 km long and 200 km width in the Brazil offshore, although explorations efforts focus heavily on the Santos, Campos and Espírito Santo basins (Beasley, et al., 2010). Large lakes were formed with a high amount of organic matter deposited. The conditions were favorable for the accumulation of hard parts of different organisms, under different conditions of preservation (Thompson et al., 2015) and for the growth of cyanobacterial colonies (Beasley et al., 2010). As the continents continued to separate, the material accumulated were covered by the oceanic waters. Under arid conditions the water was evaporated and a large deposit of salt was accumulated along the continental margins, covering deposits and forming an effective seal for the hydrocarbons.

The stratigraphic record of interest is represented by two formations: Itapema and Barra Velha. The Itapema formation is composed by intercalations of bioclastic grainstones (commonly referred to as coquinas), wackstones and packstones with mudstone and dark shales. The Barra Velha formation is divided into two sequences that present, in a general way, calcareous microbial stromatolites and laminites in the proximal portions and shale in the distal portions. Grainstones to packstones of stromatolitic and bioclastic fragments are also presented. This stratigraphic section was described for several pre-salt fields (Gaffney et al., 2010). Table 3.1 summarizes the formations and Figure 3.1 shows some examples of the facies present in the Santos basin (Salamoni et al., 2010).

Table 3.1 Briefly description of the interest formations present in the Santos Basin

FORMATION	BRIEF DESCRIPTION
Barra Velha	Microbial stromatolites, laminites and shale
Itapema	Calcareous conglomerates, mudstone and dark shales

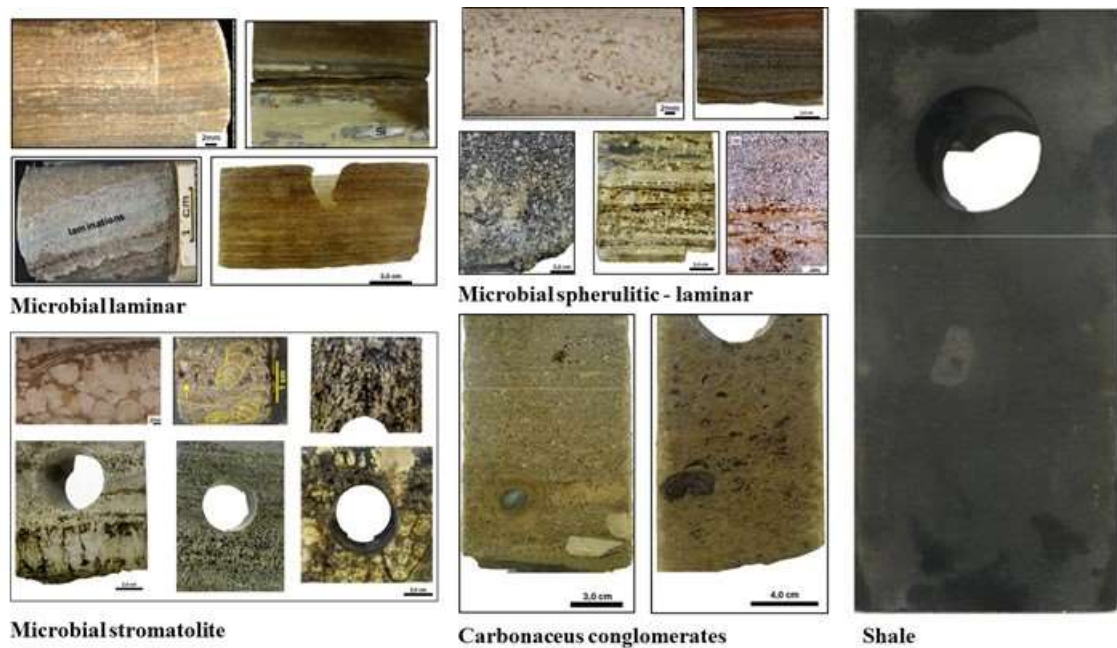


Figure 3.1 Example of facies present in the Santos Basin. (Salamoni, et al., 2010), (Petersohn et al., 2013).

The limits between the formations are given by two surfaces of stratigraphic unconformity. The first one, known as Pre-Alagoas, limits the Itapema of the Barra Velha formations. The second discordance corresponds to a seismic reflector of regional character, known as Intra-Alagoas, which limits the Barra Velha formation in the upper and lower segments (Moreira et al., 2007, Beasley et al., 2010).

The Santos Basin is located in the southeastern part of the Brazilian continental margin, in front of the states of Rio de Janeiro, Sao Paulo, Paraná and Santa Catarina. The basin has an area of approximately 270000 km². According to Moreira et al, (2007) the Basin comprises three super sequences corresponding to the Rift, Post-Rift and Drift phases. The structural framework of the Santos Basin is constituted by normal faults of great extension, parallel to the coastline. The main lineaments for the Basin have an average orientation of 42 ° (Chang et al., 1992). The Libra Discovery in the Santos Basin, is located in water depths of 2000 meters, approximately 200 km South of Rio de Janeiro, located into the east side of the Franco field, an analogous reservoir due to its similarity in depositional environments and proximity (Mann, 2013). In the Libra Discovery, a distinct oil water contact can be observed from the seismic data close to 5720 meters depth (Mann, 2013).

The studies over pre-salt lacustrine carbonate successions are challenging due to their complexities, unusual palaeoenvironmental settings, and the scarcity of publications. These carbonate successions have a great scientific and economic significance as an extensive

hydrocarbon reservoirs, hosting large volumes of oil and gas in the Aptian age (Muniz and Bosence, 2016).

3.2 Karstified carbonate reservoirs

There is a great uncertainty when modeling the distribution of karstic features. For this work, which consists on the elaboration of a synthetic model, it is useful to observe how the use of conceptual and analogous information in outcrops and common geological systems contribute to the generation of reliable geological karstic models.

Biver et al, 2012 present a methodology to model karstic diagenesis using geometrical processes that do not implicate a genetically related approach. In this work can be noted the use of analogous concepts to guide the modeling. The proposed method simulates karstification, using several conceptual models and stages of karst development that can be present in a single reservoir. They defined a karstic region, and randomly selected two blocks of the model and assigned one as a starting point (seed point) and other as an endpoint. Between the two points, a trajectory is randomly generated, with main orientation being a straight line generated by the initial and final point but with some allowed variation. The procedure of modeling karst was developed directly on blocks with the dimension of full field reservoirs. The determination of the permeability for the non-karst elements was derived in an analytical manner using an analogous equation to the Poiseuille law for flow in tubes, considering multiples conduits in a single block. The final model integrated initial matrix depositional facies with modified dissolved and conduits related to non-matrix facies.

Jones, (2015) presents a workflow to represent karst elements using high-resolution geologic models that were populated with distinct geological configurations of sub-seismic karst and matrix. He proposed to use conceptual models, outcrop analogs and cave maps to build the karst element model. They presented a realization in a 500 x 500 x 50 meters model, whit a cell dimension of 5 x 5 x 0.5 meters. The karst feature was populated using two different facies modeling approaches: object-based modeling and multiple point statistics. The matrix petrophysical properties were modeled based on core plug porosity and a specified porosity to permeability transform. The porosity and permeability of the karst features was uncertainty. The workflow he presented was designed to systematically explore the effect of different karst fills on effective properties. He used flow-based averaging methods to calculate the effective reservoir properties at the scale of a full field geologic model block. This works remarks the importance of analogs to bridge data gaps presented by scale heterogeneity.

Mendekenova et al, (2014) present challenges of characterization and modeling associated with fracture and karst. They remark the importance of combining geosciences and reservoir engineering workflows, to create a well characterized and calibrated model. Data integration along with the use of analogs and concepts helped to bridge the data gap. They created a model that integrates matrix and non-matrix elements. The matrix elements are modeled in a standard workflow. They divided the non-matrix porosity into four components based on their scale and potential to enhance flow, including fractures, solution enhanced fractures, karsts, and sub-seismic karst. The karst objects were stochastically populated using object modeling and multipoint statistic. Each non-matrix component was modeled separately, in a dual porosity model, where the shape factor parameter was treated as an uncertainty. They also presented a general distribution of porosity and permeability for non-matrix features in carbonates, where they predicted that permeability of karst is higher than fractures and matrix.

Neillo et al, (2014) proposed a workflow to characterize karst systems integrating information from drilling cores and well logs, including FMI logs, to describe karstic features. After identify the karstic features, they generated the model representing the main karstic events and a background that represented the elements of the matrix and properties that could not be isolated, including fractures. The karstic events represented were two emersions with the development of conduits and karstic networks. The conduits were generated from points of infiltration located in faults and guidelines simulating the action of water dissolving the matrix. Well test and production history allowed the calibration of conductivity and connectivity. The importance of integrating dynamic and static information to correctly describe and represent the behavior of karsts was highlighted, since individually they do not provide complete information to determine the model.

Carneiro et al, (2015) help to conceptualize the role of tectonic patterns in the development of massive dissolution structures. They focused on the effects of fractures in the morphogenesis of epigenetic karst in the Jandaíra formation, of Potiguar Basin, Brazilian northeast. They show that karst structures occur along different structural patterns related to the main trend of fractures. The authors analyzed the role of faults and joints, simplified as lineaments, in the formation of an epigenetic karst, identifying points and types of structural arrangements where the karstic dissolution is concentrated and the karst development occurs (Figure 3.2). Some of this arranges are the interconnection of fractures, center of fractures, termination of fractures, denditric and mixed pattern. They also suggested that these patterns may be involved in the formation of karst in other carbonate systems.

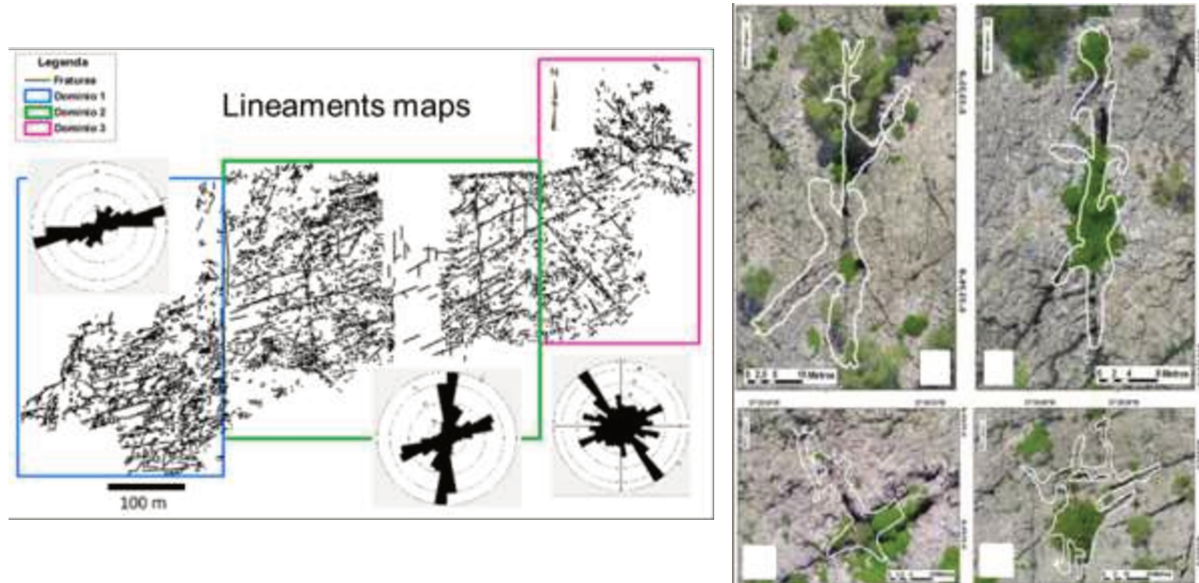


Figure 3.2 Main trend of fractures and their role in development of mega-karst. From Carneiro et al., 2015.

3.3 Hierarchical multiscale approaches

Complex scale-related heterogeneous reservoirs can be modeled based on hierarchical scaling approaches, which present great interest given the success that has been seen when applying them (Curtis, 2015).

Mikes et al. (2006) proposed a method based on the systematic description of facies and beds that served to establish the effect of small-scale parameters on a larger scale. Since geological structures are strictly hierarchical of nature, the upscale should follow this hierarchy, incorporating the impact of different scale structures. They presented a four-step procedure: (1) model construction of flow cells and flow units, (2) parameters assignment, (3) microsimulation for flow simulation on flow cells and, (4) macrosimulation for flow units and reservoir. With this approach, was possible to simplify the reservoir model, such that it becomes manageable for reservoir simulation preserving the effect of small-scale heterogeneities.

Strijker et al., (2012) shows the use of a hierarchical approach and analogous information to define a fractured network in a carbonate region that displays a prominent multiscale system of fractures. He carried out a multiscale approach to quantify the geometry and spatial characteristics of a fractured system in three dimensions, understanding the dependence of the scale in the distribution of fractures.

The fracture networks were classified into a hierarchical fracture model that reflects different fracture systems and stratigraphic control according to the scale, varying in several orders of magnitude, from fault areas of kilometers in length to joints visible to naked eye. This

approach improves the representation of fracture networks in fluid flow simulations of fractured reservoirs.

Gomez et al., (2015) used a multiscale approach to present a methodology to represent fractured carbonate reservoirs in fluid flow simulation. The methodology was focused on integrating geostatistical modeling approaches, upscaling procedures and flow simulation models considering the multiscale complexity of carbonates reservoir. They recognized the need to define a reference solution in a refined grid along the upscaling procedure. That multiscale approach showed to be very useful for representing and simulating fractured reservoirs.

Curtis, 2015, highlighted the multiscale condition when characterizing reservoirs, presenting a hierarchical division of scales that go from the pore scale to the simulation grid, based on the resolution of characterization tools and geological processes. Between those scales, workflows were developed from the wireline log scale to the finer digital rock scale, and from pore scale to core plug, well log and flow simulation grid scale. The workflows seek to show how both static and dynamic petrophysical properties can be transferred from one size to another, integrating data from different sources, into simple workflows in their design to allow their application.

3.4 Benchmark cases

Synthetic models can be used as reference models to *benchmark* proposals, such as the UNISIM-I (Avansi and Schiozer 2015) and UNISIM-II (Correia, et al. 2015). They consist of a (1) simulation model with geological, economic and operational uncertainties and a (2) reference model to be used as a known answer for compare and validate the methodologies. The geologic synthetic model in UNISIM-I represents a siliciclastic reservoir based on structural, facies and petrophysical information from Namorado Field, located in Campos Basin in Brazil. The geological grid cell resolution was defined as 25 x 25 x 1 meter, with 3.408.633 active total blocks (Figure 3.3, left). The simulation model grid resolution was 100 x 100 x 8 meters with 36.739 active blocks.

The UNISIM-II presents a synthetic model that represents Brazilian pre-salt trends. The model consists in a fractured carbonate reservoir with Super-K layers, based on a combination of pre-salt characteristic and Ghawar field information. The geologic model has a grid cell size of 50 x 50 x 1 meters (Figure 3.3, right). The simulation model has a grid cell size of 100 x 100 x 8 meters, with 65000 active blocks.

These *benchmark* cases provide the opportunity to academic institutes and oil companies, to discuss technical decisions to select oil exploitation strategies, using deterministic and probabilistic approaches.

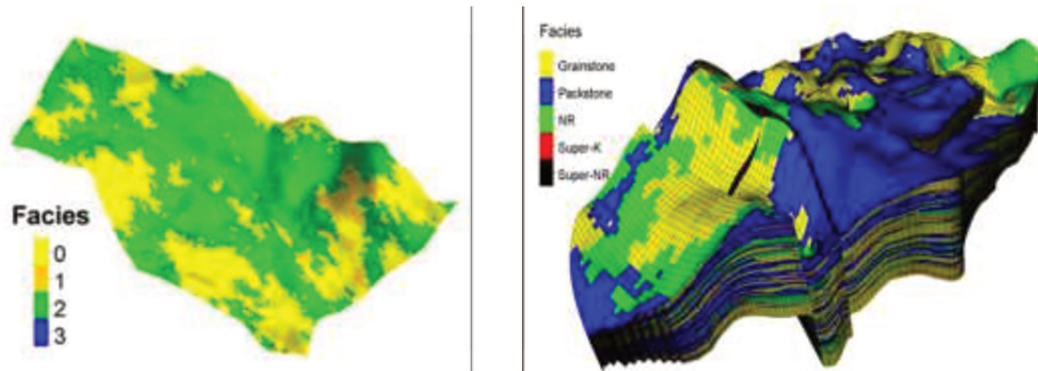


Figure 3.3 UNISIM-I (left) and UNISIM-II (right) geological synthetic models to benchmark proposals.

4 METHODOLOGY

The synthetic full field model Lira-G is generated by combining two models, (1) Lira-M, which represents the primary matrix properties, with (2) Lira-K, which represents the karst properties. They are generated separately at different grid scales and are then combined. Lira-M results of the output stochastic simulation using well log data for the entire field. Lira-K has a finer cell resolution as the karst features are small-scale heterogeneities beyond the Lira-G cell scale. Lira-G uses the same structural grid as Lira-M; therefore, they have the same cell dimensions.

This work follows six main steps that are summarized below and are described in detail in the following sections.

- Development of Lira-M that represents facies and petrophysical distribution, based on the logs from two wells of two Brazilian pre-salt fields. This model has the same dimensions and cell size as the final model Lira-G;
- Development of Lira-K with smaller size cell that represents the karst distribution and petrophysical properties model. Apart from the smaller cell dimension, this model is also smaller than Lira-G as it represents only the regions assumed to karst features development;
- Flow based upscaling of Lira-K and integration with Lira-M to generate the geological model Lira-G;
- Validation of Lira-G for use in numerical flow simulation;
- Upscaling of Lira-G to coarser simulation grid Lira-S;
- Validation of Lira-S for use in numerical flow simulation.

Figure 4.1 shows a general summary of the methodology. The following sections focus on each step in more detail. For generation of the models, the Petrel software from Schlumberger is used. For simulations, Imex from CMG is used.

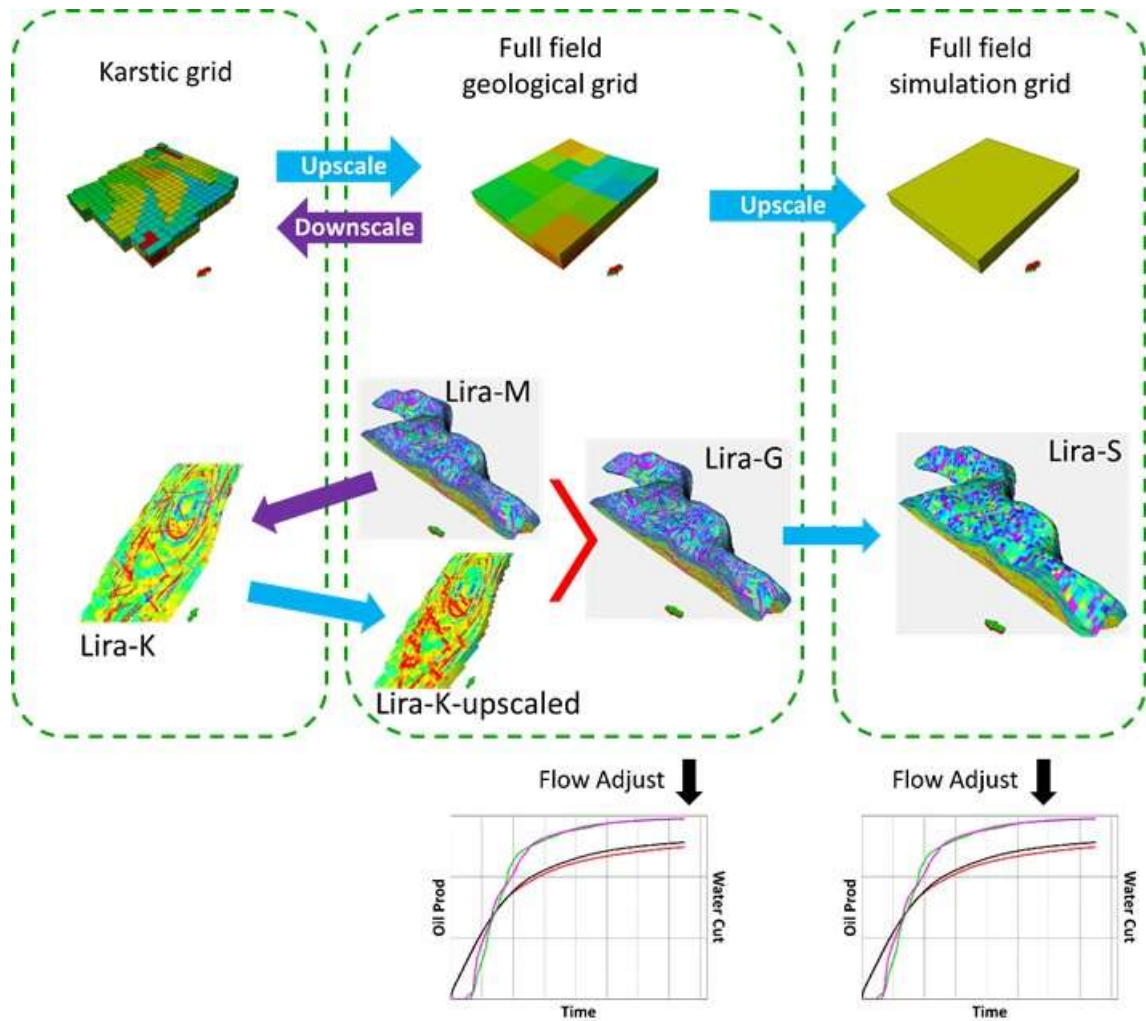


Figure 4.1 Summary of the methodology.

4.1 Lira-M

The LIRA-M model corresponds to the facies and petrophysical model without the influence of karst. It involves three models: (1) structural, (2) facies, and (3) petrophysical. The workflow for the structural model starts with surface generation and modeling, followed by fault modeling, pillar grid, and finally the generation of horizons, zones, and layers (Ringrose and Bentley, 2015).

After the structural model is generated, the technique to populate facies is the truncated Gaussian simulation (TGS), which can be used when there is a natural transition through a sequence of facies in an environment. Typical examples include carbonate environments. The spatial distribution of facies is controlled by the facies transition, the vertical facies proportion in well log and the variogram.

For petrophysical model, the porosity and permeability are populated using Gaussian simulation biasing by the facies previously modeled. The net-to-gross is calculated according

to a specific cut-off in porosity and permeability. The workflow for generation of Lira-M model is shown in Figure 4.2.

4.2 Lira-K

The synthetic model of the karstic system is based on conceptual information. Lira-K involves the three same models as Lira-M (structural, facies and petrophysical). For the structural model the conventional workflow is followed, with horizontal surfaces restricted to a hypothetical zone of karstic development.

The karst elements are generated based on the object modeling process, using the orientation, height, width, and length of the cave passage as conditioning parameters. Once created, the karsts that are connected generate a multiple-passage cave system. These karst systems are grouped to assign properties during the subsequent petrophysical modeling. Before petrophysical modeling, it is necessary to downscale the properties from Lira-M to Lira-K grid. This is an important step for the further upscaling of Lira-K to take into consideration the influence of background and edge cells affected by primary porosity (Lira-M). Therefore, the downscaled properties from Lira-M are used to populate the background in Lira-K and are associated with "non-karst" cells.

Petrophysical distribution in karst is uncertain (Jones, 2015). To populate the karst elements, groups are defined based on ranges of porosity and permeability. The net-to-gross is calculated according to the same cut-off used in the Lira-M. The workflow for generation of Lira-K is shown in Figure 4.3.

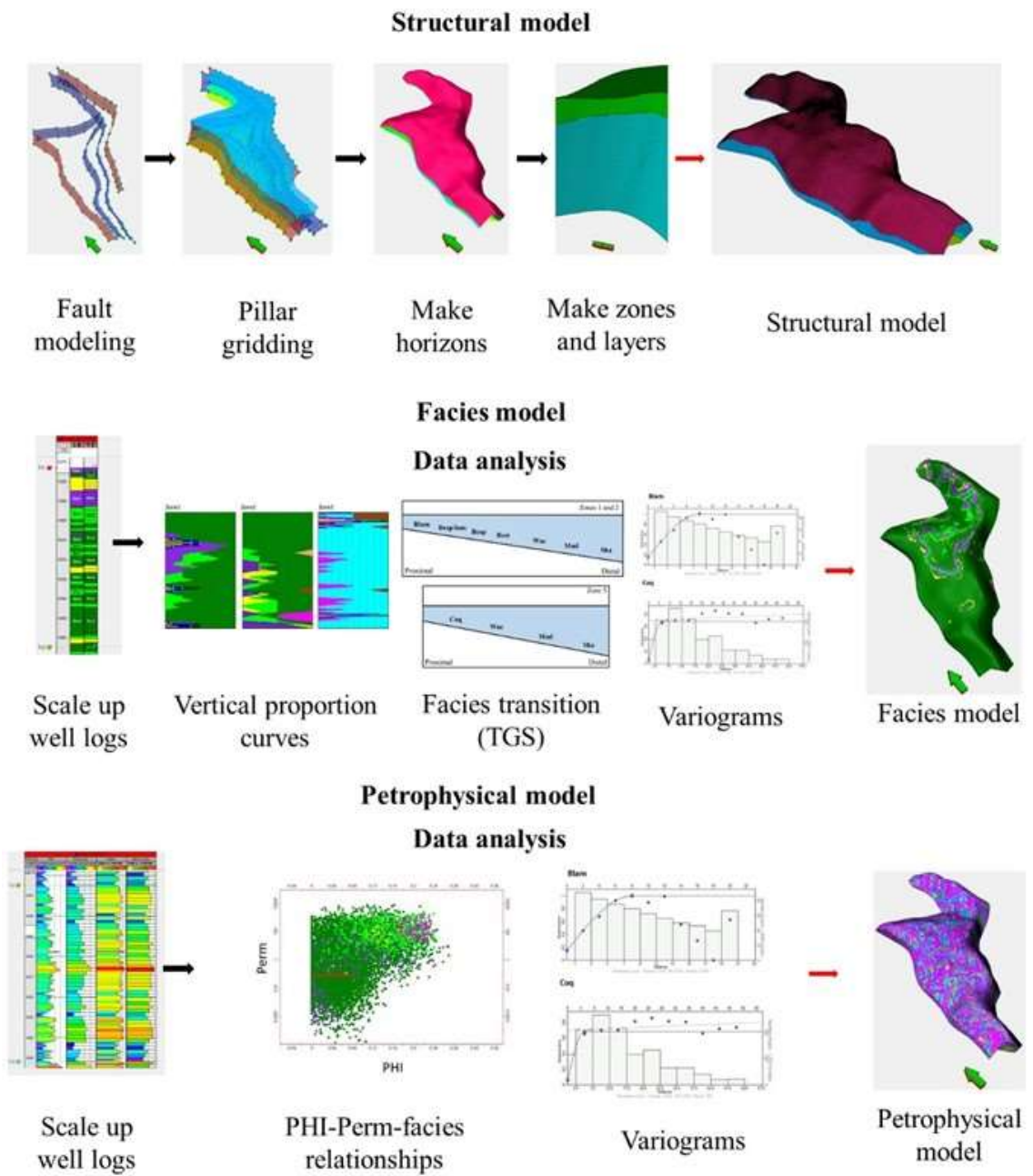


Figure 4.2 Workflow for generating Lira M

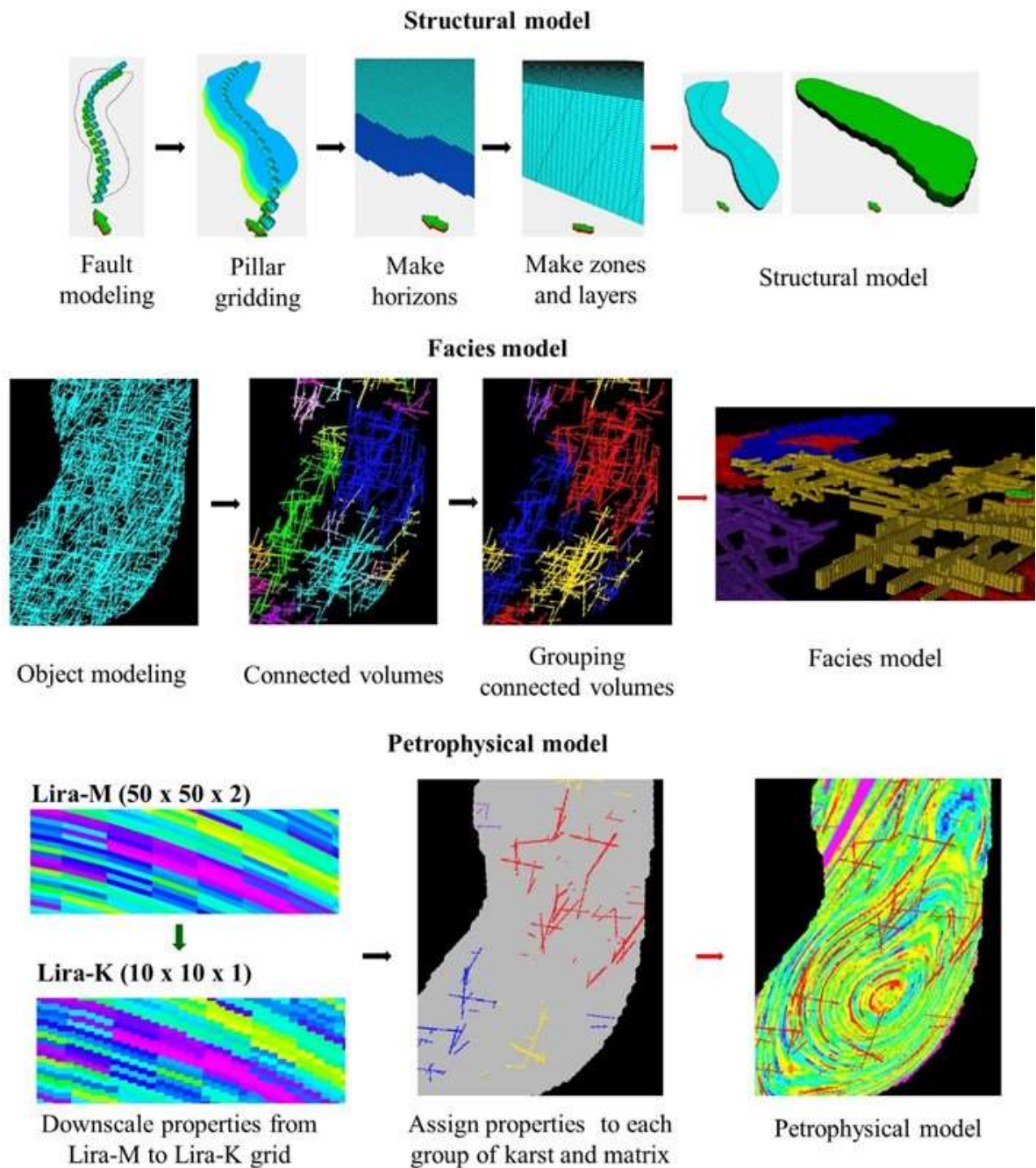


Figure 4.3 Workflow for generating Lira K.

4.2.1 Lira-G

In this stage, Lira-K is upscaled to the Lira-G grid. For this procedure, we use conventionally available methods in modeling software. Then, the upscaled Lira-K and Lira-M are combined. Lira-M has the same scale as Lira-G but does not take into consideration karst features. Therefore, for cells intercepting karst in upscaled Lira-K, the output values from the upscale of Lira-K are considered, and for cells that do not intercept karst, Lira-G has the same petrophysical distribution as Lira-M.

4.2.2 Validation of Lira-G

This step consists of an upscaling matching procedure between Lira-K and Lira-G. It involves the following stages: (1) flow simulation to identify the dynamic behavior in Lira-K and generation of a reference response to compare with Lira G; (2) validation of volumes in Lira-G and Lira-K; (3) validation and flow calibration by comparing the dynamic response of Lira-K with Lira-G and, (4) comparison of water saturation maps between Lira-K and Lira-G. The adjustment of flow is done by the creation of pseudo-curves of relative permeability that represent the combination of the effects of karst and matrix components, applying them in the blocks that represent karst in Lira-G.

4.3 Lira-S

In this stage, Lira-G is upscaled to a coarser grid resolution model, called Lira-S. This step is necessary due to the high number of blocks in Lira-G, which renders them unsuitable for application in numerical flow simulation.

4.3.1 Validation of Lira-S

In this step, the validation procedure for Lira-S is applied in the same way as it was done for Lira-G. The process involves the following steps: (1) validation of volumes in Lira-G and Lira-S, (2) validation and flow calibration comparing the dynamic response of Lira-G and Lira-S and, (3) water saturation maps to compare water advance.

5 APPLICATION

This chapter presents how this work was developed, containing a description of the geological models and their elaboration, including input data and parameters used. Also, how the models are integrated is explained, based on scale transfer between Lira-K and Lira-G grids, and how the adjustment-validation is made for its use in numerical simulation.

Table 5.1 summarizes the generated grids, the block size, and the models to be represented applied in this study.

Table 5.1 Summary of Lira models

Model	Grid [m3]	Description
Lira-M	50 x 50 x 2	Rock matrix with Brazilian pre-salt trends
Lira-K	10 x 10 x 1	Representation of karstic features
Lira-G	50 x 50 x 2	Brazilian pre-salt trends and karstic features (geological field scale)
Lira-S	200 x 200 x 5	Simulation scale model

The geological scenario considered for Lira-G represents a karstic carbonate reservoir, and the model is developed by combining the Lira-M, an outcome of an inter-well geomodeling, with Lira-K, an outcome of karst distribution based on object modeling.

Lira-M is composed of three formations, each of them with a characteristic facies distribution and petrophysical properties, obtained from two well logs. Lira-K corresponds to two small regions of Lira-M and, therefore, the existence of karsts is assigned to two assumed regions.

The details followed to develop Lira-G are presented below. The results obtained are presented discussed in Chapter 6.

5.1 Lira-M

The input data and information used to create the model are the following:

- Map images of the depth of formation surfaces;
- Images of interpreted seismic profiles;
- Facies distribution for two wells;
- Continuous logs of porosity and permeability for two wells.

Part of the information used is supplied by the national oil and gas bio-fuels agency - ANP, and another part is public access. The first well, called Lira-1, is the Libra Wildcat well and is in its real position in relation to the surfaces and the structural model. The second well, called Lira-2 was taken from the Buzios field, Santos basin.

5.1.1 Structural model

Lira-M has the same structure and grid as Lira-G, and they are conditioned by four surfaces and seven faults. The four surfaces are elaborated from the depth maps of the three formations (Petersohn et al., 2013) (Figure 5.1). They are called, from top to bottom, Tz1, Tz2, Tz3 and Bres, and the zones they limit are called Zone 1 (Z1), Zone 2 (Z2) and Zone 3 (Z3).

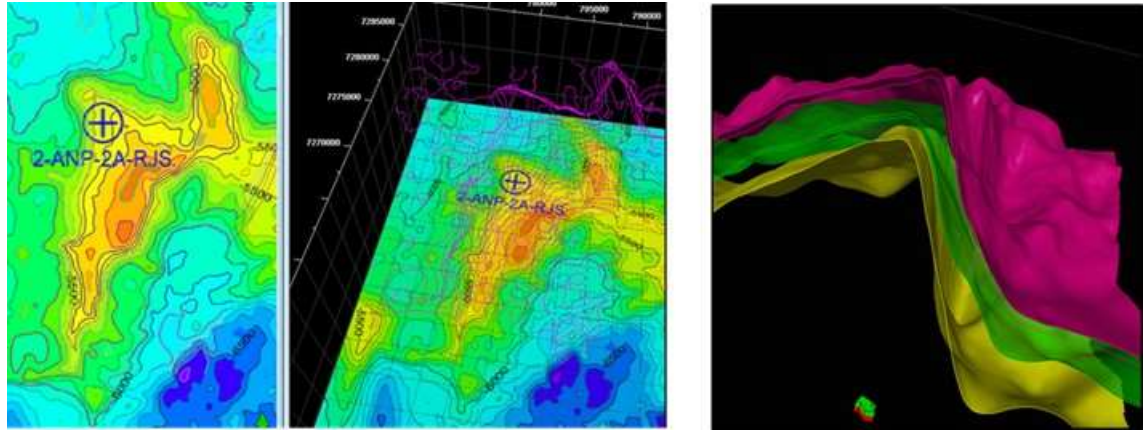


Figure 5.1 Creation of surfaces based on maps of boundary of formations

Seven faults are constructed using images of interpreted seismic profiles (Petersohn et al., 2013) (Figure 5.2), three of them are boundaries of the field, and four faults are internal. The surfaces generated helped to define the faults in the intermediate zones between the seismic profiles. From the images, we cannot determine an exact value for the throw. When creating the horizons, in the areas close to the faults, the surfaces are extrapolated at a distance from the fault plane, defined in this case as 100 meters (2 blocks of the model grid) creating an apparent and variable throw that follows the trend of the surfaces.

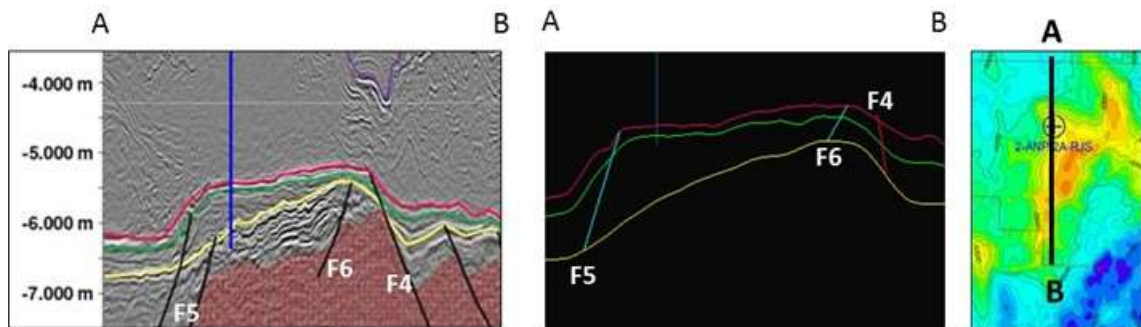


Figure 5.2 Creation of fault model based on images of interpreted seismic profiles

The faults are defined as zig-zag fault type and affect all three formations (Figure 5.3). The transmissibility attributed to the faults can be calculated using different methods, as based on displacement, shale gouge ratio, rock type, etc. (Schlumberger, 2015). As a result, the

internal faults are partially open, with values of transmissibility multipliers presented in Table 5.2.

Table 5.2. Fault transmissibility multipliers.

Fault	Trans Mult
3	0.64
4	0.76
5	0.98
6	0.91

In the three zones, the layers are distributed following the base surface of the formation, from bottom to top (Figure 5.3).

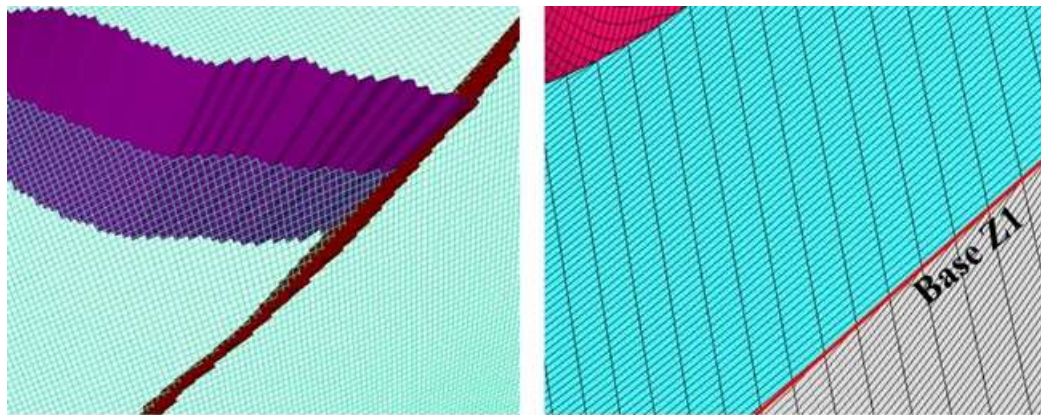


Figure 5.3 Zig-zag faults (left) and layers following the base (right) in the structural model of Lira-M.

The grid resolution is 50 x 50 x 2 meters, which results in 10.339.395 active cells. with a bulk volume of roughly 50 billion m³ (Figure 5.4). The same grid is applied for Lira-G.

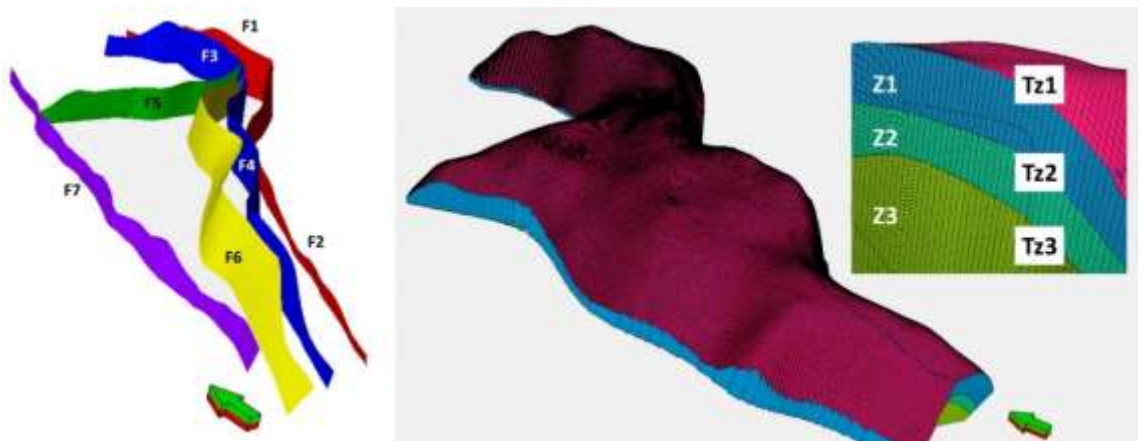


Figure 5.4 Lira-M structural model.

5.1.2 Facies model

The facies information in the composite log is used for modeling based on truncated Gaussian simulation (TGS), as the facility to consider the depositional transition through a sequence of facies. First, the facies are taken from the logs and positioned on the grid using

upscaled methods for discrete properties. Figure 5.5 shows the facies in the composite log in track 1 and upscaled to grid in track 2.

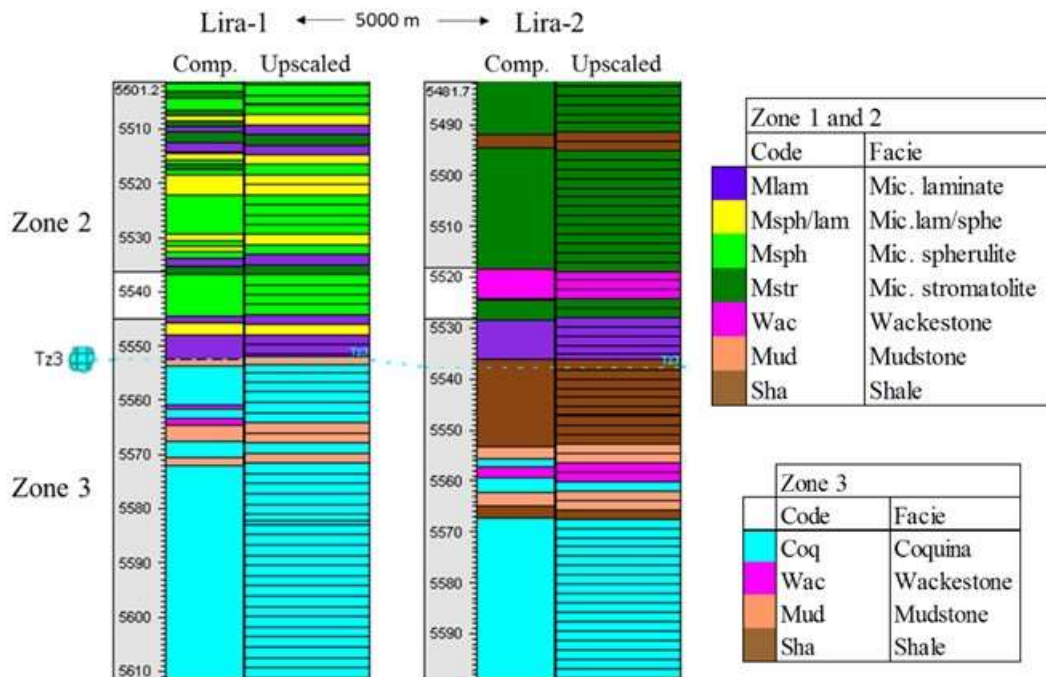


Figure 5.5 Facies from composite log and upscaled in a segment of Lira-1 and Lira-2 wells

To populate the grid with the facies based on TGS, it is necessary to assign the order of facies transition. For Lira-M, we assume a general simple transition from proximal to distal. In zones 1 and 2, the facies vary from microbial laminar and stromatolitic carbonates to wackestone, mudstone, and shale. For Zone 3, the transition varies from grainstone (coquinas) to wackestone, mudstone, and shale. Figure 5.6 shows the arrangement considered. This was raised based on descriptions on equivalent lacustrine sedimentary environments. (Muniz and Bosence, 2015; Suosaari et al, 2016; Jahnert and Collins, 2011; Jahnert and Collins, 2012; Thompson, Stilwell, and Hall, 2015).

The variogram is modeled according to the azimuth of principal lineaments reported as 42° (Chang et al, 1992). Once the data analysis is performed, the stochastic simulation is run. Since is a stochastic model, if the seed number changes, the resulting model is different, but honoring the parameters previously assigned.

After upscaling well logs, porosity and permeability are associated with the facies for each formation. Porosity and permeability are populated using Gaussian simulation biasing by facies. Table 5.3 and 5.4 show the parameters used to generate the porosity and permeability model.

For vertical permeability is applied an average multiplier for each zone. The multipliers are calculated as the relationship between the harmonic average (vertical permeability) and the arithmetic average (horizontal permeability) in the wells. Table 5.5 shows the vertical permeability multiplier calculated for each formation based on the two wells.

The net to gross (NTG) is calculated based on a cut-off approaching: if porosity is zero, or if permeability is less than 0.1 millidarcy the block is considered non-reservoir and the NTG is 0. For permeable facies, NTG is 1

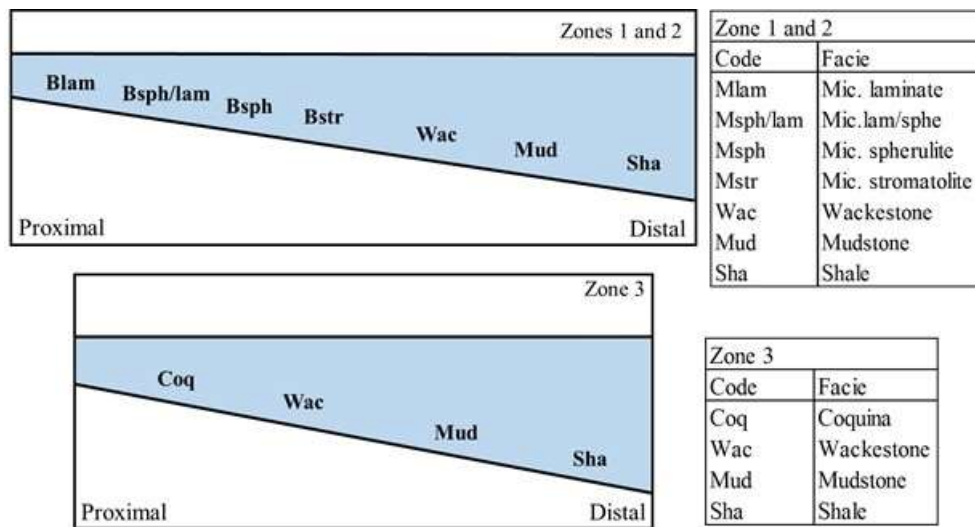


Figure 5.6 Distribution of facies used as input for Truncated Gaussian simulation.

5.1.3 Petrophysical model

For petrophysical modeling, we use the continuous density-porosity (DPHI) and nuclear resonance magnetic permeability from well logs. The well logs are upscaled to grid resolution, by computing the effective property at each block intercepted by the well (Figure 5.7). For porosity, it is used the arithmetic average method. For permeability, two average methods are applied: for flow along continuous parallel layers, the arithmetic average gives the effective permeability, while for flow perpendicular to continuous parallel layers the harmonic average is the applied method (Ringrose and Bentley, 2015). Thereby, the arithmetic average defines the horizontal permeability and harmonic average indicates the vertical permeability for each of the blocks intercepted by the wells.

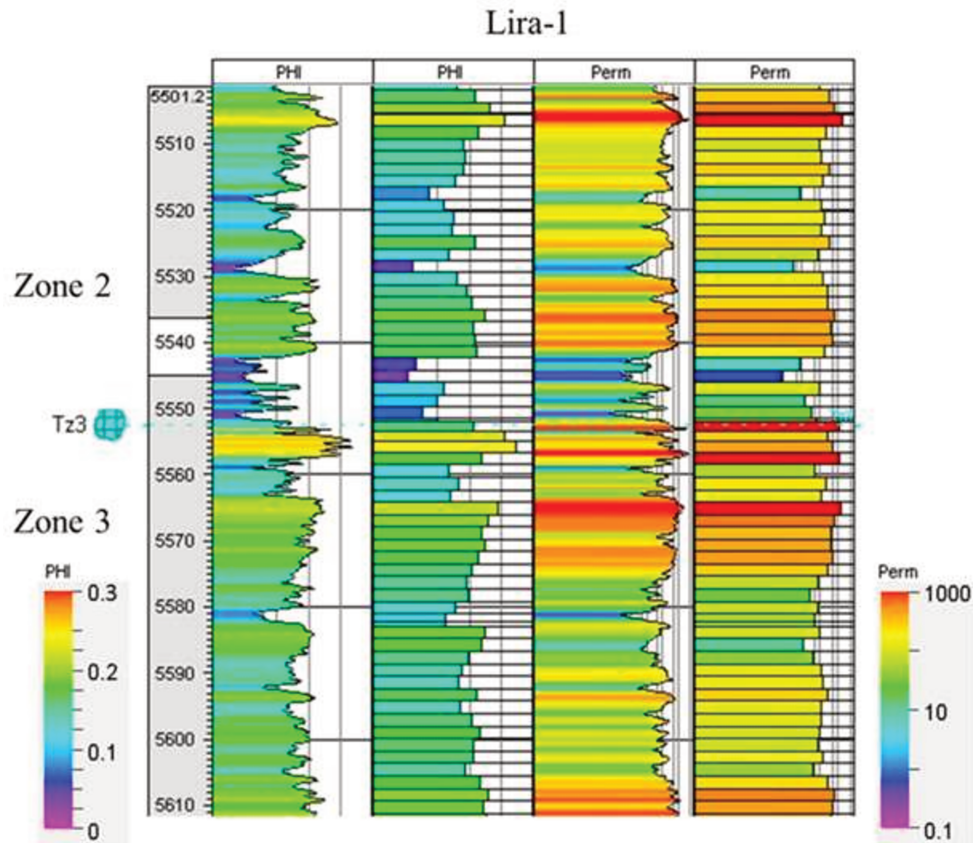


Figure 5.7 Upscale of porosity and permeability from well log to grid, in a segment of Lira-1.

Table 5.3 Parameters used in generation of porosity model in Lira-M

Porosity - Zone 1					
Facies	Major dir [m]	Minor dir [m]	Vertical [m]	Azimuth [°]	Distribution
Blam	1500	500	2	42	Normal from Perm well log
Besf/lam	1500	500	2	42	Normal from Perm well log
Besf	1500	500	2	42	Normal from Perm well log
Best	1500	500	4	42	Normal from Perm well log
Sha	1500	1000	2	42	Normal - mean= 0.04; sd=0.02
Porosity - Zone 2					
Facies	Major dir [m]	Minor dir [m]	Vertical [m]	Azimuth [°]	Distribution
Blam	1500	500	2	42	Normal from Perm well log
Besf/lam	1500	500	4	42	Normal from Perm well log
Besf	1500	500	2	42	Normal from Perm well log
Best	1500	500	4	42	Normal from Perm well log
Wac	1500	500	2	42	Normal from Perm well log
Sha	1500	1000	2	42	Normal - mean= 0.04; sd=0.02
Porosity - Zone 3					
Facies	Major dir [m]	Minor dir [m]	Vertical [m]	Azimuth [°]	Distribution
Blam	1500	500	2	42	Normal - mean= 0.08; sd=0.02
Wac	1500	500	2	42	Normal from Perm well log
Mud	1500	100	2	42	Normal from Perm well log
Coq	1500	500	4	42	Normal from Perm well log
Sha	1500	1000	2	42	Normal - mean= 0.04; sd=0.02

Table 5.4 Parameters used in generation of permeability model in Lira-M

Permeability - Zone 1					
Facies	Major dir [m]	Minor dir [m]	Vertical [m]	Azimuth [°]	Distribution
Blam	1500	500	2	42	Log normal from Perm well log
Besf/lam	1500	500	2	42	Log normal from Perm well log
Besf	1500	500	2	42	Log normal from Perm well log
Best	1500	500	4	42	Log normal from Perm well log
Sha	1500	1000	2	42	Log normal - mean= 0.08; sd=0.01
Permeability - Zone 2					
Facies	Major dir [m]	Minor dir [m]	Vertical [m]	Azimuth [°]	Distribution
Blam	1500	500	2	42	Log normal from Perm well log
Besf/lam	1500	500	4	42	Log normal from Perm well log
Besf	1500	500	2	42	Log normal from Perm well log
Best	1500	500	4	42	Log normal from Perm well log
Wac	1500	500	2	42	Log normal from Perm well log
Sha	1500	1000	2	42	Log normal - mean= 0.08; sd=0.01
Permeability - Zone 3					
Facies	Major dir [m]	Minor dir [m]	Vertical [m]	Azimuth [°]	Distribution
Blam	1500	500	2	42	Log normal - mean= 0.9; sd=0.1
Wac	1500	500	2	42	Log normal from Perm well log
Mud	1500	100	2	42	Log normal from Perm well log
Coq	1500	500	4	42	Log normal from Perm well log
Sha	1500	1000	2	42	Log normal - mean= 0.08; sd=0.01

Table 5.5 Vertical permeability multiplier calculated by zone

	Lira 1	Lira 2	Lira Field
Zone 1	0.34	0.44	0.39
Zone 2	0.48	0.37	0.43
Zone 3	0.6	0.47	0.54

5.2 Lira-K

The Lira-K is based on conceptual information. The location of karstic development zones was selected considering the regional structural framework such as the distance to the major faults, along with formation tops. The grid of this model has a finer cell resolution, as the karst features are small scale heterogeneities beyond the Lira-G cell scale. The block size defined is 10 x 10 x 1 meters.

Two zones of karsts development, one in the formation 2 (Lira-K zone 2) and other in the formation 3 (Lira-K zone 3) are created. In zone 2, the grid is defined by two horizontal surfaces that represent the paleo-underground water system, with depths of 5250 and 5285 meters and the cut with Zone 2 boundaries (Tz2 and Tz3), as shown in Figure 5.8. The region created is 35 meters thick and is composed of 1.153.237 cells. For Zone 3, the grid is defined by the horizontal surfaces at depths of 5340 and 5380 meters and the cut with the Zone 3 top

(Tz3). This is 40 meters thick and is composed of 5.541.560 cells. Figure 5.8 shows the structural sections of Lira-K.

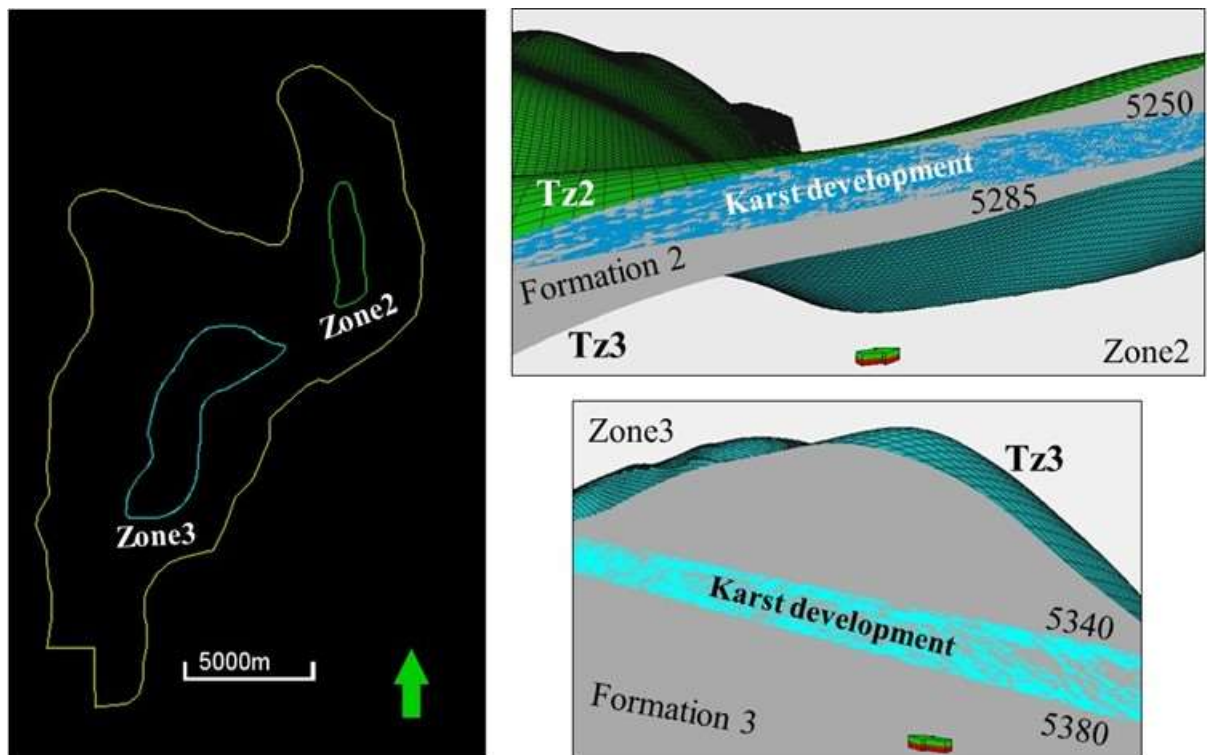


Figure 5.8 Definition of the Lira-K grid in relation to Lira-M

5.2.1 Facies Model

The distribution of karst features is generated using objects modeling technique. The element to model is the cave passage. In this study we assumed a cave passage to be a dissolution enhanced width fracture (Medekenova et al., 2014). We also assume that karst occurs in tectonic structures where a concentration of faults, fractures or joints exists and that these structures can be simplified as lineaments (Carneiro et al., 2015). Therefore, it can be modeled as a box-shaped object with variable height, width, length, and main orientation. For main lineaments three main orientations are selected from the structural model, with azimuth close to 10, 50 and 110 (Figure 5.9).

To generate the individual elements the parameters shown in Table 5.6 are applied, based on Loucks, (1999); Carneiro et al, (2015); Klimchouk et al, (2016); Jones, (2015).

Once the elements are created they are assigned to a new facies called Karst (Figure 5.10 - left). The next step is to group these elements which are connected to create continuous multiple passage caves systems. This is accomplished by using the geometrical modeling process, selecting the connected volume option for the facies karst created (Figure 5.10 - center).

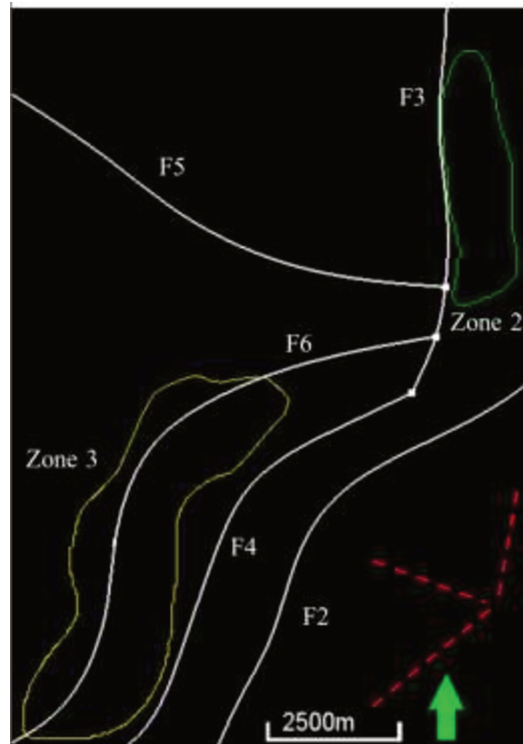


Figure 5.9 Definition of main lineaments for Lira-K, in red dotted lines.

Table 5.6 Summary of parameters for karst object modeling

Zone	Body Shape	Main Orientation [normal]		Karst Width [m] (normal)		Karst length/ Karst Width		Karst height [m] (truncated normal)		
		Mean	Std	Mean	Std	Mean	Std	Min	Mean	Std
3	Box	10 - 40 - 100	5	10	5	30 - 20 - 15 - 10	10	2	4 - 3	2
2	Box	10 - 40 - 115	5	10	5	20 - 10	10	2	4 - 3	2

After the volumes are connected, we select the number that covered the percentage of karst to be represented, 4%, in this case (Trice, 2015). By knowing the total number of cells in the Lira-K in zones 2 and 3, we can determine the number of cells that would reorder close to 4% of the total grid. Then, we can determine the number of connected volumes of that percentage. For zone 2, 14 connected volumes have 46.302 cells, representing the 4%; for zone 3, 23 connected volumes with 216.433 cells represent 4%. Then, the selected volumes are distributed in four groups to subsequent petrophysical modeling (Figure 5.10 - right).

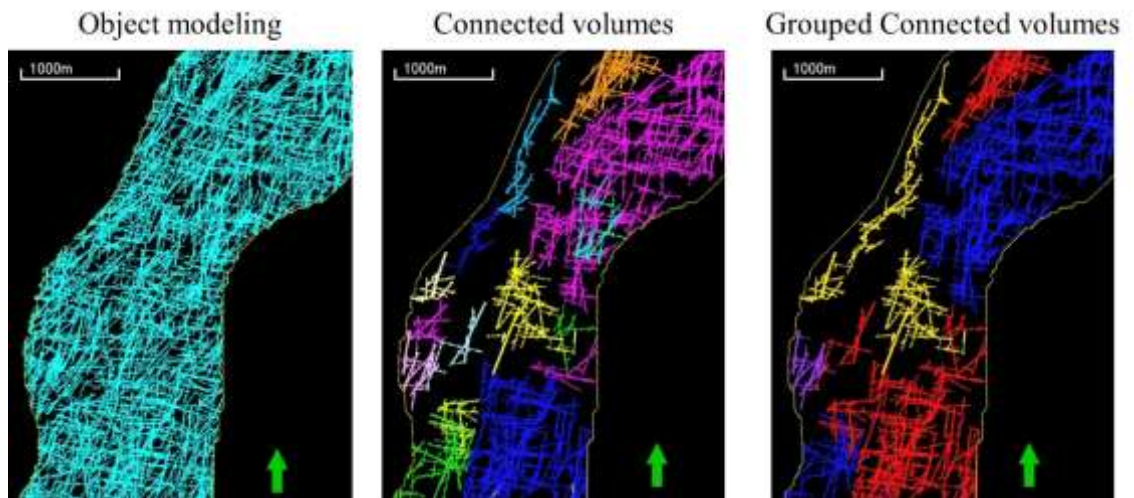


Figure 5.10 Workflow for karst distribution modeling.

The discrete property Rock Type (RT) which indicates if a cell represents matrix (RT=1) or karst (RT=2) is created to be used during the petrophysical modeling, upscale process, and flow simulation.

5.2.2 Petrophysical model

Before petrophysical modeling of karst features, it is necessary to downscale the properties from Lira-M to Lira-K grid, in order to consider the influence of background and edge cells affected by primary porosity (Lira-M), when modeling properties of karst. The downscale process finds the source property values at the center of the target cell (Schlumberger, 2015) and is applied to porosity and permeability from Lira-M to Lira-K grid (Figure 5.11).

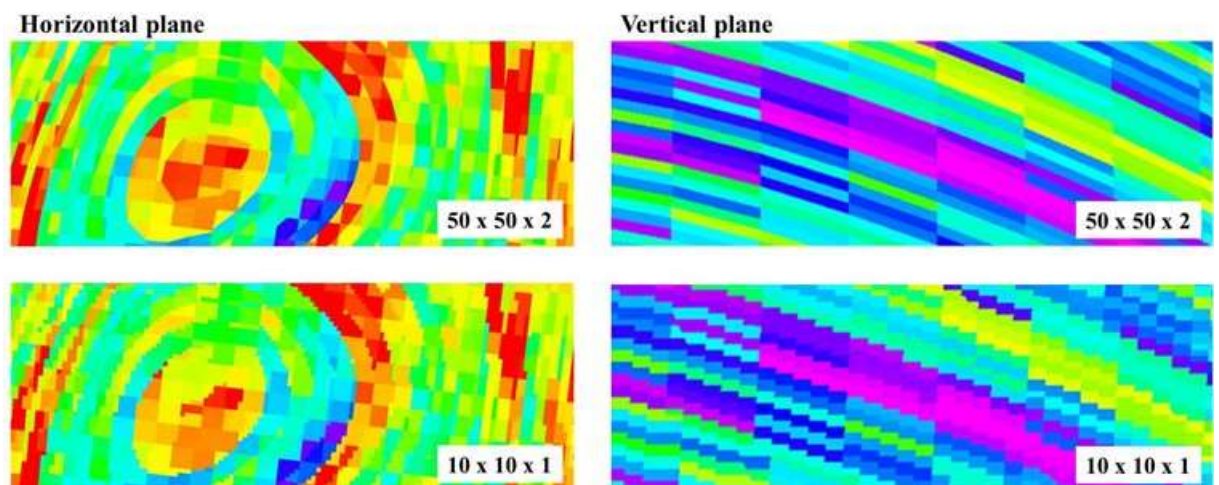


Figure 5.11 Downscaled of permeability from Lira-M to Lira-K, in a horizontal (left) and vertical (right) view.

The classes of karst properties are based on porosity and permeability. The selected range values seek to simulate the effect of different karstic fillings (almost open to collapsed) as presented in Jones, 2015, and Medekenova and Jones, 2014. Table 5.7 summarizes the range of porosity and permeability values assigned for the classes of karst.

Table 5.7 Petrophysical properties assigned for karst modeling

Porosity				
Karst class	min	max	Mean	dev
1	0.56	0.80	0.68	0.07
2	0.63	0.78	0.70	0.05
3	0.83	0.87	0.84	0.02
4			0.05	0.03
Permeability				
Karst class	min	max	Mean	dev
1	2000	11000	9000	2500
2	1000	2500	2000	600
3	1000	11000	8000	3000
4			0.1	0.1

The petrophysical model is generated using Gaussian simulation. Porosity and permeability are simulated for each class of karst. For background facies (without karst influence), porosity and permeability are set from the downscaled Lira-M (Figure 5.12). In karsts is assumed that the ratio of vertical permeability and horizontal permeability is 1, and for variograms, we assumed horizontal isotropy. The net to gross is calculated according to the same cut-off used in Lira-M.

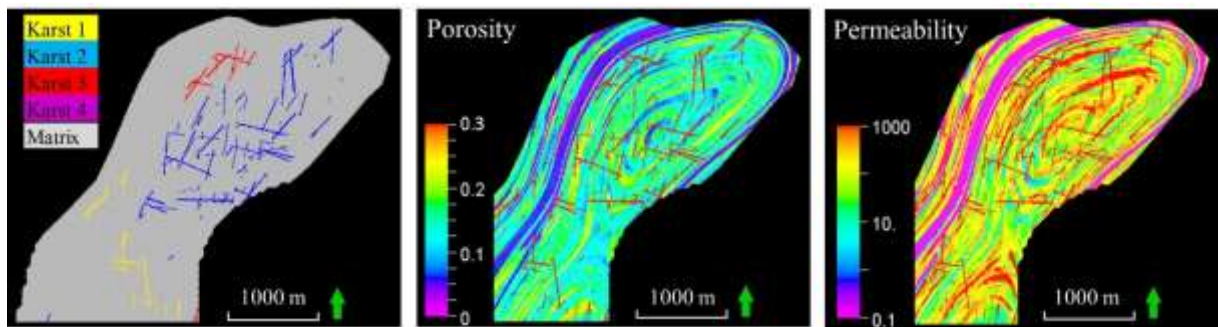


Figure 5.12 Porosity and permeability models in Lira-K.

5.3 Generation of LIRA-G

The generation of Lira-G follows two main stages: transfer of scale from Lira-K to the Lira-G grid, and integration of models in the Lira-G grid.

Once the Lira-K is generated, it must be transferred to Lira-G grid. For this procedure, we use the available methods in commercial software. RT property is upscaled as a discrete property weighting by porosity and permeability. The average method known as mode, which gives the most common value of those presents in the average is used. When the weighted method is applied it maintains the tendency of the karstic system better represented after upscaled. In Chapter 6 a more detailed description are presented. Porosity is upscaled using the arithmetic mean weighted with the NTG. The permeability is upscaled with the flow-based upscaling method, using close flow between layers as boundary condition.

The integration of Lira-M and Lira-K in Lira-G is done based on a logical operation that relates the formation (Zone 1, 2 or 3), the Lira-M and the upscaled Lira-K properties, taking into account that Zone 1 has no karstic development, while Zones 2 and 3 present karstic development in the delimited areas. The integration rules are defined as follows: for Zone 1 there is no karst development, therefore we assign the same value of the properties determined in Lira-M. For Zone 2, if $RT=2$ in the upscaled Lira-K block, assign the upscaled property, if not, assign the property from Lira-M. In the same way for Zone 3, if $RT=2$ in cells of upscaled Lira-K, assign the upscaled property, if not, assign the property from Lira-M. Figure 5.13 shows the integration process.

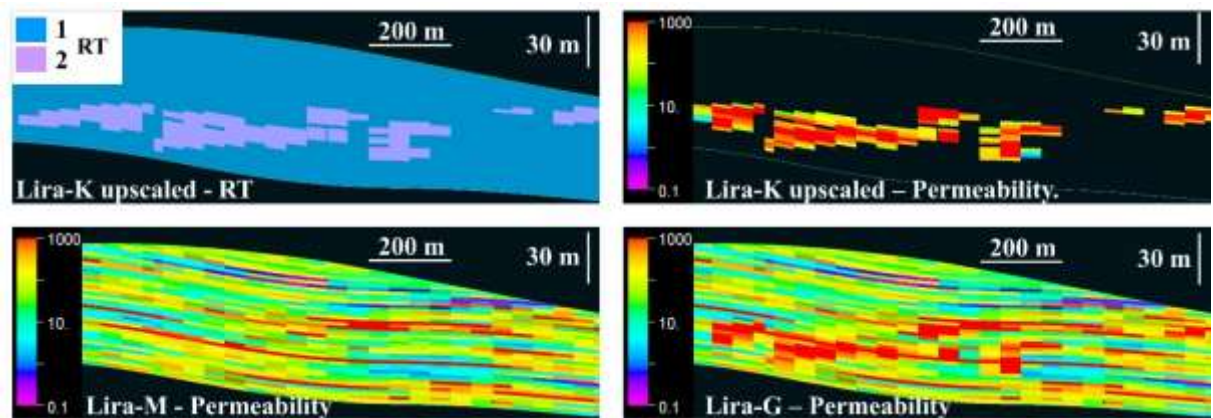


Figure 5.13 Integration of upscaled Lira-K and Lira-M into Lira-G.

5.4 Validation of Lira-G

For this procedure is selected a region from Lira-K and Lira-G in zones 2 and 3. (Figure 5.14). The main steps of the validation process are the flow simulation in Lira-K, to be used as a reference response, and the flow adjustment in Lira-G.

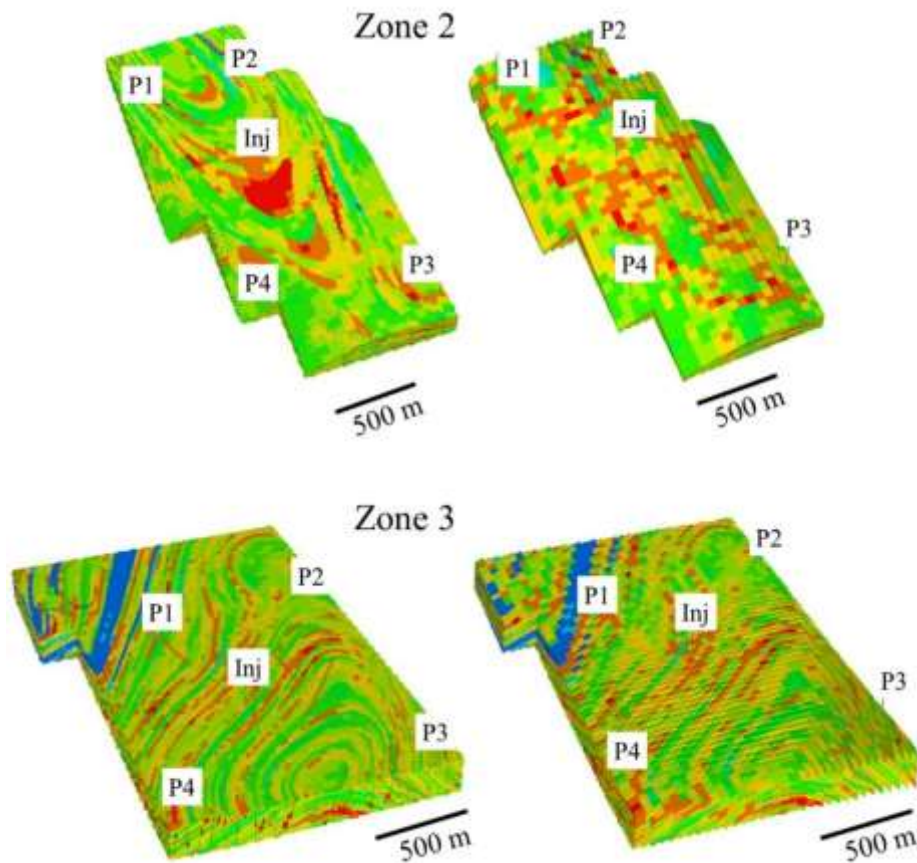


Figure 5.14 Selected zones for validate Lira-G. Top: Zone 2; bottom: Zone 3. Example for Permeability.

5.4.1 Simulation in Lira-K

This study assumed a cave passage to be a dissolution enhanced fracture (Medekenova et al., 2014). The concept of an equivalent porous media is important when modeling fractured reservoirs which can be treated by various levels of complexity. The simplest approach treats the reservoir as a single porosity system. For more complex scenarios it should be treated as a dual porosity system. The continuity of the fractured system is essential. When a fracture system is continuous and interconnected at a given scale, it can be treated as an equivalent porous medium using either a single or dual porosity model (Nelson., 2001; Gale., 1982). This is the case presented in Lira-K, where the enhanced fractured system is continuous at the 10 x 10 x 1 m block size. (Figure 5.15). For this study, we modeled Lira-K as an equivalent single porous medium as we assume the scale of karstic features at the same level of block size.

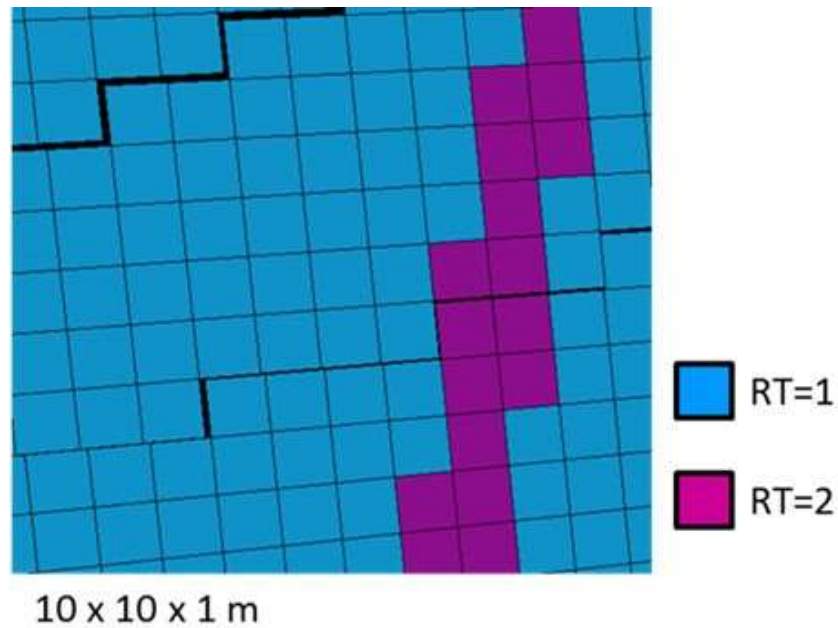


Figure 5.15 Karts system continuous in a whole block at Lira-K scale.

We apply an inverted five spot strategy to determinate the behavior in Lira-K. The vertical production wells are located at a distance close to 1 km between each other (Figure 5.14). Table 5.8 shows the rock-fluid properties and reservoir parameters for initialization of simulation.

The model has two rock types, representing matrix and karst. Figure 5.16 presents the curves of relative permeability applied in Lira-K. The curve for RT=1 is from a real carbonate reservoir of the Brazilian pre-salt in the Santos basin. We assume the same relative permeability of fracture systems to karstic facies (RT = 2), although other relative permeability curves can be applied (Pauget et al., 2014).

Table 5.8 Rock-fluid properties and parameters of validation model

Property	Value
Gas Density	1.35673
Oil Density	926.01
Water density	1
Reservoir temperature	90 [°C]
Reference pressure	630 [kgf/cm ²]
Reference pressure depth	5300 [m]
Rock compressibility	4.27E-05 [1/(kg/cm ²)]
Constant bubble point pressure	500 [kgf/cm ²]
Water-oil contact	5720 [m]
Oil viscosity	0.35 [cp]

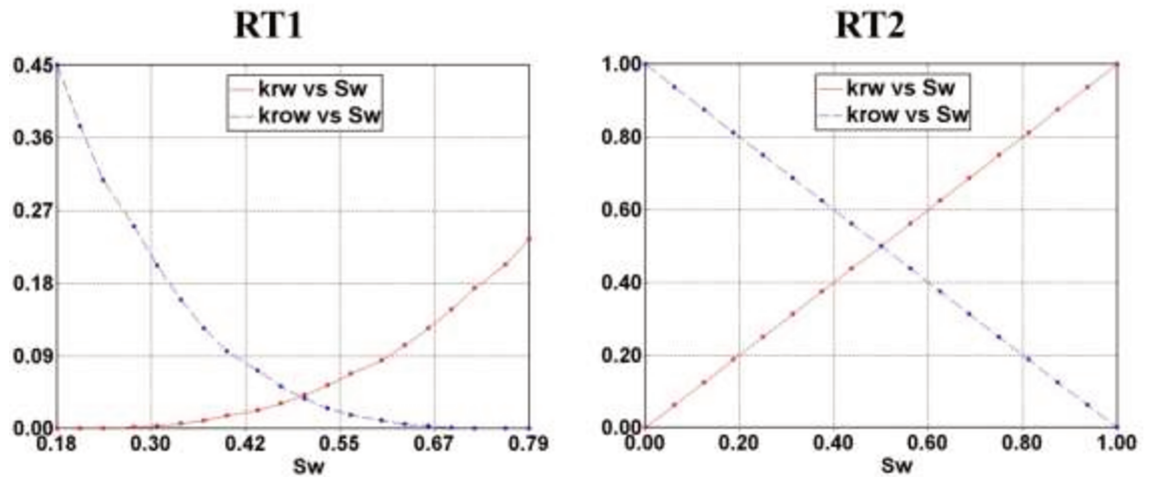


Figure 5.16 Relative permeability curves for RT=1 and RT=2 in Lira-K

The operational parameters of the injection well were established with a maximum injection rate of 3000 m³ / day and a maximum pressure of 660 kgf/cm²; for production wells, we established a minimum pressure of 520 kgf/cm², being above the bubble point pressure to obtain only oil production.

5.4.2 Flow adjustment

In this stage, we apply in Lira-G the same initialization parameters as Lira-K and then compare the response of the two models. A poor match is observed between Lira-G and Lira-K (Figure 5.17).

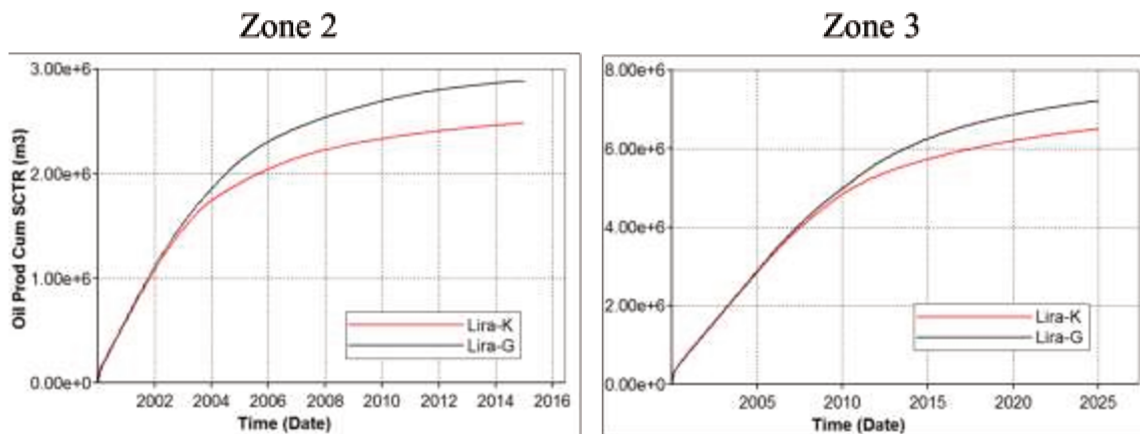


Figure 5.17 Comparison of cumulative oil production in Lira-K and Lira-G using the same relative permeability curve for RT=2

Thus, the use of pseudo-curves of relative permeability is applied, in order to get a good match with the reference solution because of dynamic phenomena that cannot be upscale by the common averages used for static properties (Correia, 2014). The pseudo-curve represents the

combined dynamic effect of karst and matrix features from the reference solution into a coarser grid. The detailed analysis of a methodology to obtain a pseudo-curve of relative permeability is out of the scope of this work. We use a practical approach to modify the relative permeability curve for $RT=2$ in Lira-G: first by modifying the points of S_{wi} and S_{or} , and then adjusting the shape of the relative permeability curve varying the Corey exponents.

The new points of S_{wi} and S_{or} are determined using the value of S_{wi} and S_{or} in the curves of Lira-K and the average percentage of blocks of Lira-K with $RT = 1$ and $RT = 2$ included in the blocks of $RT = 2$ in Lira-G. To determine the average percentage, a downscale of RT is applied from Lira-G to Lira-K (Figure 5 18 A and B). Then the average percentage of blocks in Lira-K with $RT = 1$ and $RT = 2$ included in blocks with $RT = 2$ of Lira-G is calculated (Figure 5 18 C and D).

Thus, in zones 2 and 3 the average percentage of matrix blocks calculated is 84% and of karst blocks is 16%. The new S_{wi} and S_{or} points are calculated as the RT weighted average between the end points of the relative permeability curves in the reference model. In this way, the points determined for $RT = 2$ for Lira-G in zones 2 and 3 are $S_{wc} = 0.02$ and $S_{or} = 0.82$.

The second step for the upscaling-matching procedure is the modification of Corey Coefficients. An increase in coefficient in any of the phases generates a decrease in relative permeability with respect to the other phase present in the system. Figure 5.19 shows the pseudo-curves applied for $RT = 2$ in Lira-G in zones 2 and 3 to obtain a good match with Lira-K.

Figure 5.20 shows the match obtained after modifying the relative permeability curve in the cumulative oil production. The graphs of other parameters of the field are presented in the Chapter 6.

Finally, water saturations maps at different times of simulation are observed and compared between the models. For Zone 2, the horizontal plane is taken at 5260 meters deep and for Zone 3 at 5350 meters. The graphs of other parameters of the field and the resulting maps are presented in the Chapter 6.

5.5 Upscale to Simulation grid Lira-S

The simulation grid is generated using the same input parameters applied in the structural model of Lira-G. The block size is 200 x 200 x 5 meter, with 296.000 active blocks. RT property is upscaled as a discrete property weighting by porosity and permeability. Porosity is upscaled using the arithmetic mean weighted with the NTG. Permeability is upscaled with the flow-based upscaling method, using close to flow between layers as the boundary condition.

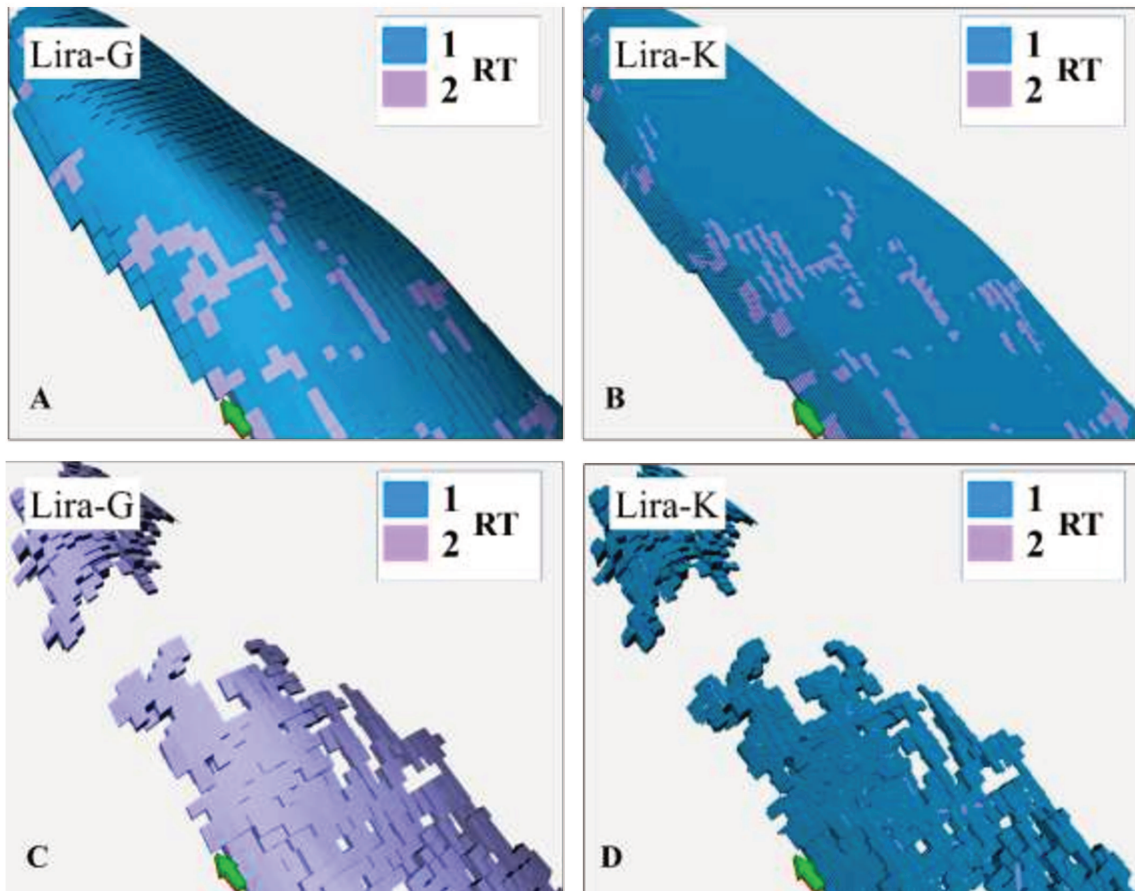


Figure 5.18 Determination of the RT percentage of the Lira-K contained in the blocks RT = 2 in Lira-G

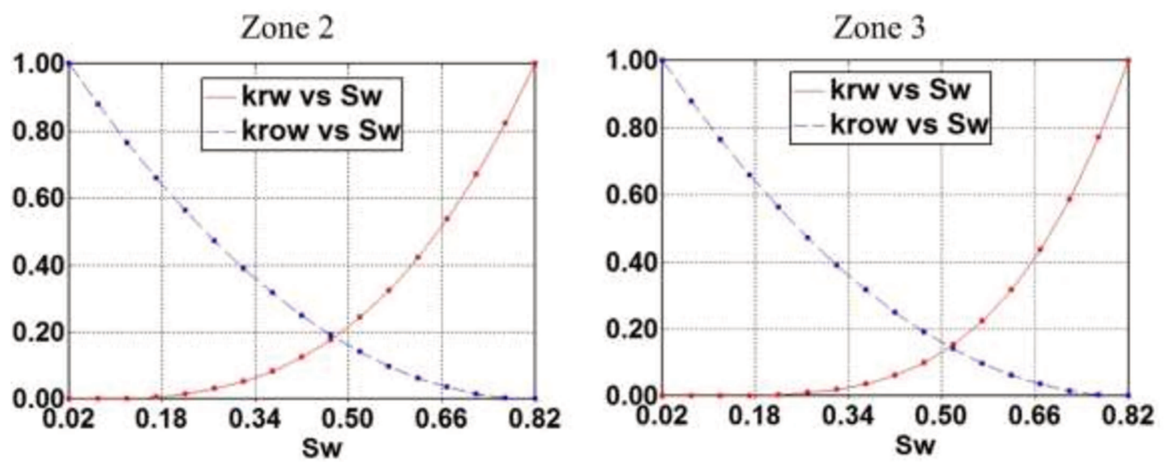


Figure 5.19 Relative permeability pseudo-curve used for RT=2 in Lira-G.

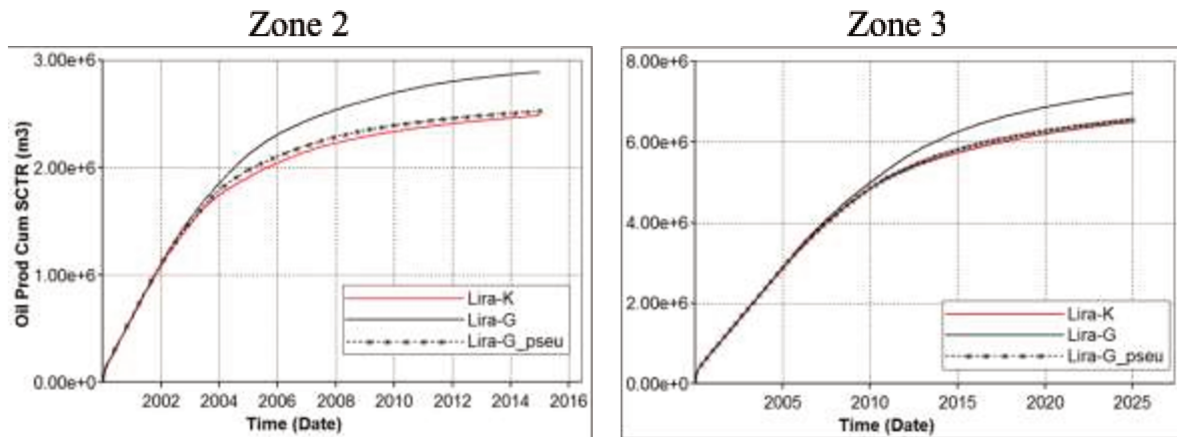


Figure 5.20 Comparison of cumulative oil production between Lira-K and Lira-G using the pseudo-curve of relative permeability for $RT=2$ in Lira-G

5.5.1 Validation of Lira-S

In this stage, we compare the dynamic results between Lira-G and Lira-S. The properties of the fluids and initialization parameters are the same used in Lira-K and Lira-G, applying the relative permeability pseudo-curves generated during the Lira-G adjustment process. The adjustment of the model is done in each zone separately, by comparing the response of the two models, Lira-G and Lira-S in the same way as was done in the Lira-G validation process.

For Zone 1, without the presence of karst, the adjustment is made in the curve of $RT = 1$ varying the shape of the curve and maintaining the same points of S_{wc} and S_{or} .

For Zone 2 and Zone 3, the adjustment is made first for $RT = 1$, which represents the matrix. For this are used a region of Lira-G and Lira-S without the influence of karst. The adjustment is made by modifying the shape of the curve using the same points of S_{wi} and S_{or} .

For the blocks with $RT = 2$ in Lira-S, the adjustment is made first in the S_{wi} and S_{or} points calculating the RT weighted average, in the same way as it is done in the validation process of lira-G. In Zone 2 the percentage of $RT = 1$ is 61% and $RT = 2$ is 39%, with $S_{wi} = 0.12$ and $S_{or} = 0.2$. For Zone 3 the percentage of $RT = 1$ is 56% and $RT = 2$ is 44%, with $S_{wc} = 0.1$ and $S_{or} = 0.2$. Figure 5.21 to Figure 5.23 show the relative permeability pseudo-curves applied in Zone 1, 2 and 3 respectively. The results of the application of the curves are shown in Chapter 6.

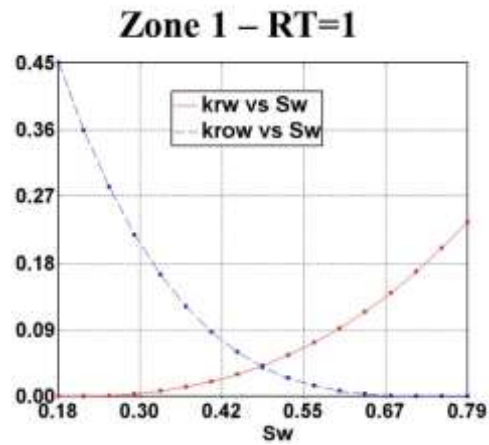


Figure 5.21 Relative permeability curve used in Lira-S for Zone 1

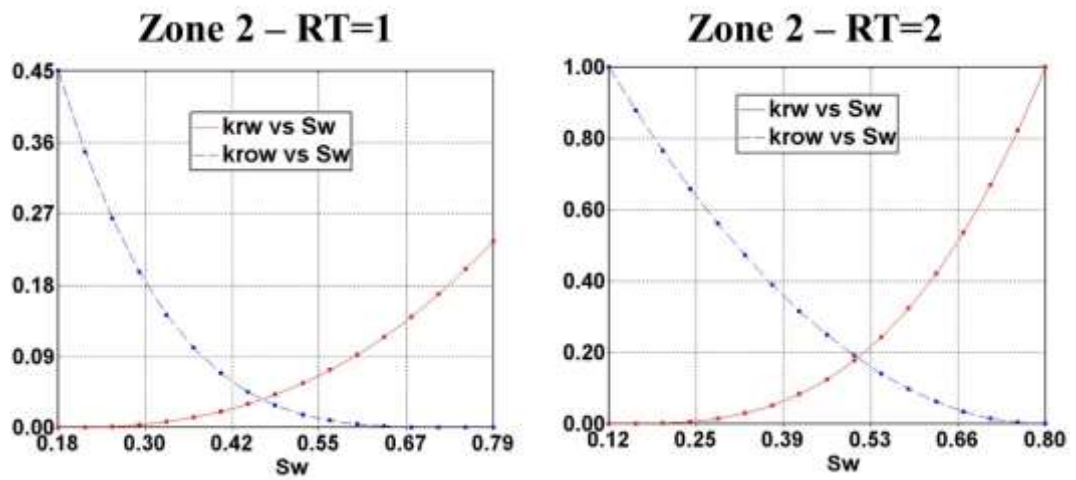


Figure 5.22 Relative permeability curves used in Lira-S for Zone 2

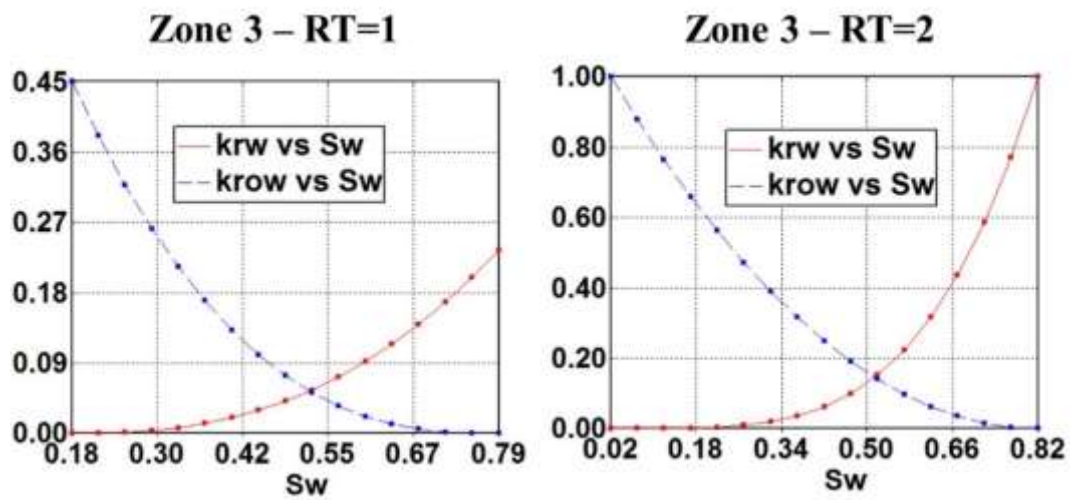


Figure 5.23 Relative permeability curves used in Lira-S for Zone 3

Finally, are compared maps of water saturation at different years of simulation, between Lira-G and Lira-S in Zones 1, 2 and 3. The resulting maps are presented and discussed in the next section.

6 RESULTS AND DISCUSSIONS

In this section we present Lira-M, Lira-K, Lira-G and Lira-S models. First, Lira-M is presented, showing the spatial distribution and the values obtained. Subsequently, Lira-K presentation is made, showing the results of the upscaling process and its integration with Lira-M to generate Lira-G. The adjustments obtained in the validation zones during the upscaling process, together with the water saturation maps, are presented too. Finally, the results for the Lira-S model, the global distribution and values of properties and the validation of the upscaling process are shown.

6.1 Lira-M

Figure 6.1 shows the spatial distribution of facies model in Lira-M at top of Zones 1, 2 and 3. Zone 1 and 2 present microbial carbonates, wackestone, mudstone, and shale. Zone 3 presents coquinas, wackestone, mudstone, and shale.

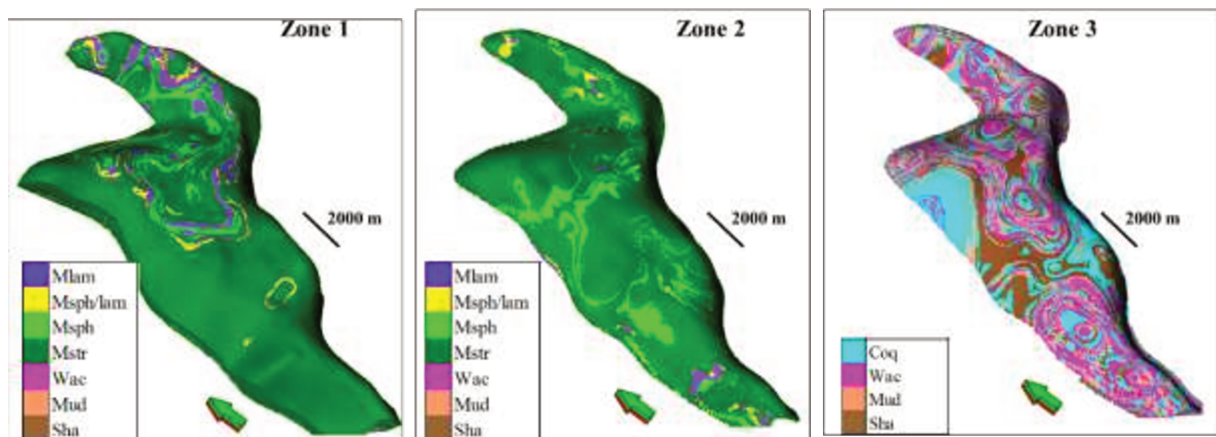


Figure 6.1 Facies model in Lira-M.

Figures 6.2 to 6.4 show the cross plot of permeability against porosity for the three zones. Figures 6.5 to 6.7 present vertical cross sections showing the facies, porosity and permeability distribution in Zones 1, 2 and 3 respectively. These images describe the general behavior of the properties for each zone in the field.

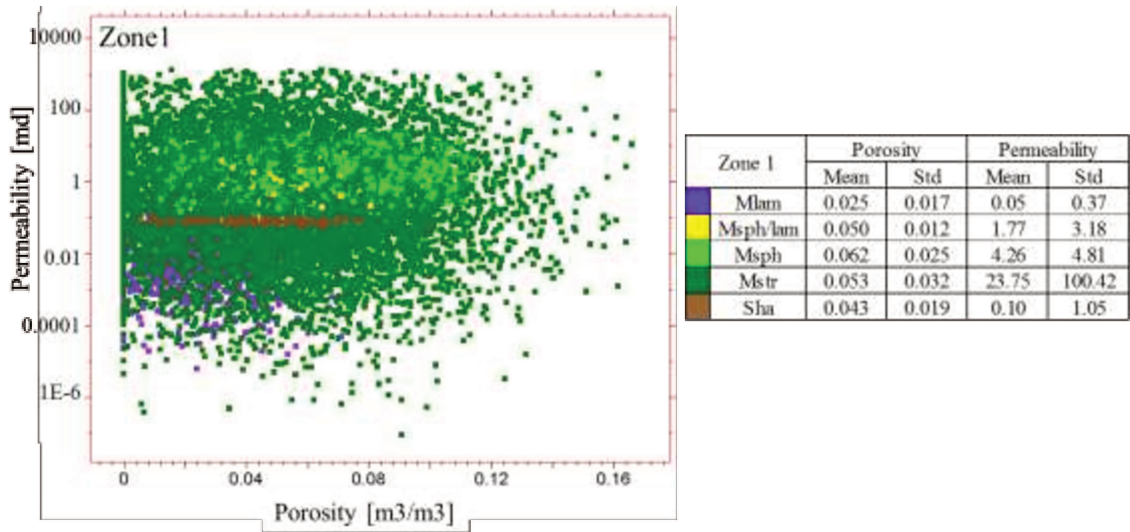


Figure 6.2 Crossplot of porosity and permeability by facies for Zone 1 in Lira-M

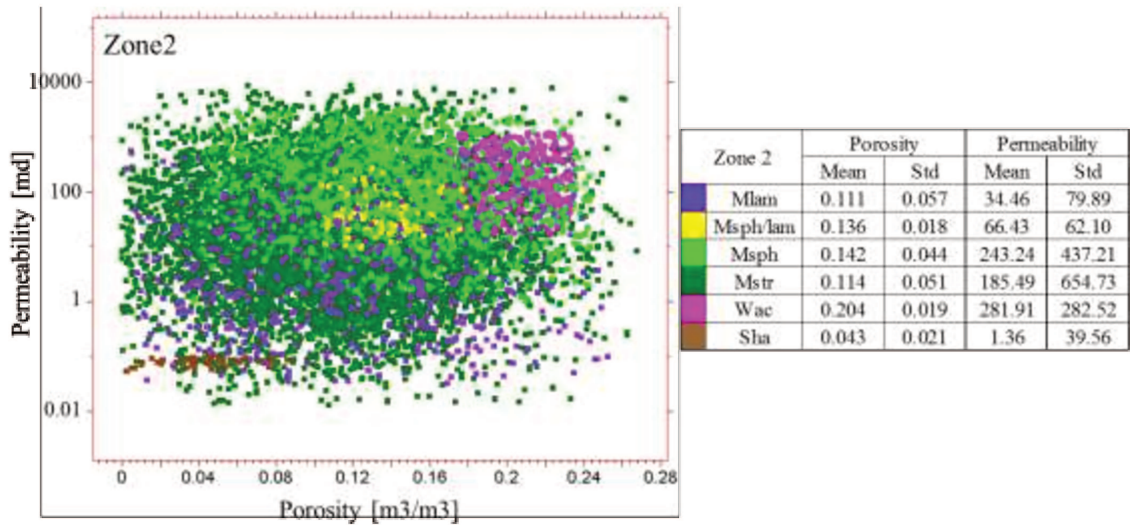


Figure 6.3 Crossplot of porosity and permeability by facies for Zone 2 in Lira-M

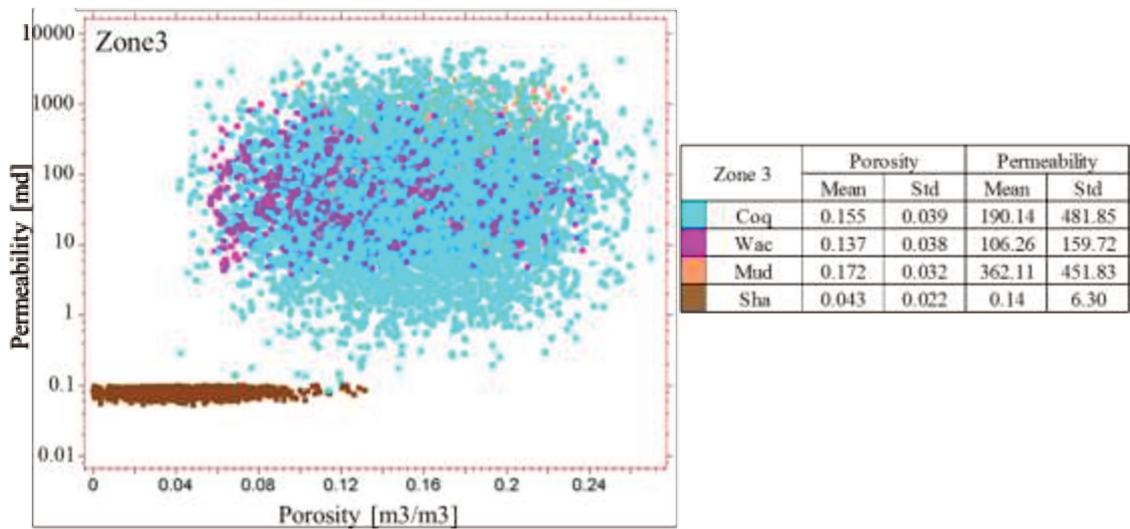


Figure 6.4 Crossplot of porosity and permeability by facies for Zone 3 in Lira-M

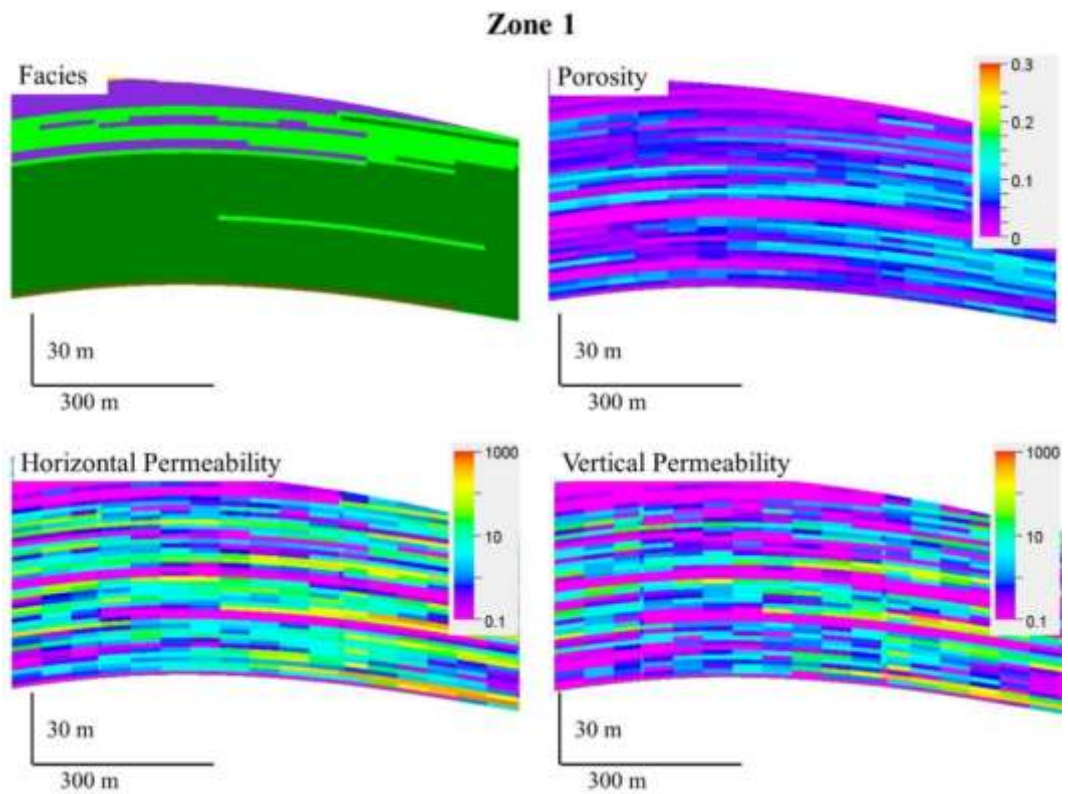


Figure 6.5 Cross section showing the facies, porosity and permeability of Lira-M in Zone 1

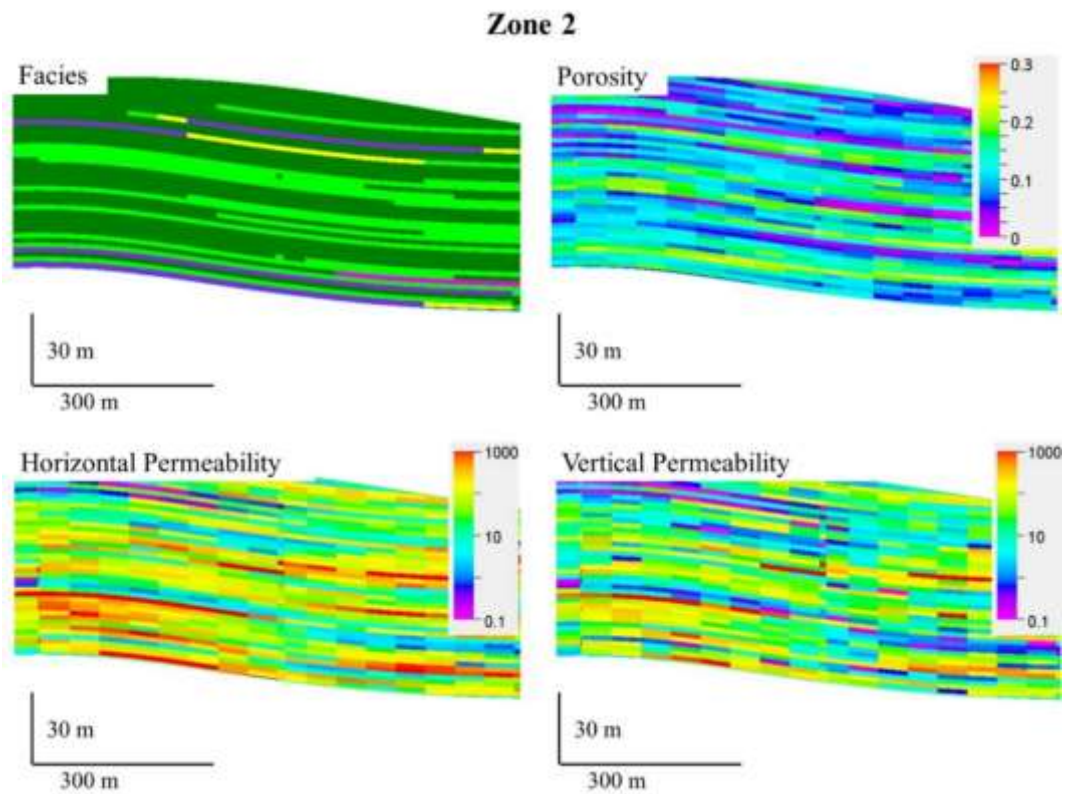


Figure 6.6 Cross section showing the facies, porosity and permeability of Lira-M in Zone 2

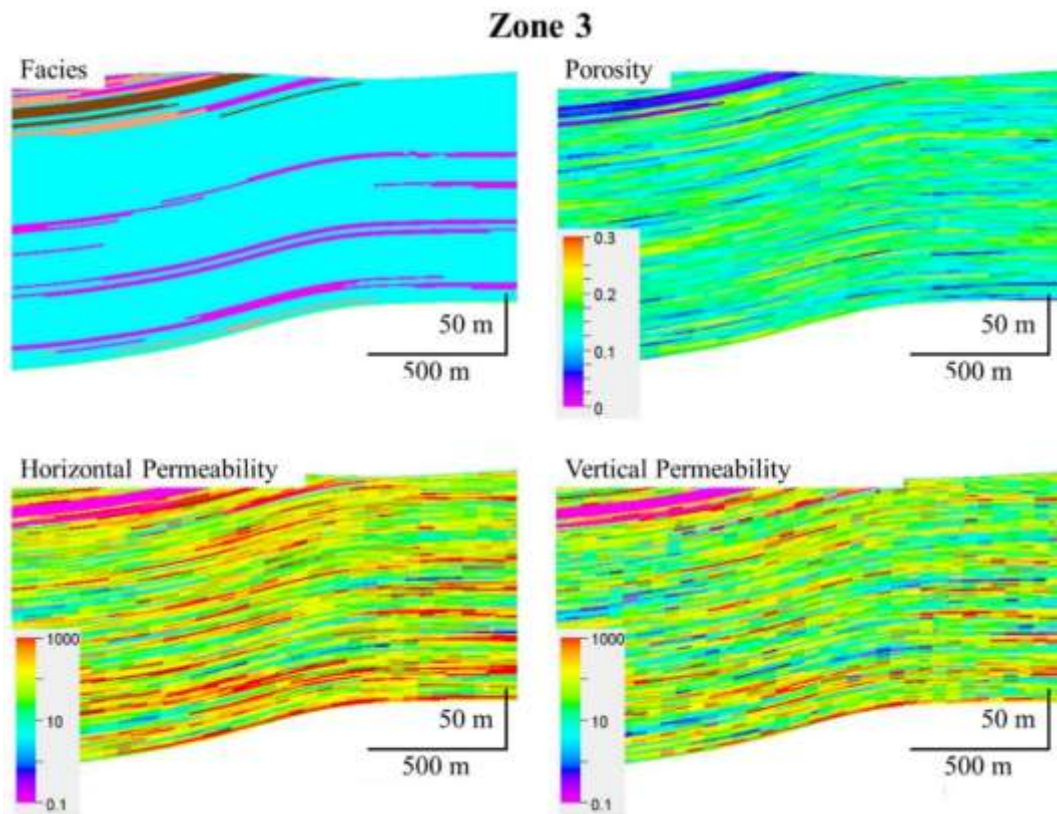


Figure 6.7 Cross section showing the facies, porosity and permeability of Lira-M in Zone 3

Higher values for permeability are presented in Zone 3. Zone 3 also shows a presence of shale, which is characterized by low permeability values. These extensively distributed shale layers can generate vertical flow barriers (Figure 6.7). Zone 2 also shows good average property values, although these are lower than those in Zone 3. Zone 1 presents the lowest average quality for the entire field.

6.2 Lira-K

As described in the application section, this grid is smaller and has a higher resolution than Lira-M. Figure 6.8 shows the grid of Lira K in zones 2 and 3.

Figure 6.9 and 6.10 show porosity and permeability distribution and property histograms of Lira-K in Zone 2. Figure 6.11 and 6.12 present property distribution and histograms respectively for Zone 3. The generated model presents the karsts with different sizes and spatial distribution, which communicate with a heterogeneous matrix.

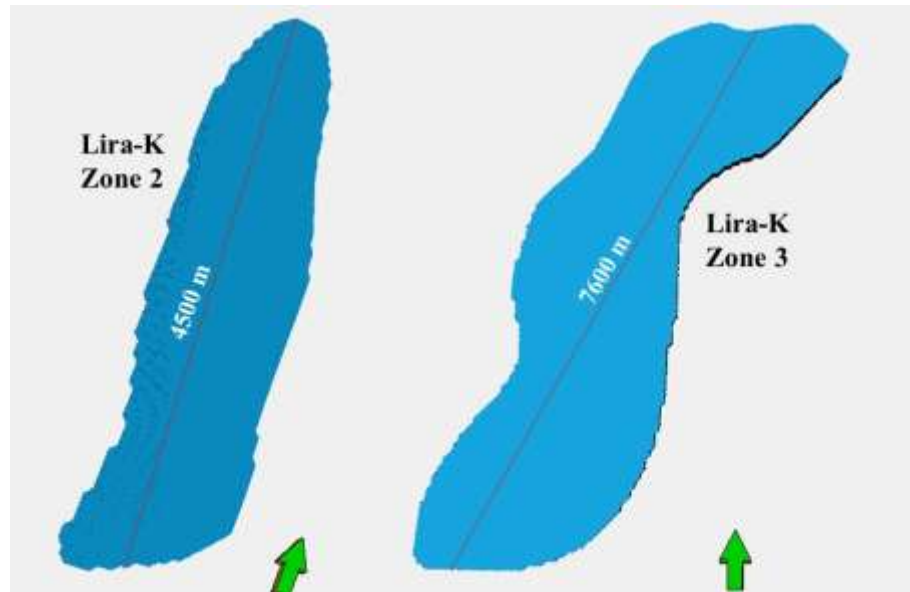


Figure 6.8 Grid of Lira-K developed in Zone 2 and Zone 3

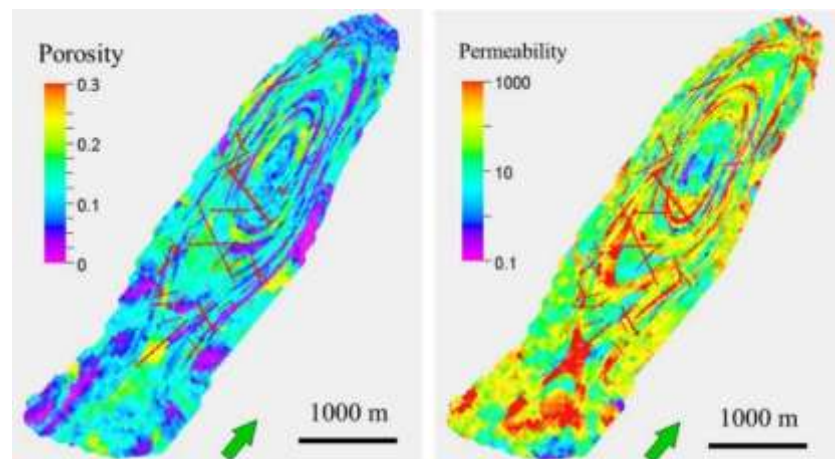


Figure 6.9 Lira-K porosity and permeability model in Zone 2

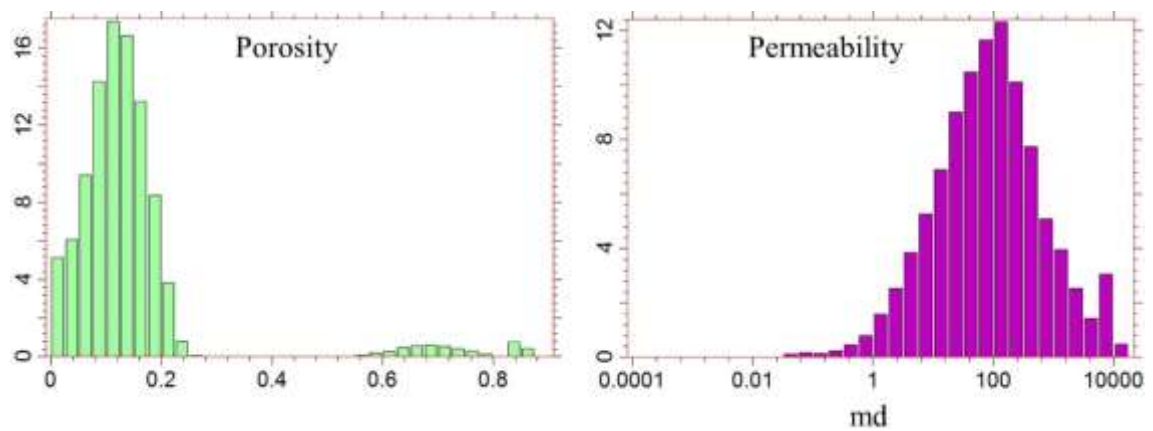


Figure 6.10 Porosity and permeability histograms for Zone 2 of Lira-K

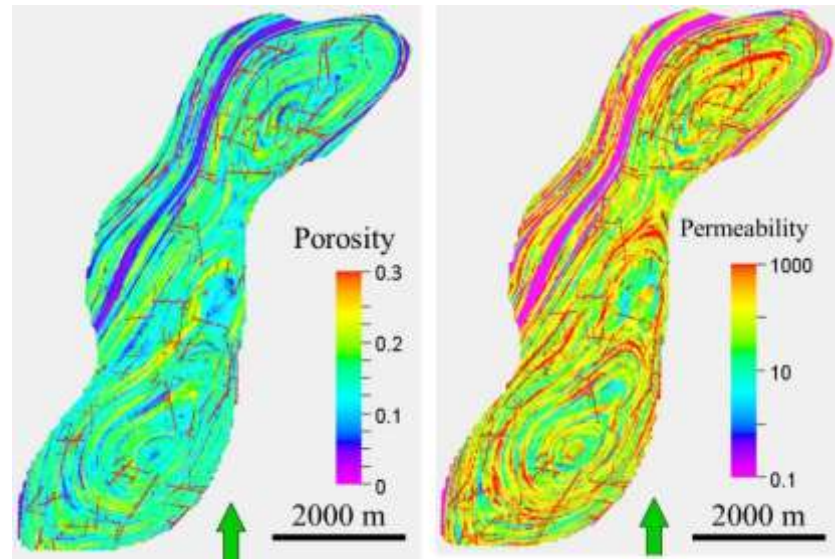


Figure 6.11 Facies distribution in karst system for Zone 3 of Lira-K

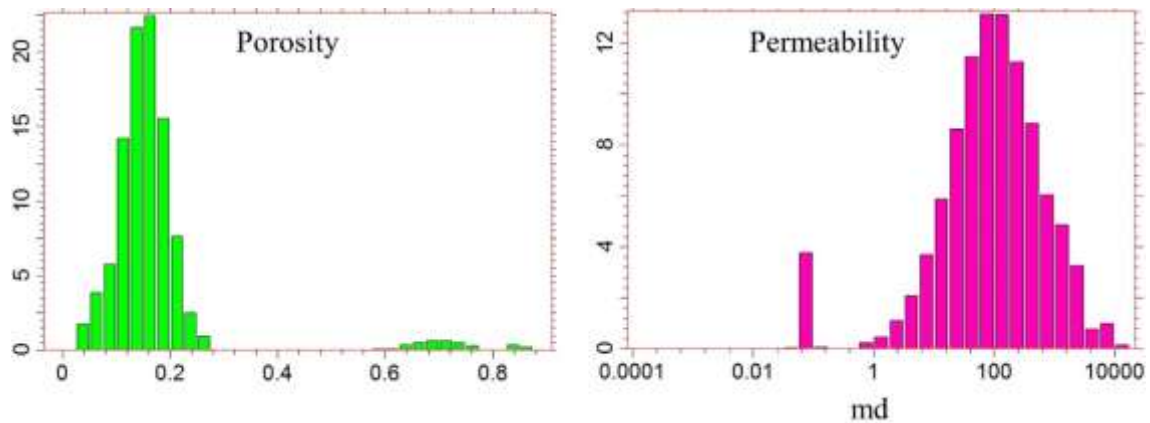


Figure 6.12 Porosity and permeability histograms for Zone 3 of Lira-K

6.3 Lira-G

The upscaling process is carried out from both zones of Lira-K up to the Lira-G. The upscale of RT is necessary to assign relative permeability curves during the numerical simulation. The spatial distribution of RT in both the fine and coarse grids is almost similar for zones 2 and 3, as shown in Figure 6.13 and Figure 6.14.

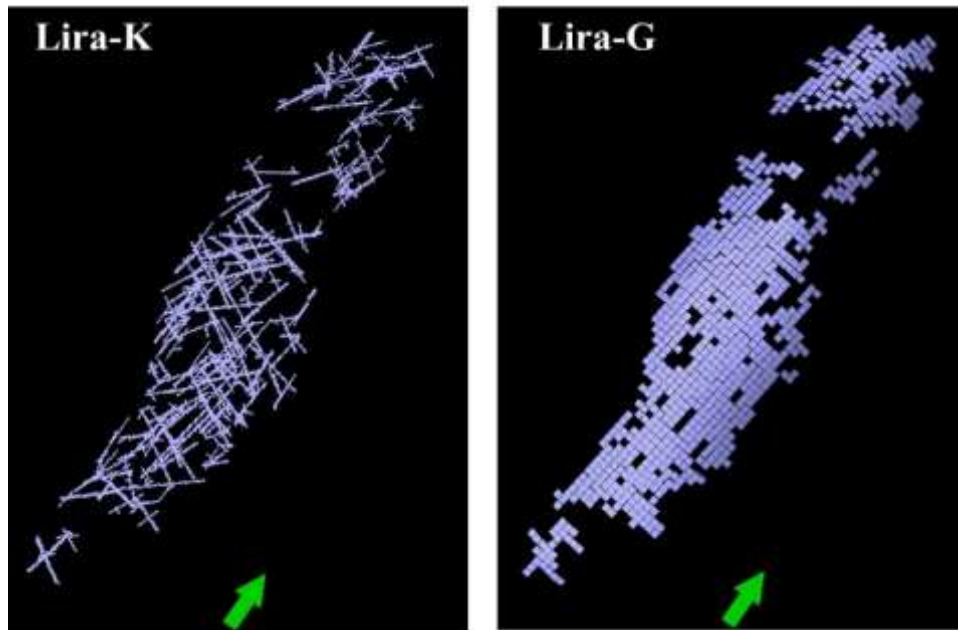


Figure 6.13 RT=2 upscaled from Lira-K to Lira-G in Zone 2

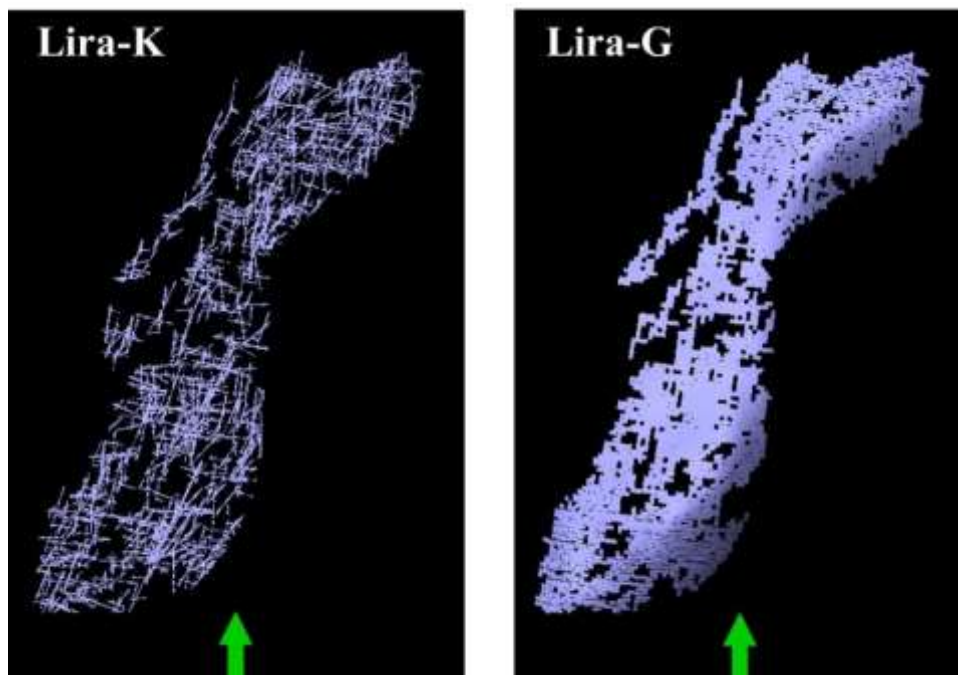


Figure 6.14 RT=2 upscaled from Lira-K to Lira-G in Zone 3

Figure 6.15 shows the histograms of porosity of Lira-K and Lira-G in validation Zones 2 and 3. In the histograms, porosity values above those presented in Lira-M are identified, which represent the influence of the karst in the upscaled model.

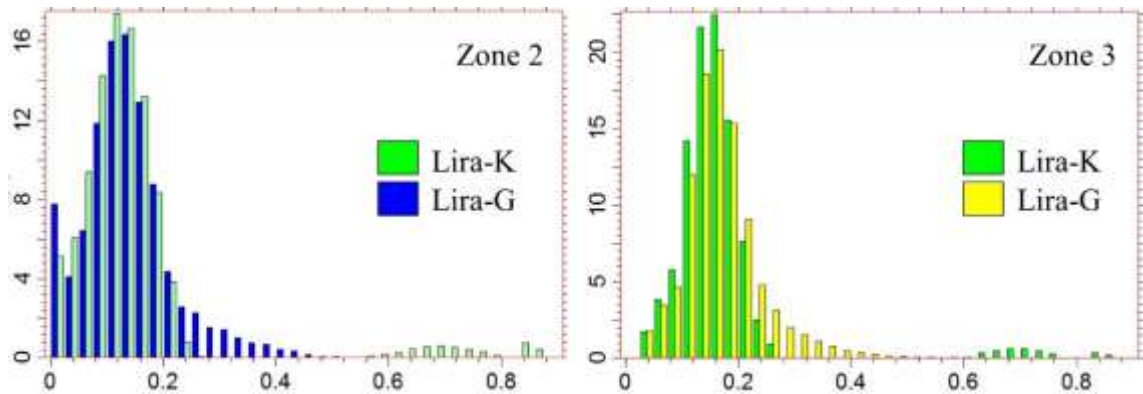


Figure 6.15 Porosity histograms for Lira-K and Lira-G in zones 2 and 3.

Figure 6.16 shows the histogram of porosity with highlighted porosity of RT=1 and RT=2 in Lira-G, as compared to Lira-K, for Zone 2. From the histograms, it is observed that porosity values above the recorded for RT = 1 are presented. These values are related to the influence of karsts. A clear cutoff between RT = 2 and RT=1 in Lira G is not differentiated, although the karst rock type in Lira-G presents the trend to higher values in properties.

A similar behavior is observed for porosity in Zone 3 (Figure 6.17).

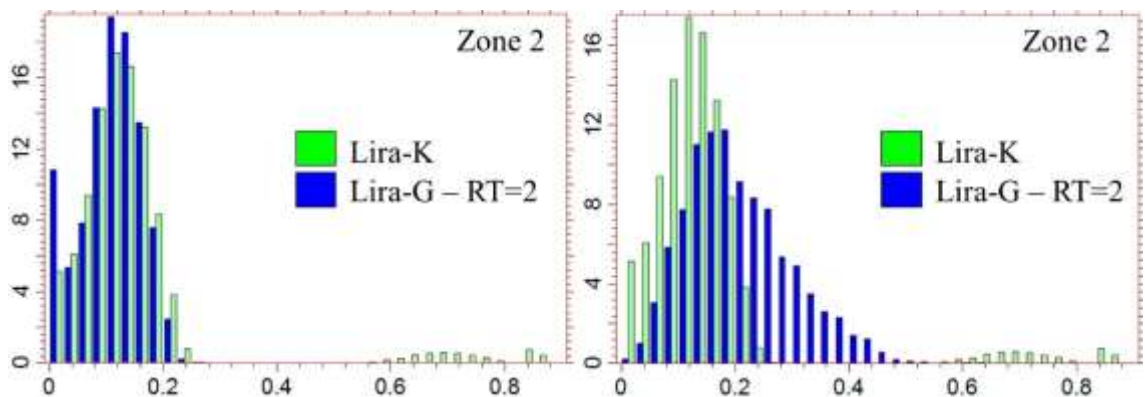


Figure 6.16 Comparison of porosity between Lira K and Lira-G RT=1 (left) and Lira-G RT=2 (right) in Zone 2.

Figure 6.18 shows the comparative histogram for permeability in validation zones 2 and 3. The karstic influence on permeability in Lira-G is presented in Figure 6.19 and Figure 6.20, for Zone 2 and Zone 3 respectively, in the same way as it was done for porosity in Figures 6.16 and 6.17. For validation of permeability upscale, the dynamic comparison based on flow simulation is necessary and is present in the next section.

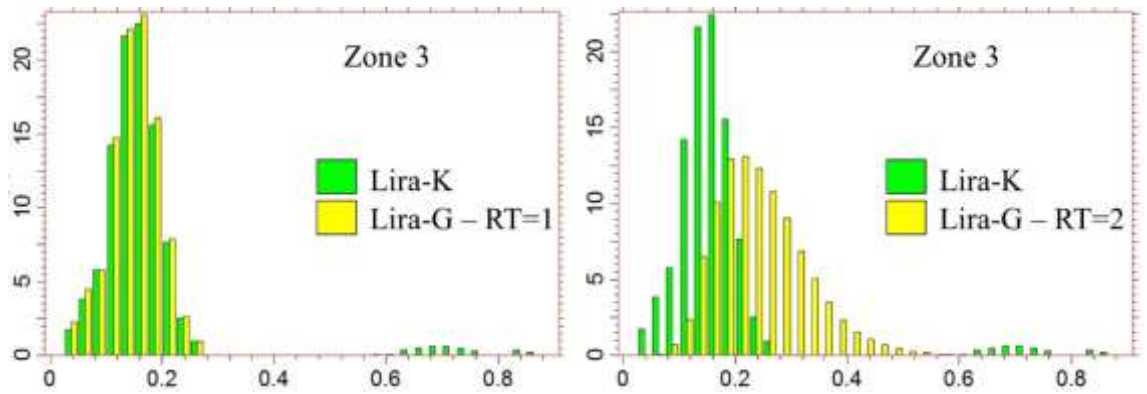


Figure 6.17 Comparison of porosity between Lira K and Lira-G RT=1 (left) and Lira-G RT=2 (right) in Zone 3.

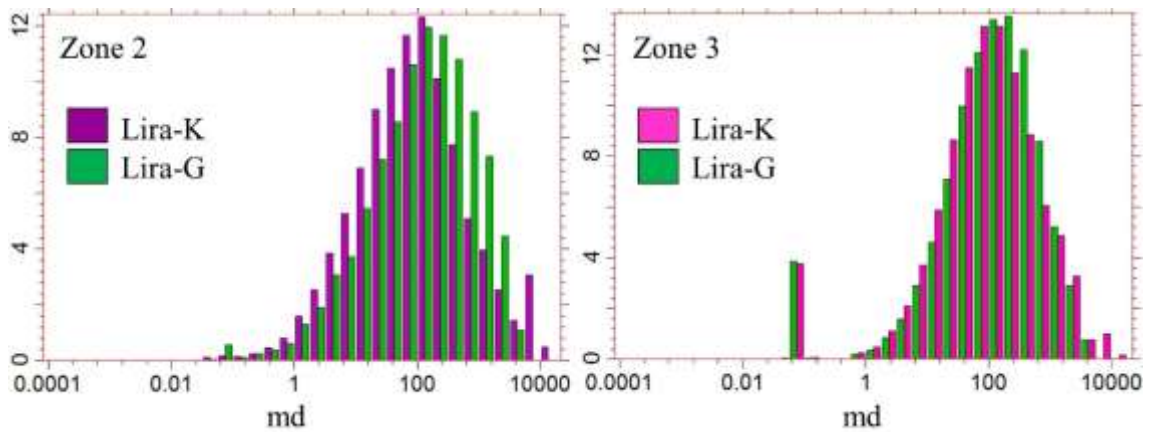


Figure 6.18 Permeability histograms for Lira-K and Lira-G in zones 2 and 3.

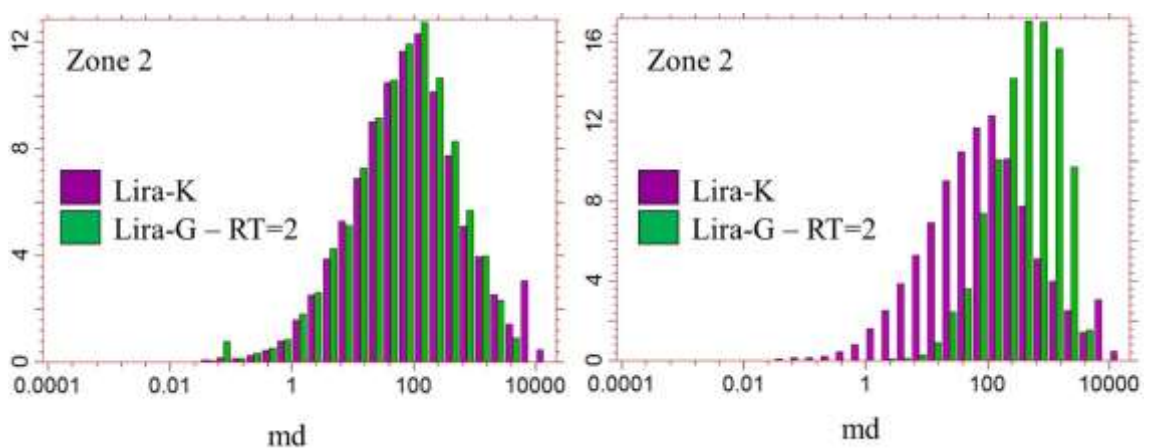


Figure 6.19 Comparison of permeability between Lira K and Lira-G RT=1 (left) and Lira-G RT=2 (right) in Zone 2.

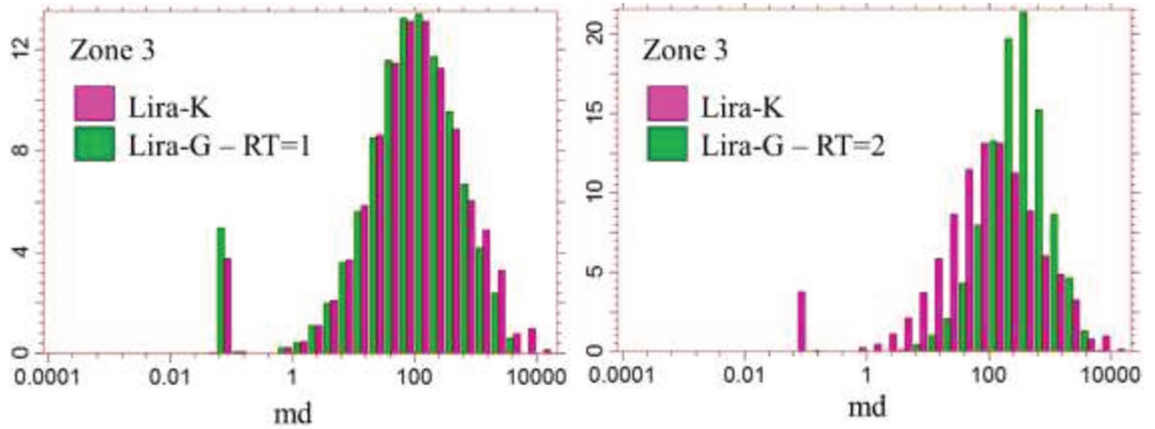


Figure 6.20 Comparison of permeability between Lira K and Lira-G RT=1 (left) and Lira-G RT=2 (right) in Zone 3.

Figure 6.21 shows the cross plot of porosity and permeability of Lira-G of Karst regions in Zone 2 and 3, highlighting the rock type (Karst - Matrix). The influence of karsts in Lira-G can be observed again without differentiating a clear cutoff, but showing a general trend to high values for porosity and permeability.

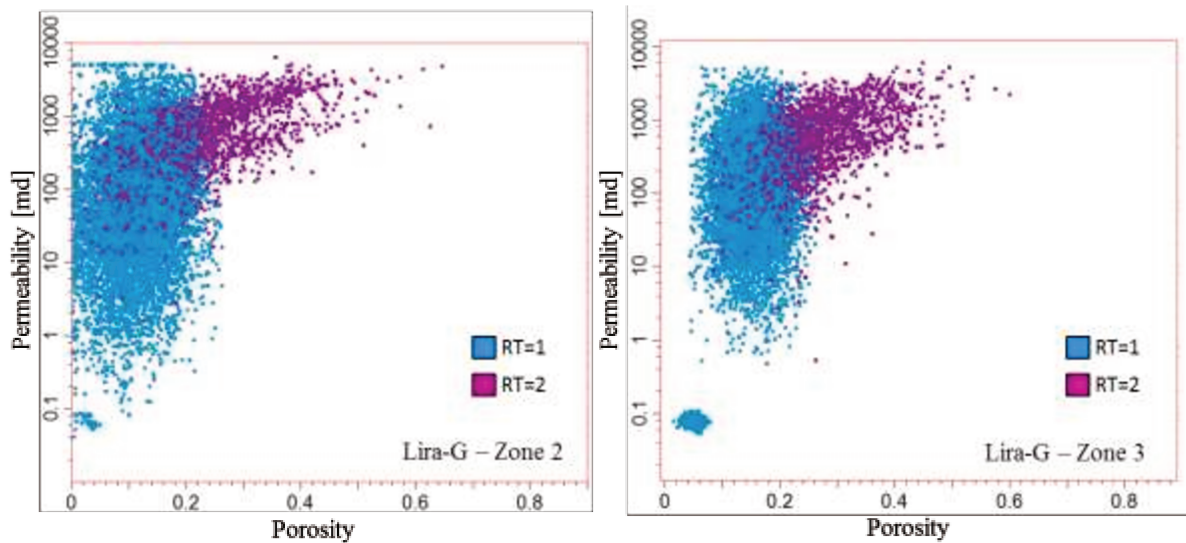


Figure 6.21 Crossplot of porosity and permeability by rock type in validation zones 2 and 3 in Lira-G.

The integration of models is the final step for generating Lira-G. Figure 6.22 and Figure 6.23 present cross sections for Lira-G in the regions of Lira-K in Zone 2 and Zone 3, respectively. It is possible to notice the highlights of karst features in the distribution of rock type, porosity, and permeability.

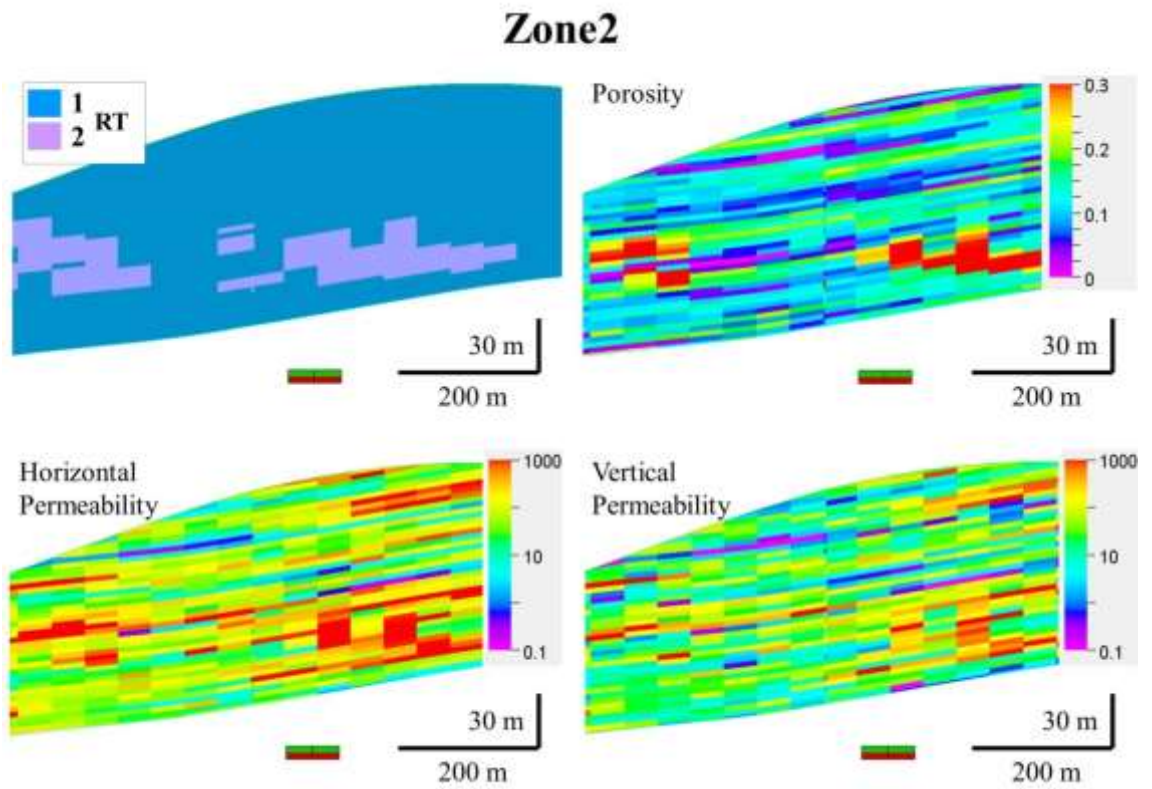


Figure 6.22 NS cross section of Lira-G showing karstic influence in Zone 2

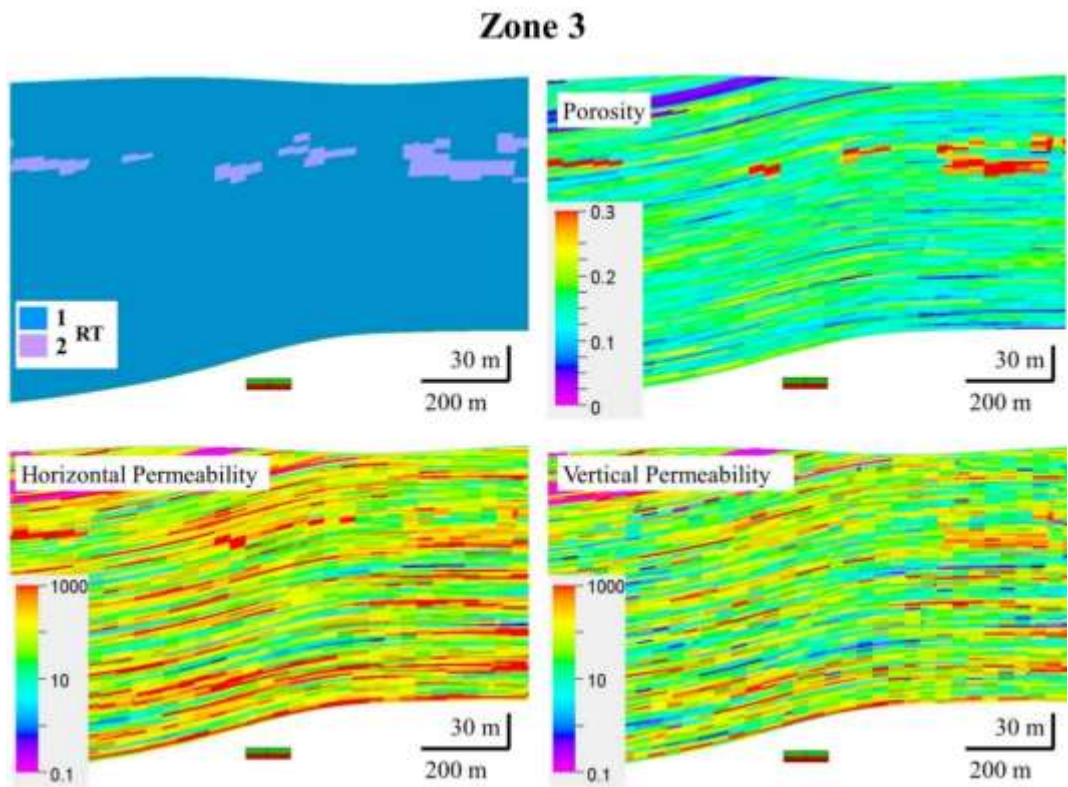


Figure 6.23 NS cross section of Lira-G showing karstic influence in Zone 3

6.4 Validation of LIRA-G

The results of the validation process are presented in two main segments: (1) the application of the simulation model in Lira-K, and (2) the process of validation and flow adjustment.

6.4.1 Simulation in Lira-K

Figure 6.24 shows the water advance from the injector well in a selected area, in seven different times of the first 36 months of simulation, together with the horizontal permeability and rock type images for zone 2 of Lira-K grid.

Figure 6.25 presents the water advance in Lira-K for zone 3 as shown in Figure 5.24 for Zone 2.

The behavior in Lira-K, can be widely described as follows: (1) the water advances through the matrix (RT=1). (2) Once the water reaches the karsts elements (RT = 2) there is an exchange from matrix to karst, and an increase in water saturation and advance through karst and, (3) when the karstic element is saturated with water, the karst-to-matrix fluid exchange occurs. It can also be observed that karst behaves as a connector between zones of high permeability which are separated according to the facies model.

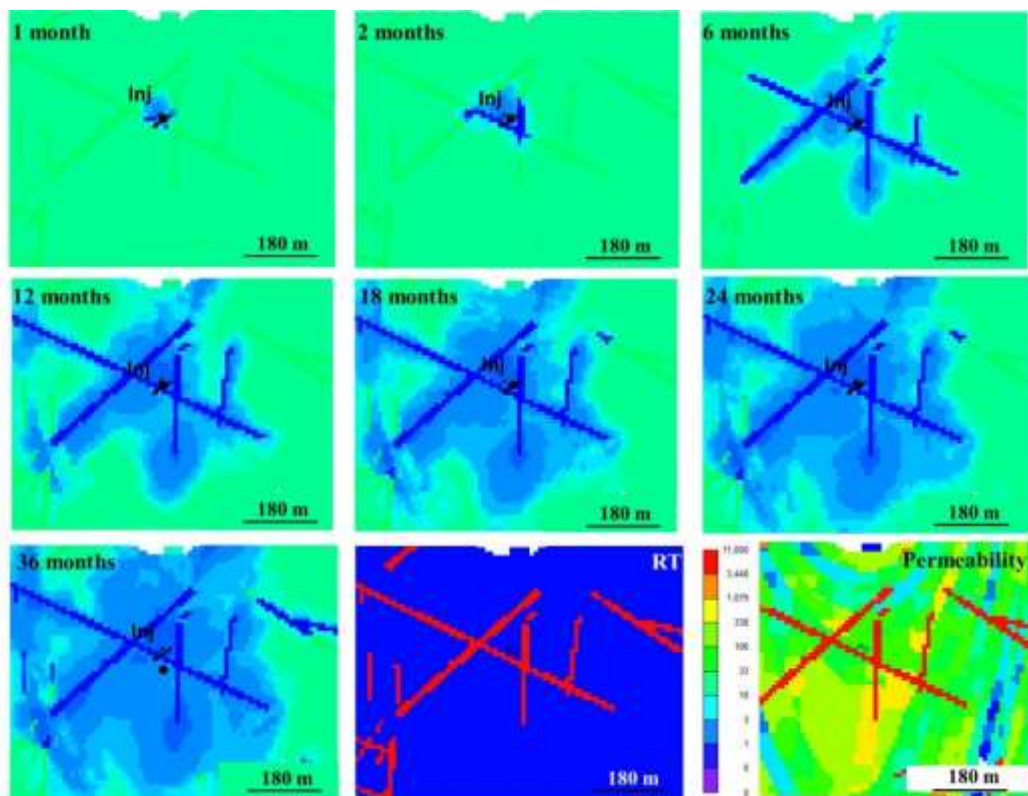


Figure 6.24 Flow simulation on the Lira-K in Zone 2

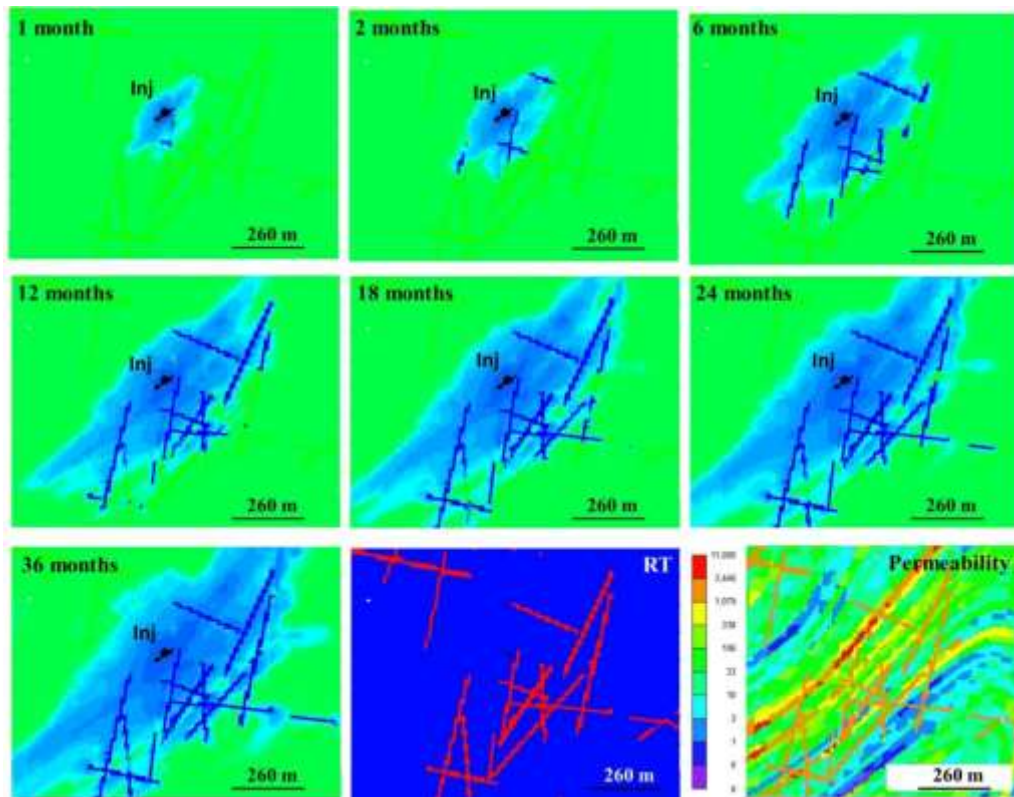


Figure 6.25 Flow simulation on the Lira-K in Zone 3

6.4.2 Flow adjustment

It can be seen in Table 6.1 that porous volume in Lira-G in the regions selected for validating process remained almost unchanged compared to Lira-K.

Table 6.1 Comparison of zones selected for validation of Lira-G

Zone	Grid	Active blocks	Pore Vol [m ³]	% volume error
Zone 2	Lira-K2	611113	8874200	0.94
	Lira-G2	12425	8957326	
Zone 3	Lira-K3	1709184	29009690	1.21
	Lira-G3	35826	29360850	

The use of the pseudo-curves of relative permeability generated for RT=2 in Lira-K produces a good match with the reference solution when comparing different reservoir parameters. Figure 6.26 and 6.27 compare the results obtained from the simulations in Lira-K and Lira-G for zones 2 and 3 respectively.

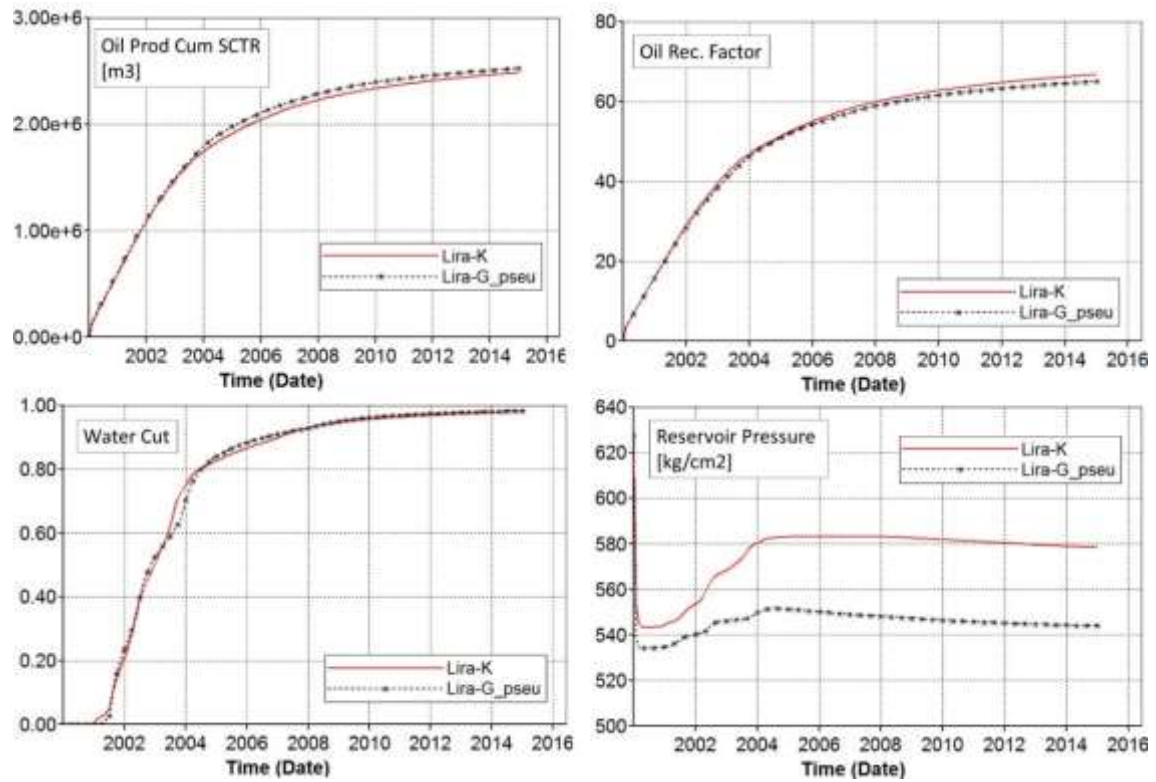


Figure 6.26 Reservoir pressure, oil production, water cut and oil rate comparing the Lira-K and Lira-G in Zone 2 after validation

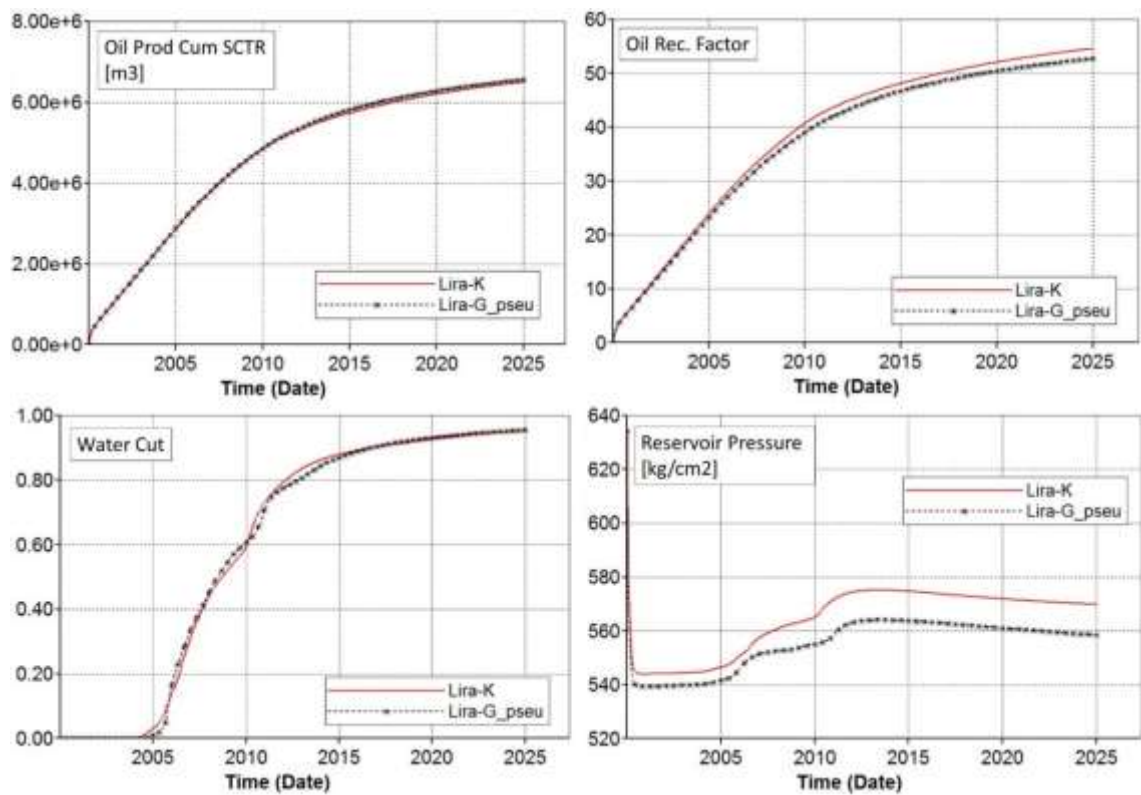


Figure 6.27 Reservoir pressure, oil production, water cut and oil rate comparing the Lira-K and Lira-G in Zone 3 after validation

Figure 6.28 to Figure 6.30 compare profiles of water saturation between Lira-K and Lira-G in Zone 2 at six months, five years and ten years of simulation respectively, in a horizontal cut at 5260 meters depth.

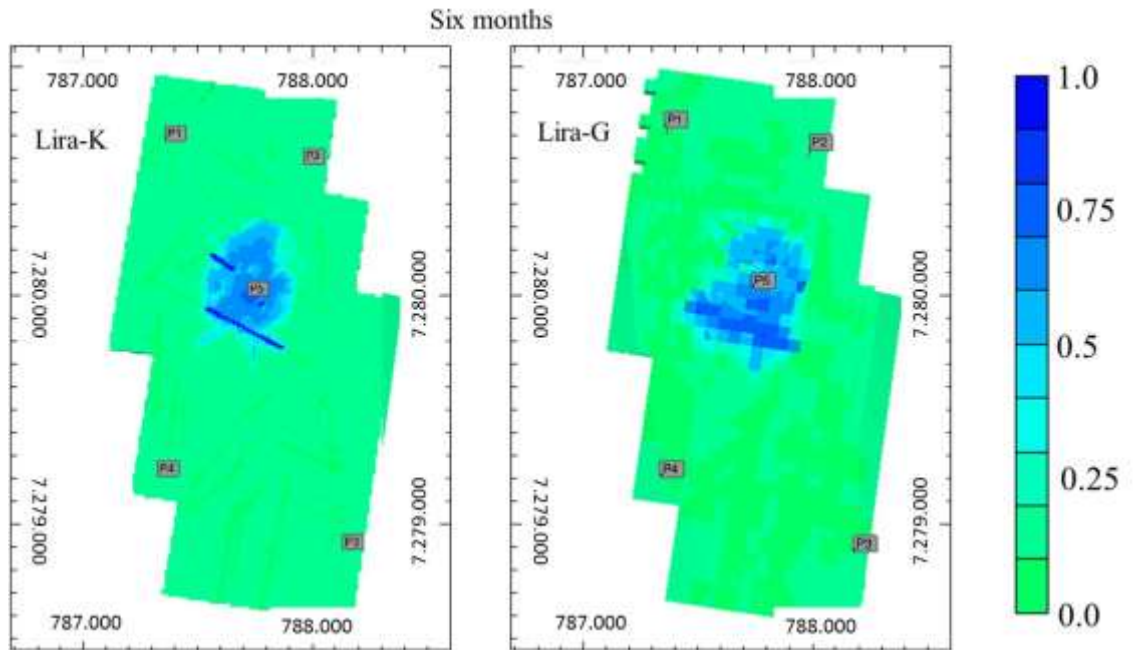


Figure 6.28 Comparison of water saturation between Lira-K and Lira-G in Zone 2 at six months of simulation.

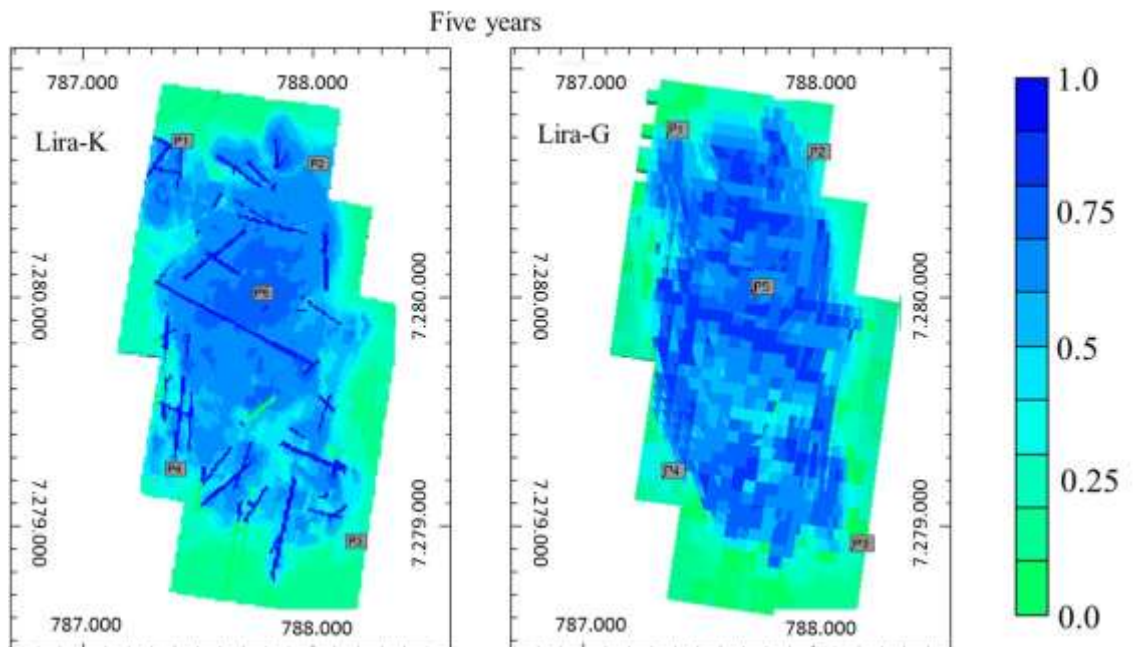


Figure 6.29 Comparison of water saturation between Lira-K and Lira-G in Zone 2 at five years of simulation

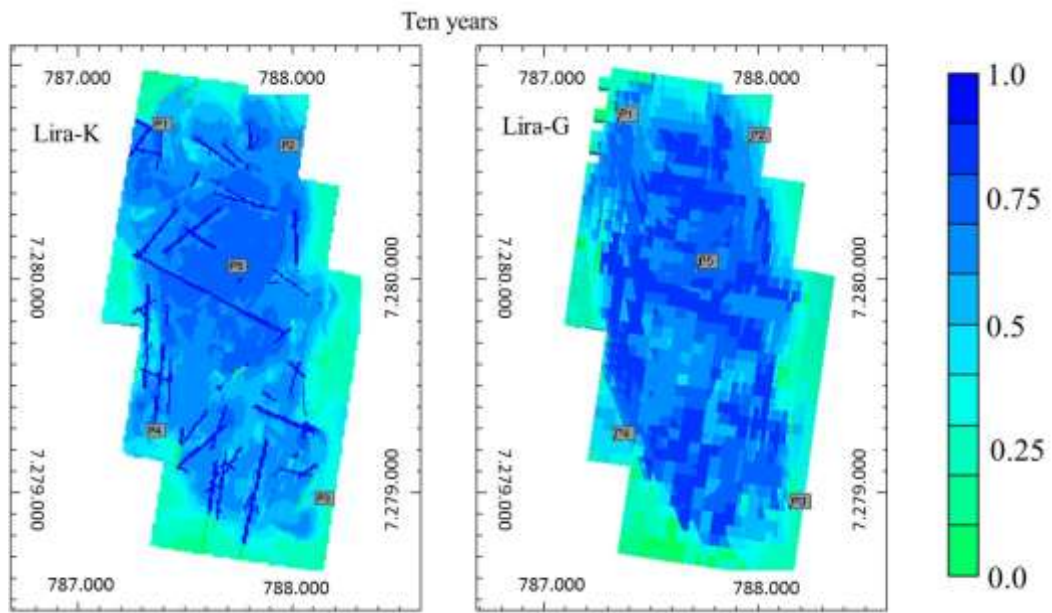


Figure 6.30 Comparison of water saturation between Lira-K and Lira-G in Zone 2 at ten years of simulation

Figure 6.31, Figure 6.32 and Figure 6.33 show the water saturation in Lira-K and Lira-G in Zone 3 at six months, five years and ten years of simulation respectively, in a horizontal cut at 5350 meters depth.

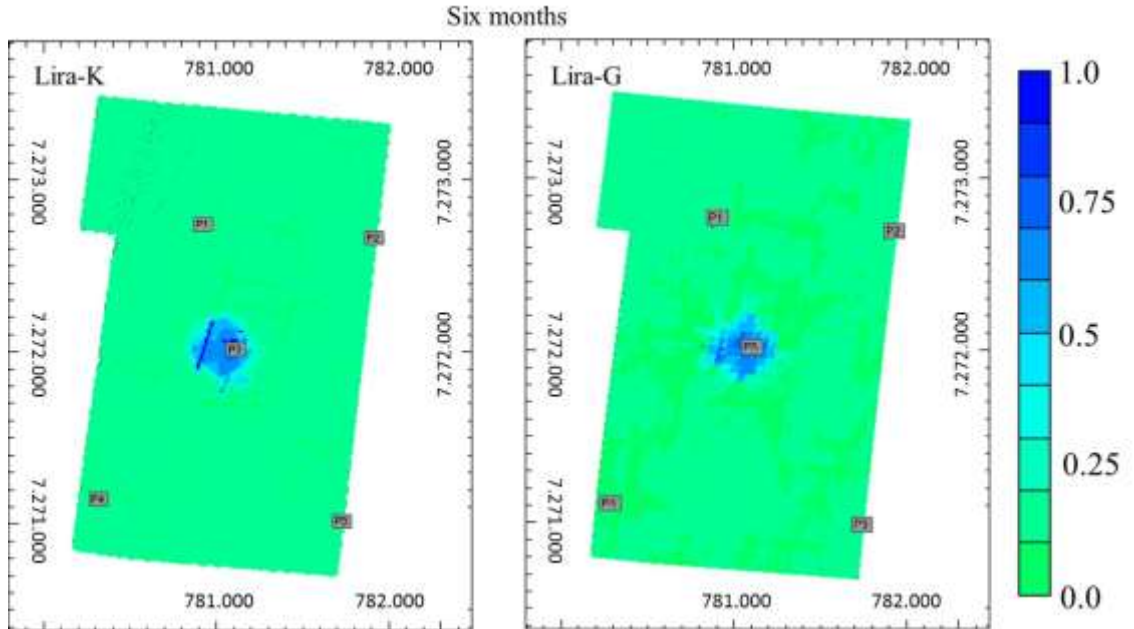


Figure 6.31 Comparison of water saturation between Lira-K and Lira-G in Zone 3 at six months of simulation

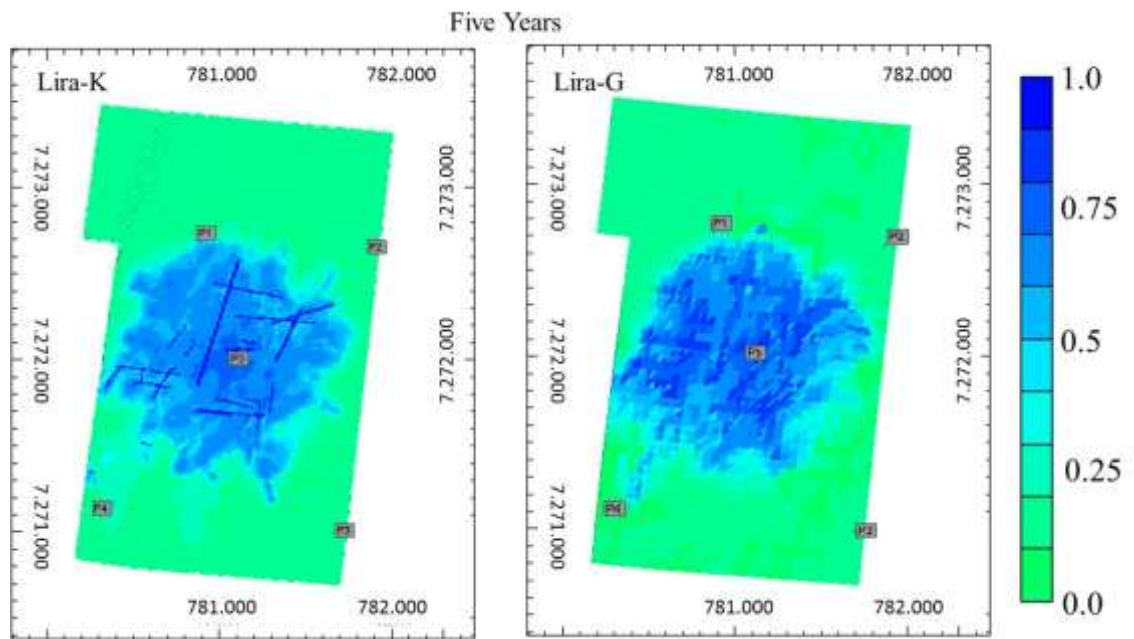


Figure 6.32 Comparison of water saturation between Lira-K and Lira-G in Zone 3 at five years of simulation

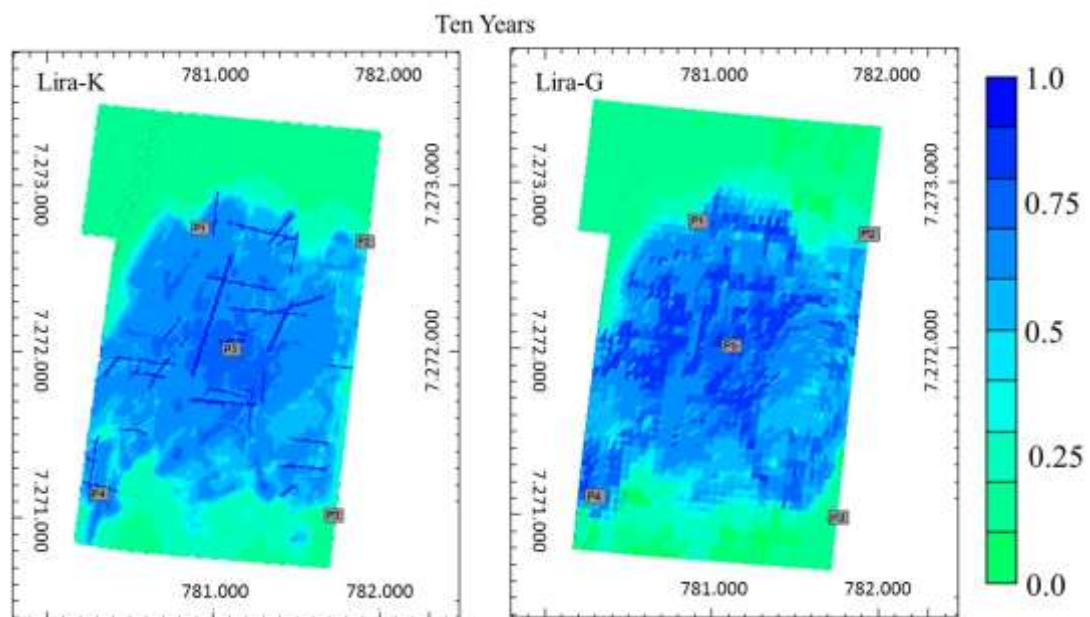


Figure 6.33 Comparison of water saturation between Lira-K and Lira-G in Zone 3 at ten years of simulation

When comparing the distribution of the saturation in Lira-K with Lira-G it is observed that the two models show very similar behavior, in the two zones. A good match with respect to oil production, water cut, and oil rate is achieved for the field. As with Lira-K, Lira-G presents water advance related to (1) permeability matrix, (2) water saturation in karst, and (3) karst-to-matrix and matrix-to-karst fluid exchanges.

The validation process of Lira-G shows good dynamic matching conserving reservoir production parameters. Considering the well production parameters, it is required a local

adjustment, based on a local approach of pseudo-curves and calibration of well index. (Figure 6.34 to 6.37). However, these steps were not addressed in this work. Future works on this model can focus on doing adjustment analysis per well when this type of heterogeneity is presented.

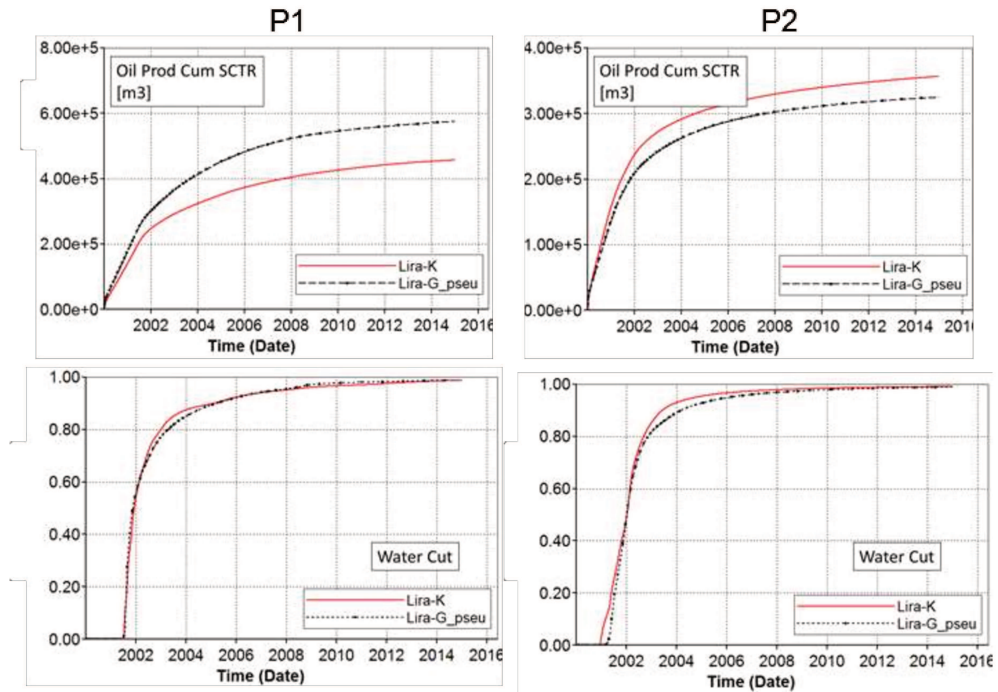


Figure 6.34 Oil production and water cut comparing production wells adjust in Lira-K and Lira-G in Zone 2 after validation.

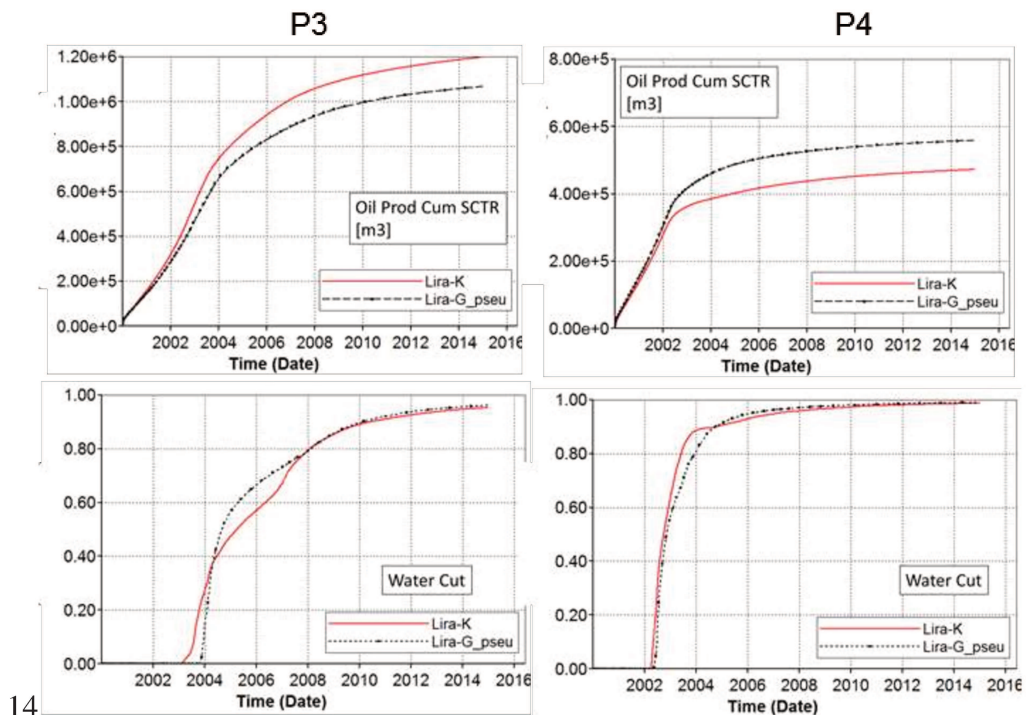


Figure 6.35 Oil production and water cut comparing production wells adjust in Lira-K and Lira-G in Zone 2 after validation.

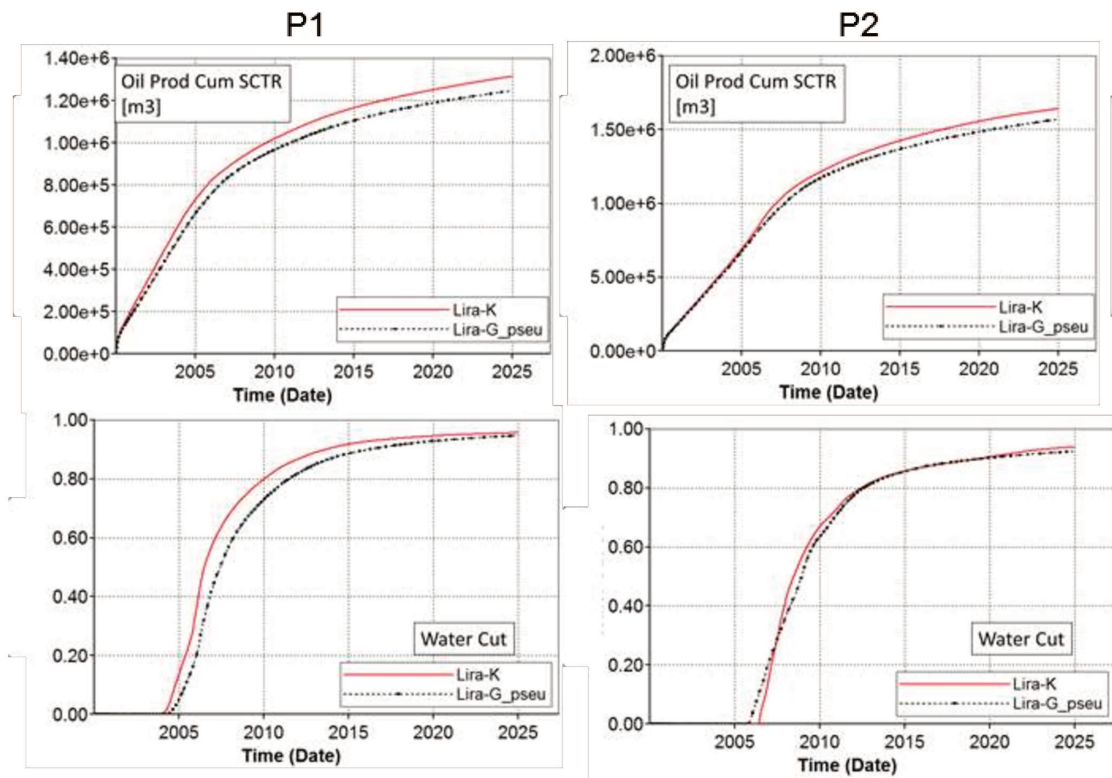


Figure 6.36 Oil production and water cut comparing production wells adjust in Lira-K and Lira-G in Zone 3 after validation.

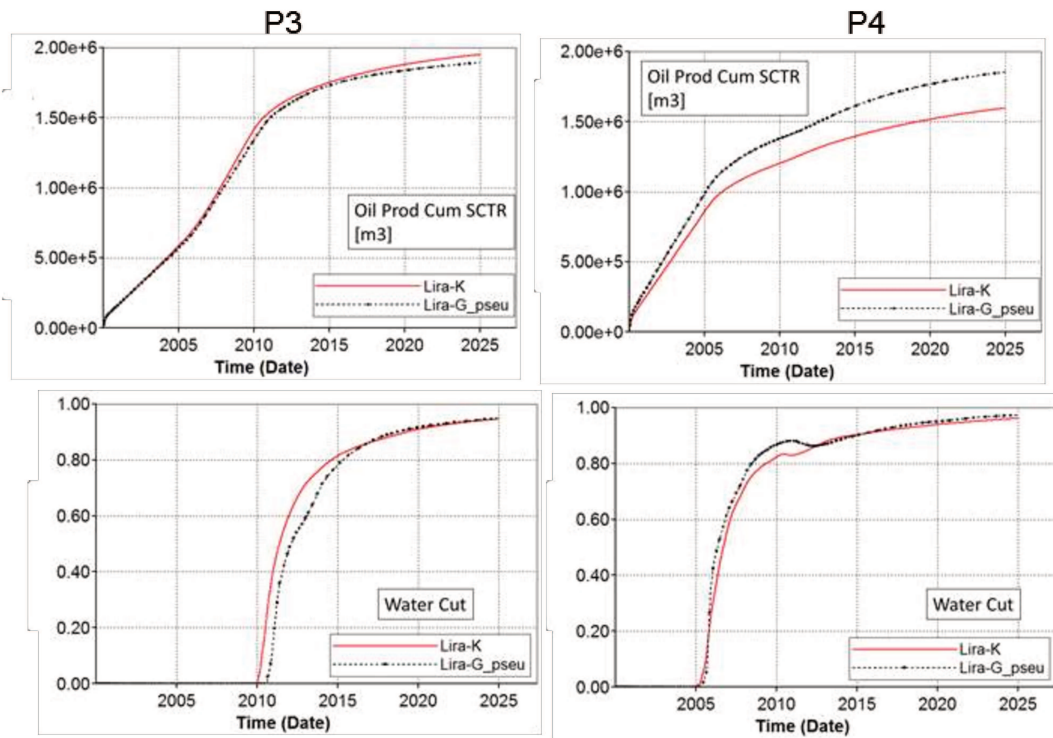


Figure 6.37 Oil production and water cut comparing production wells adjust in Lira-K and Lira-G in Zone 3 after validation.

6.5 Lira-S

Lira-S is the result of the upscaling of full Lira-G. This model decreases the total number of blocks while preserving the trend of the properties and the total porous volume.

Figure 6.38 and Figure 6.39 compare the porosity and permeability respectively, of a region of Lira-G and Lira-S with karst influence in Zone 2 and Zone 3.

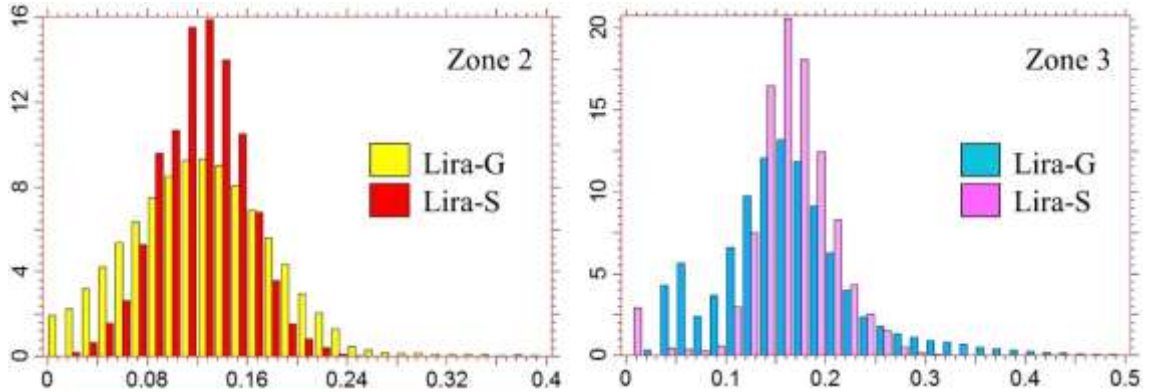


Figure 6.38 Porosity histograms comparing Lira-G and Lira-S in a region with karst influence in zones 2 and 3.

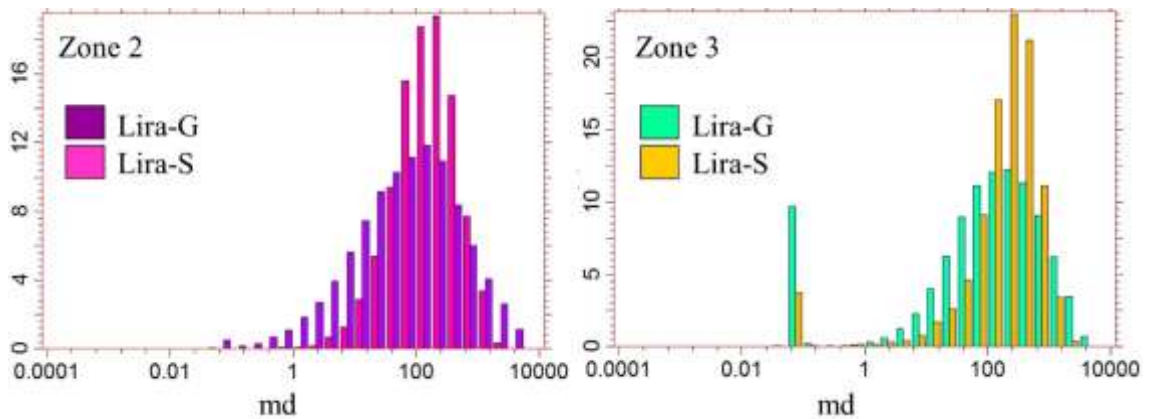


Figure 6.39 Permeability histograms comparing Lira-G and Lira-S in a region with karst influence in zones 2 and 3.

Figures 6.40 and Figure 6.41 highlight the porosity based on RT in Lira-S, as compared to Lira-G in zones 2 and 3 respectively. Figure 6.42 and Figure 6.43 compare the permeability. It is less clear to differentiate between karstic and matrix blocks in Lira-S when compared to Lira-G, although karstic block tends to reach higher property values than matrix block.

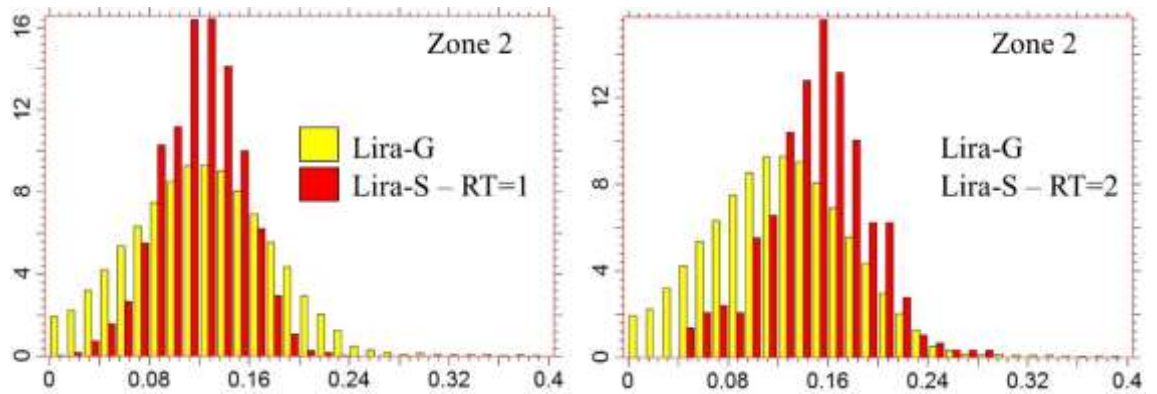


Figure 6.40 Comparison of porosity between Lira G and Lira-S RT=1 (left) and Lira-S RT=2 (right) in Zone 2.

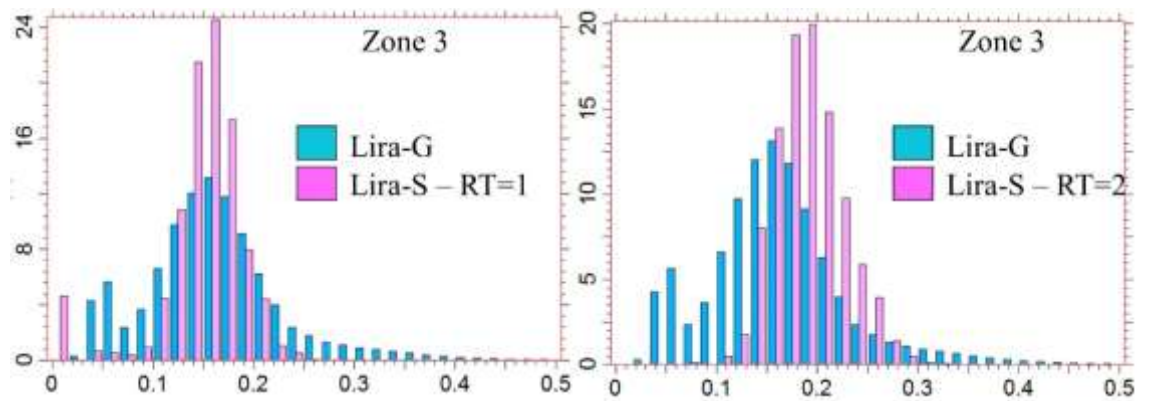


Figure 6.41 Comparison of porosity between Lira G and Lira-S RT=1 (left) and Lira-S RT=2 (right) in Zone 3.

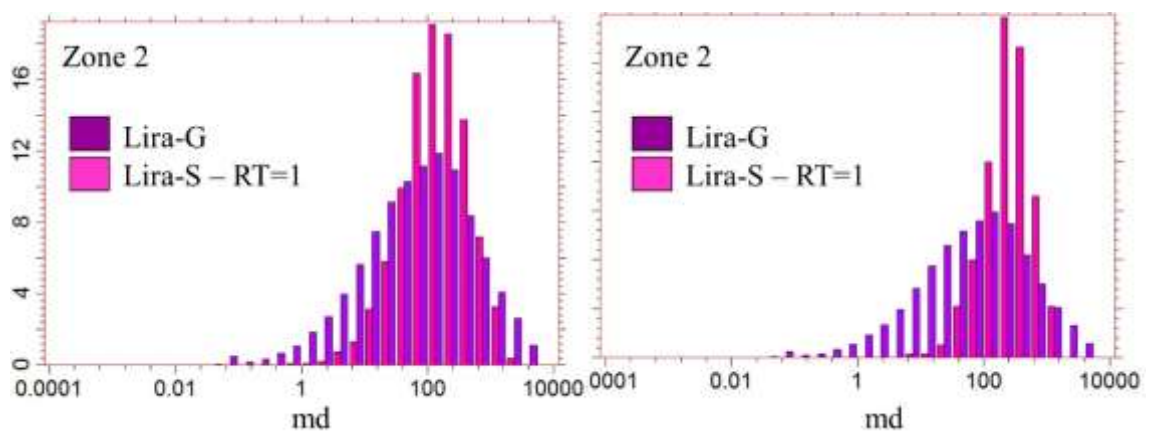


Figure 6.42 Comparison of porosity between Lira G and Lira-S RT=1 (left) and Lira-S RT=2 (right) in Zone 2.

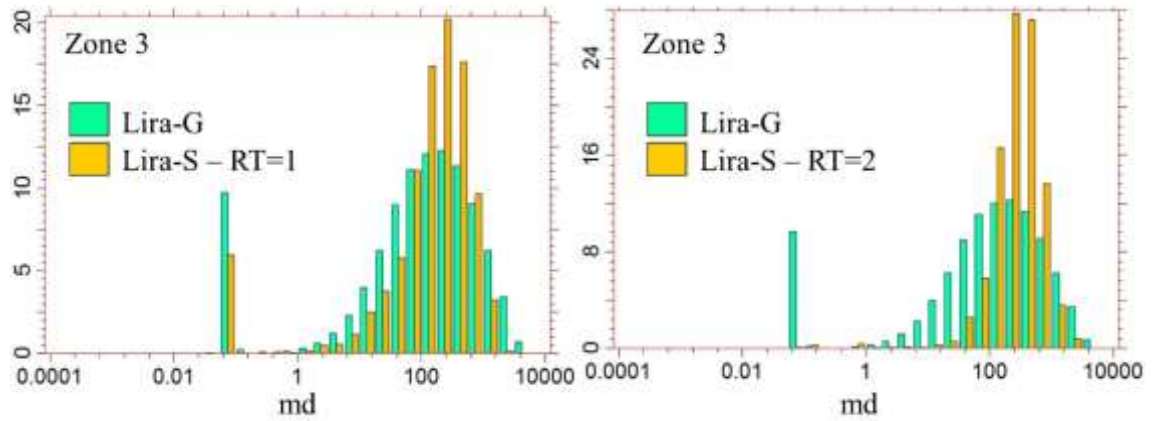


Figure 6.43 Comparison of porosity between Lira G and Lira-S RT=1 (left) and Lira-S RT=2 (right) in Zone 3.

Figure 6.44 to Figure 6.47 show the porosity, horizontal permeability, vertical permeability and NTG respectively in Lira-G and Lira-S.

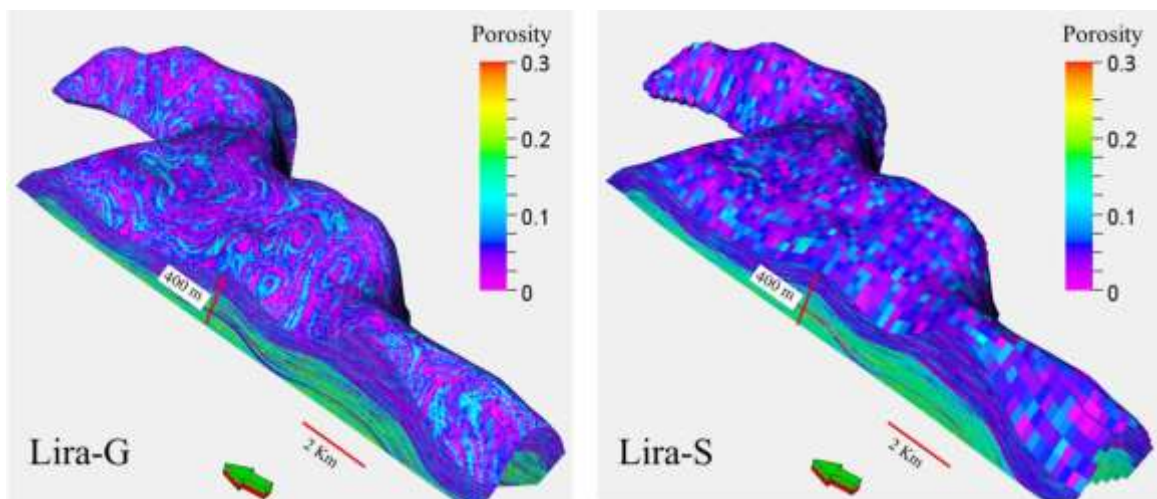


Figure 6.44 Porosity model in Lira-G and Lira-S

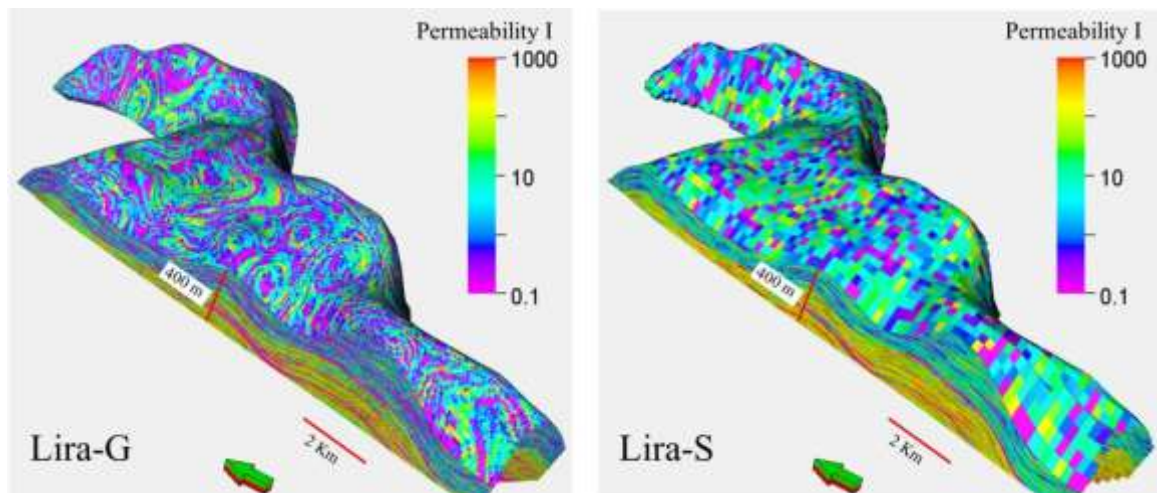


Figure 6.45 Horizontal permeability model in Lira-G and Lira-S

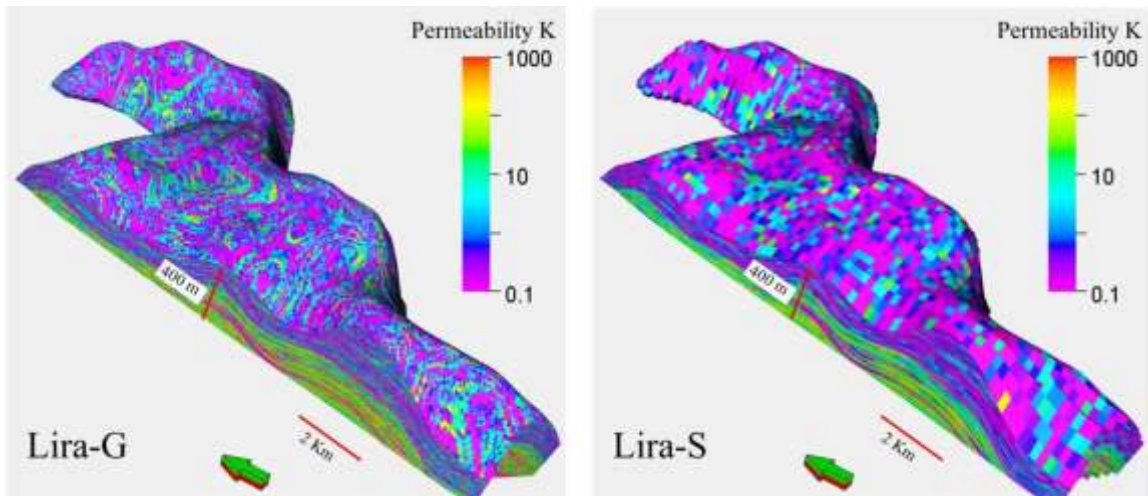


Figure 6.46 Vertical permeability model in Lira-G and Lira-S

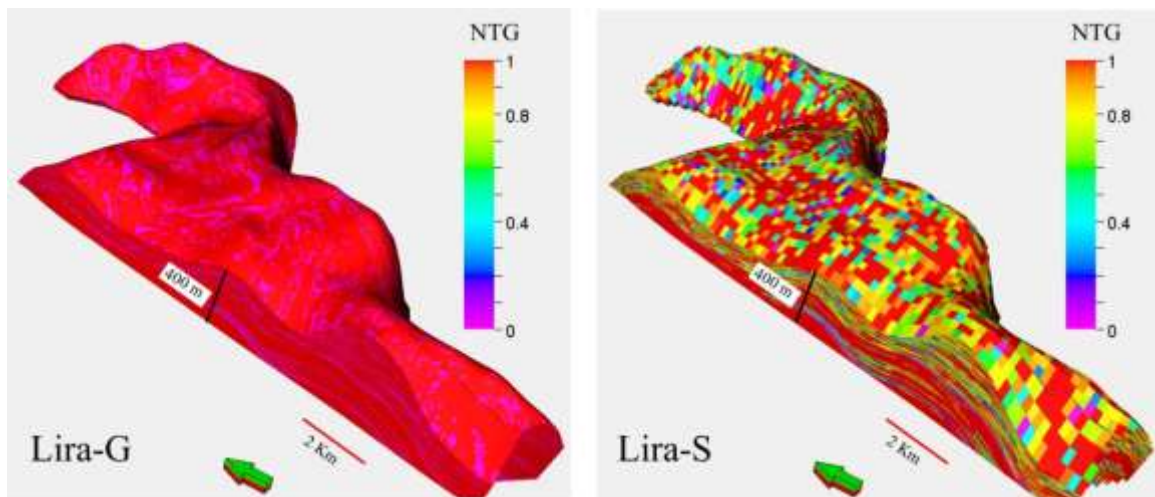


Figure 6.47 NTG model in Lira-G and Lira-S

Figure 6.48 and Figure 6.49 show the histogram comparing porosity and horizontal permeability in full field Lira-G and Lira-S respectively by zone.

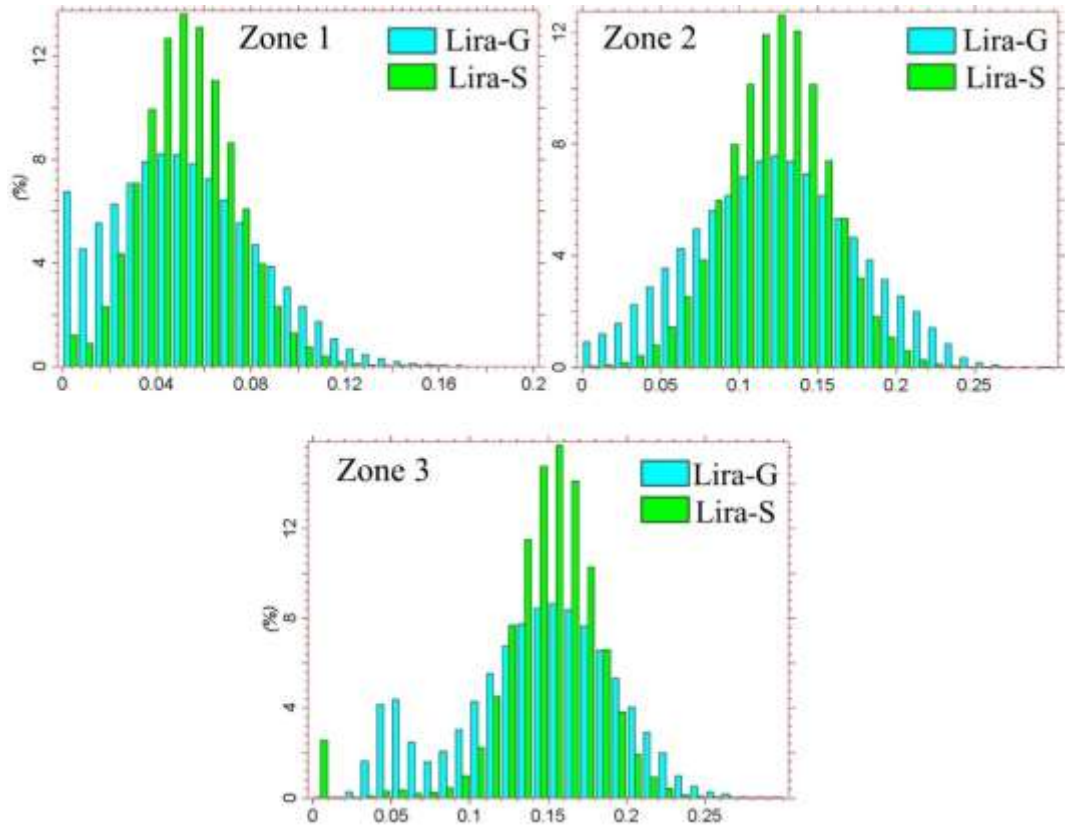


Figure 6.48 Porosity of full field Lira-G and Lira-S by zone.

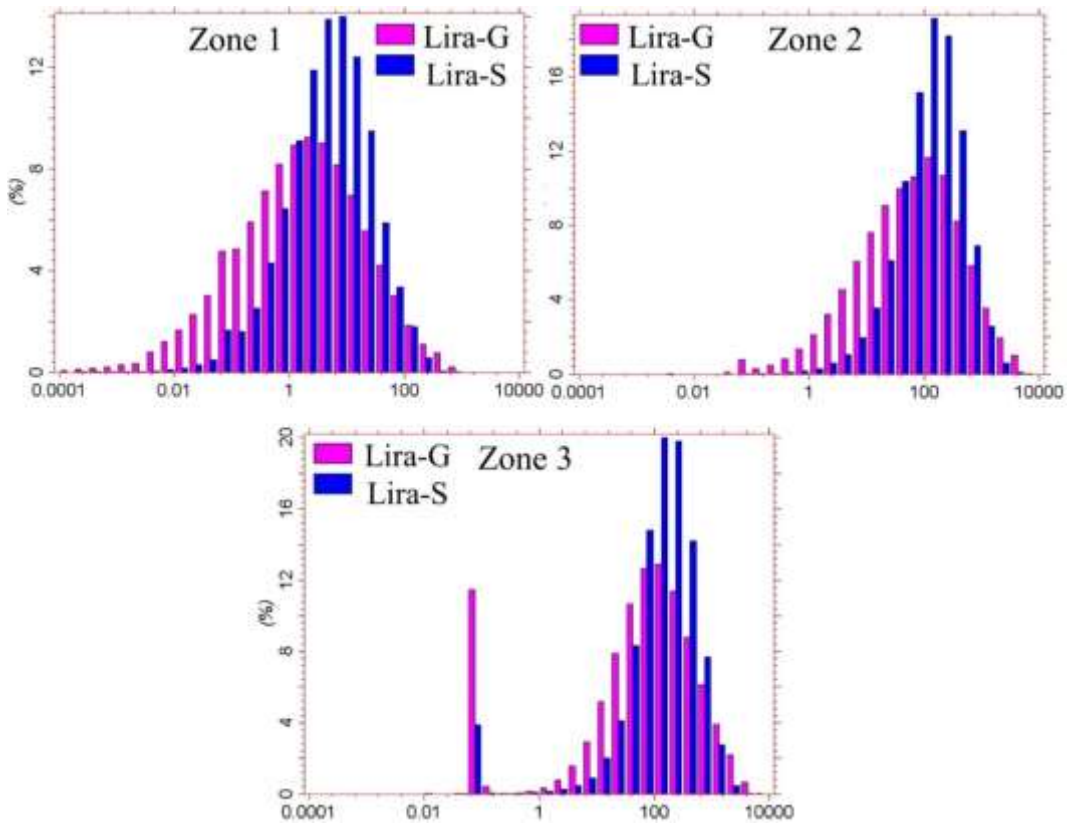


Figure 6.49 Permeability of full field Lira-G and Lira-S by zone

The pore volume in full field Lira-G and Lira-S remains almost invariable as can be seen in Table 6.2.

Table 6.2 Volume comparison between Lira-G and Lira-S

Model	Active Blocks	Pore Volume [m3]	Pore Volume % difference
Lira-G	10663599	5466107000	0.44
Lira-S	296088	5490322000	

Figure 6.50, 6.51 and 6.52 present a cross sections of Lira-S in Zone 1, Zone 2 and Zone 3, respectively. In Zones 2 and 3 the influence of the karst in the distribution of porosity, and permeability is highlighted.

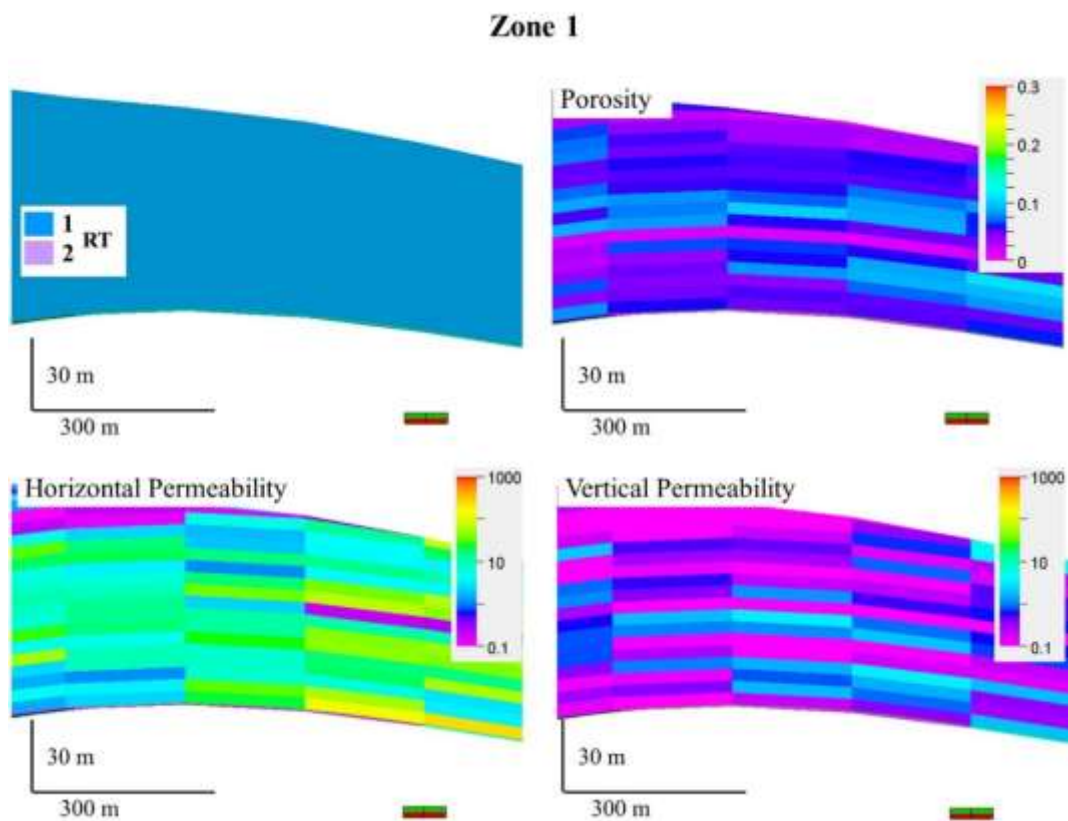


Figure 6.50 Cross section showing the RT, porosity and permeability of Lira-S in Zone 1

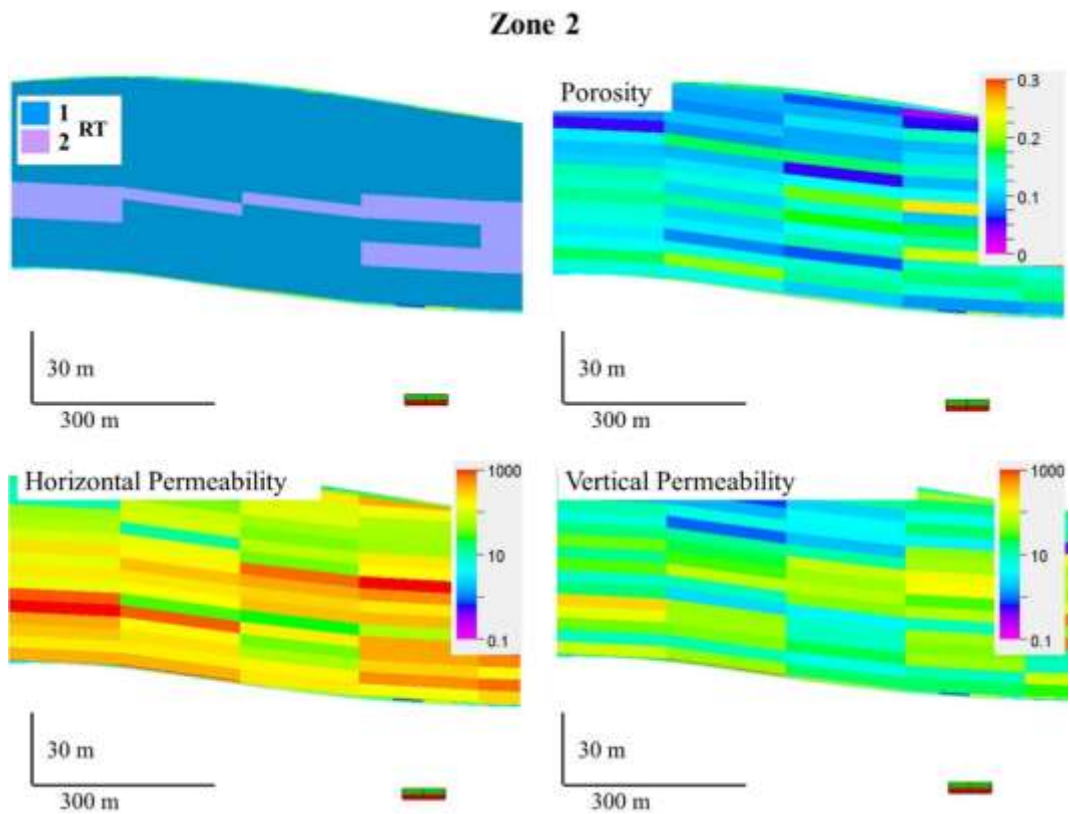


Figure 6.51 Cross section showing the RT, porosity and permeability of Lira-S in Zone 2

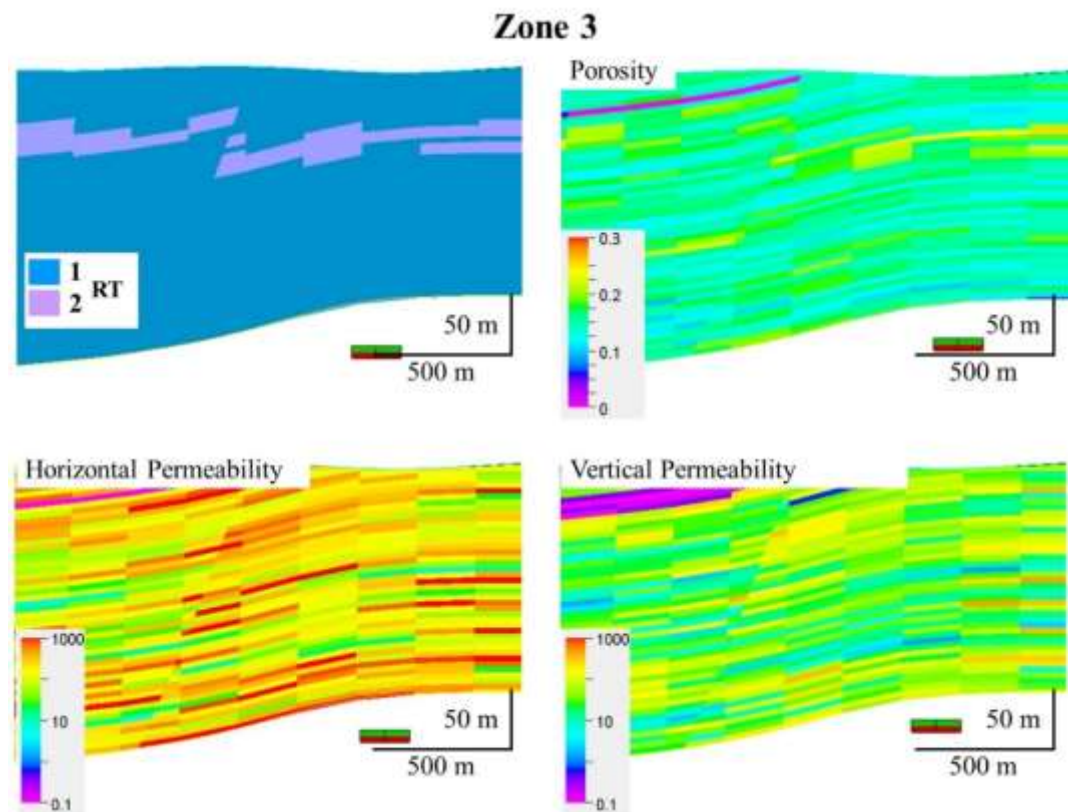


Figure 6.52 Cross section showing the RT, porosity and permeability of Lira-S in Zone 3

6.5.1 Validation of Lira-S

The first step is to verify that the porous volume in the regions taken from Lira-G and Lira-K is conserved in both models; this situation can be noted in Table 6.3.

Table 6.3 Pore volume comparison between Lira-G and Lira-S in validation regions of zones 1, 2 and 3.

Modelo	Pore Volume [m3]		
	Zone 1	Zone2	Zone3
Lira-G	36464630	68684100	99364960
Lira-S	36938150	70683990	99063840

Figure 6.53 to 6.55 compares the results obtained from the simulations in the validation zones of Lira-G and Lira-S in Zones 1, 2 and 3 respectively. The images show the adjustment obtained by using the pseudo-curves.

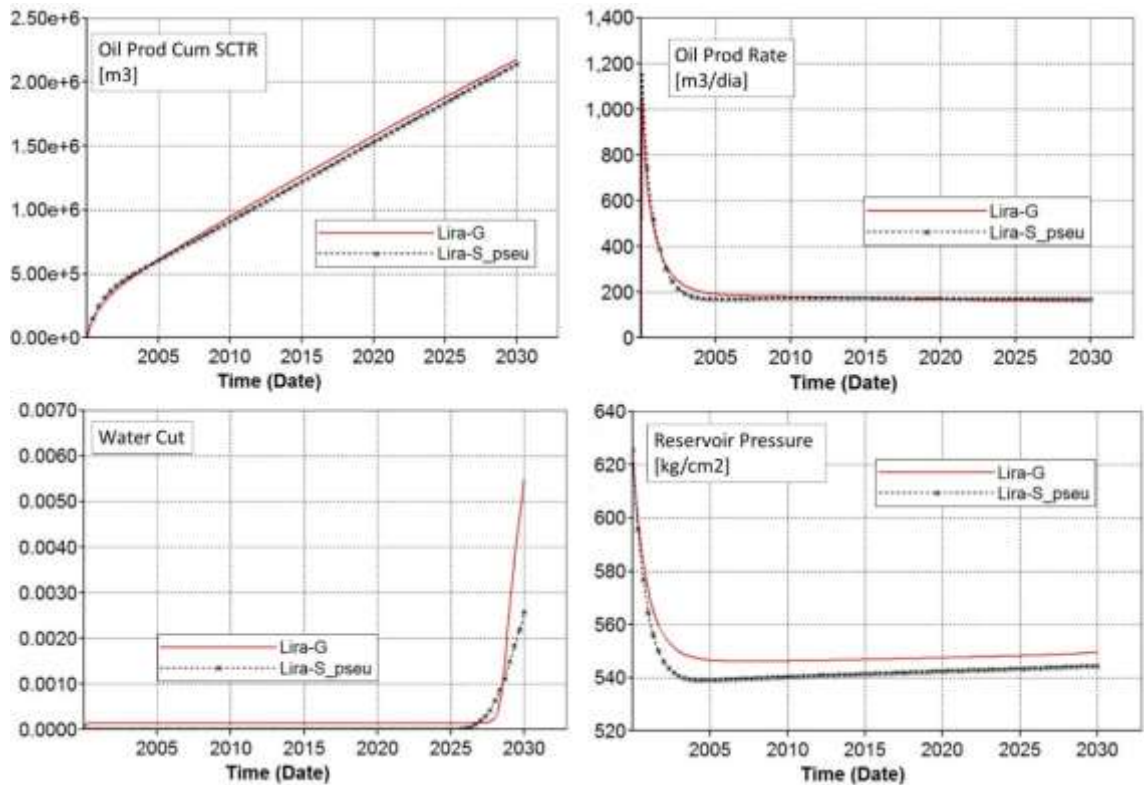


Figure 6.53 Comparison of oil production, oil production rate, water cut and reservoir pressure between Lira-G and Lira-S in Zone 1 after validation.

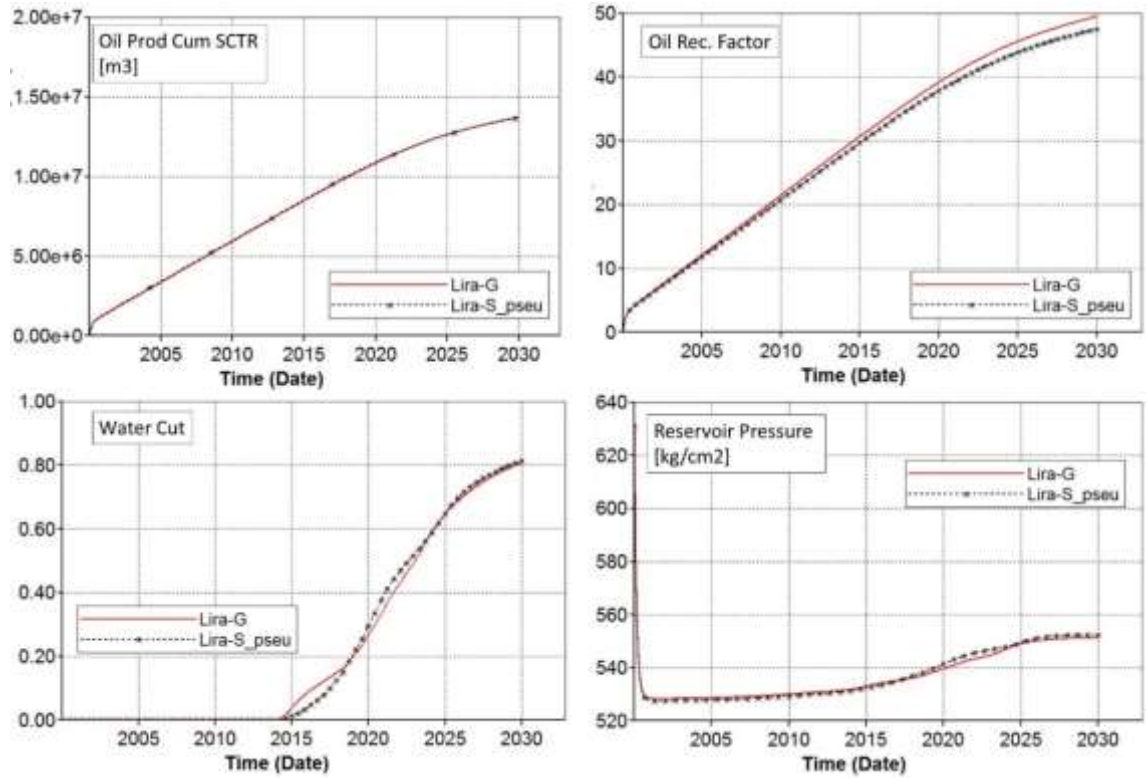


Figure 6.54 Comparison of oil production, oil recovery factor, water cut and reservoir pressure between Lira-G and Lira-S in Zone 2 after validation.

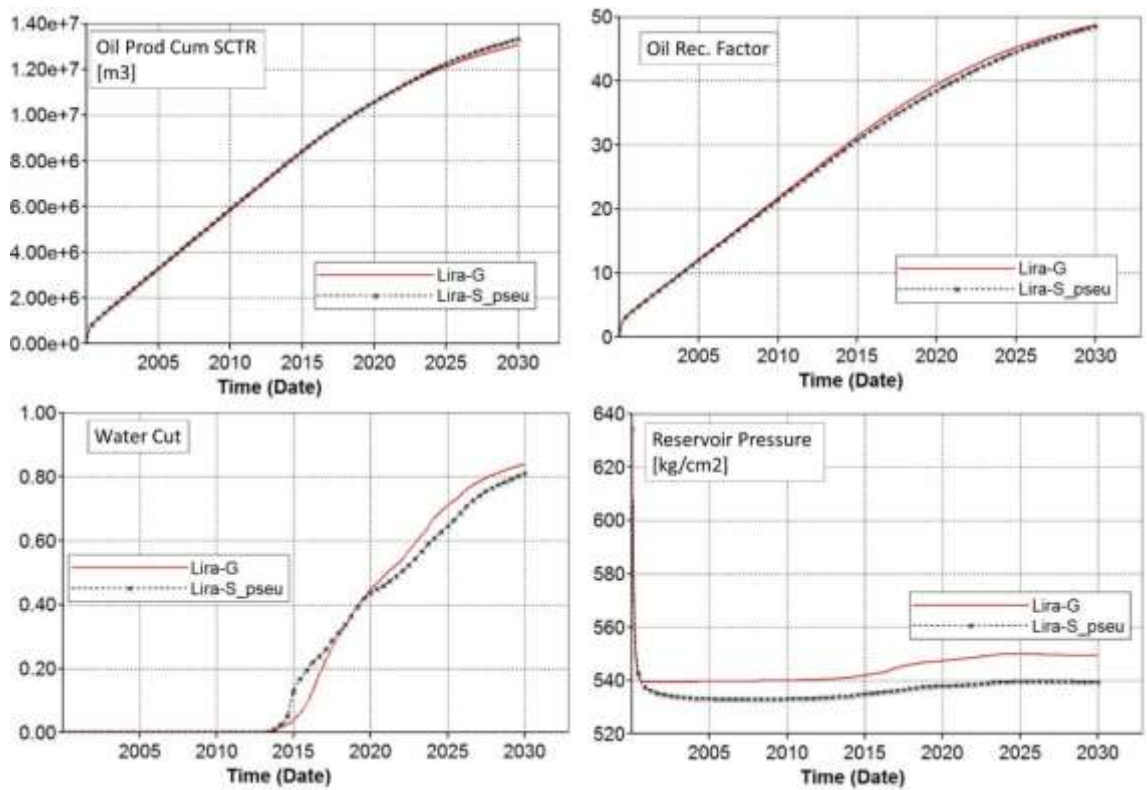


Figure 6.55 Comparison of oil production, oil recovery factor, water cut and reservoir pressure between Lira-G and Lira-S in Zone 3 after validation

A good match with respect to different reservoir parameters such as oil production, oil recovery factor, water cut, and reservoir pressure is achieved for the field in validation regions.

Figure 6.56 and Figure 6.57 show the comparison of water saturation between Lira-G and Lira-S for Zone 1 at ten and thirty years of simulation respectively, in a horizontal cut.

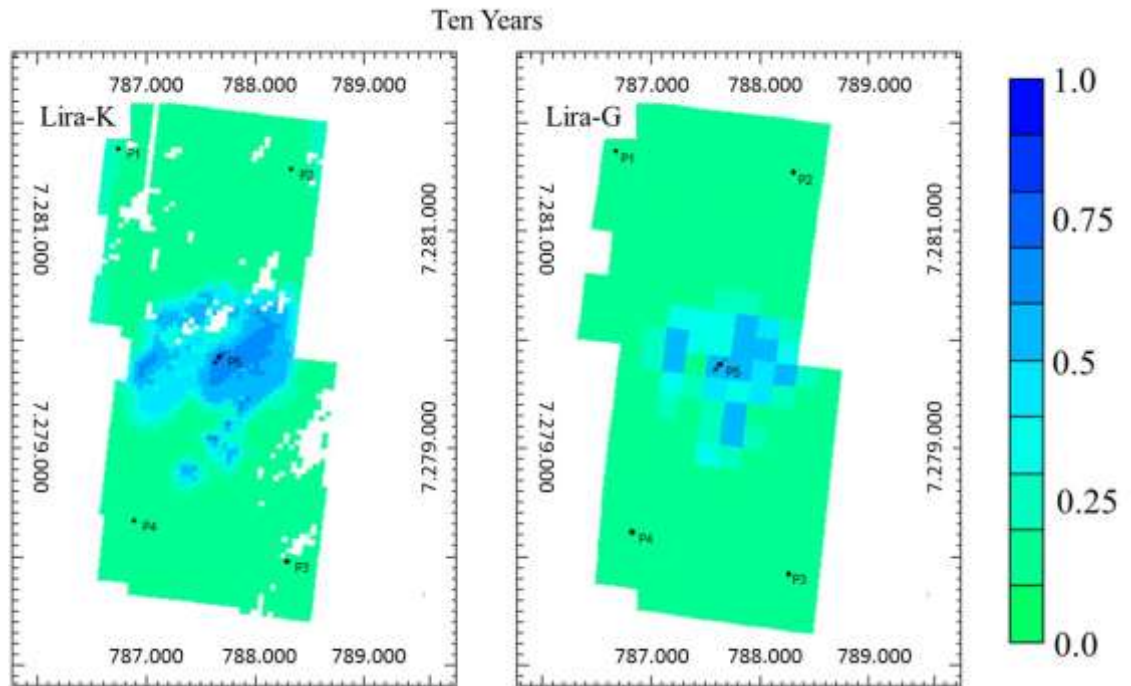


Figure 6.56 Comparison of water saturation between Lira-G and Lira-S in Zone 1 at ten years of simulation.

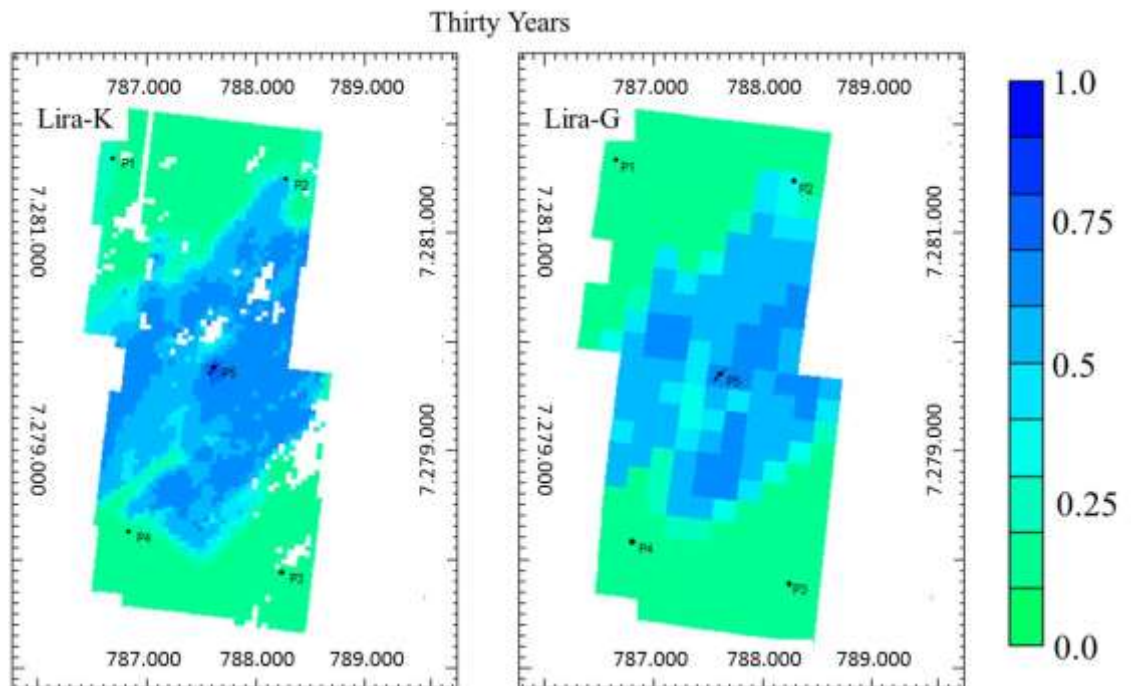


Figure 6.57 Comparison of water saturation between Lira-G and Lira-S in Zone 1 at thirty years of simulation

Figure 6.58 and Figure 6.59 show the water saturation in Lira-G and Lira-S for Zone 2 at ten and thirty years of simulation respectively, in a horizontal cut at 5260 meters depth.

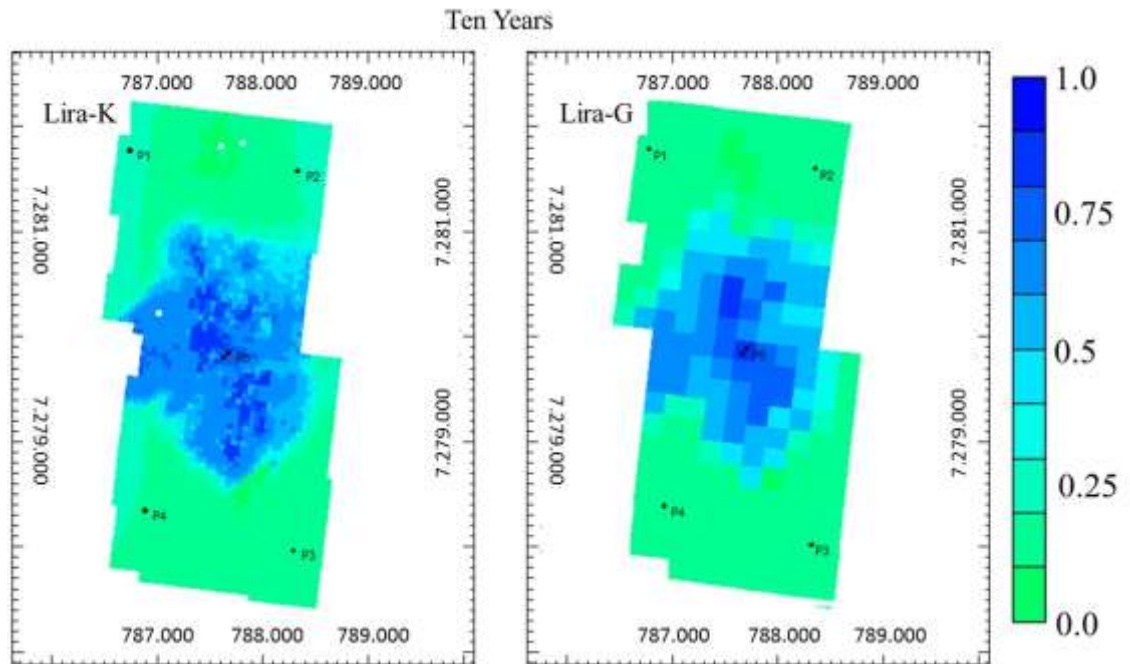


Figure 6.58 Comparison of water saturation between Lira-G and Lira-S in Zone 2 at ten years of simulation

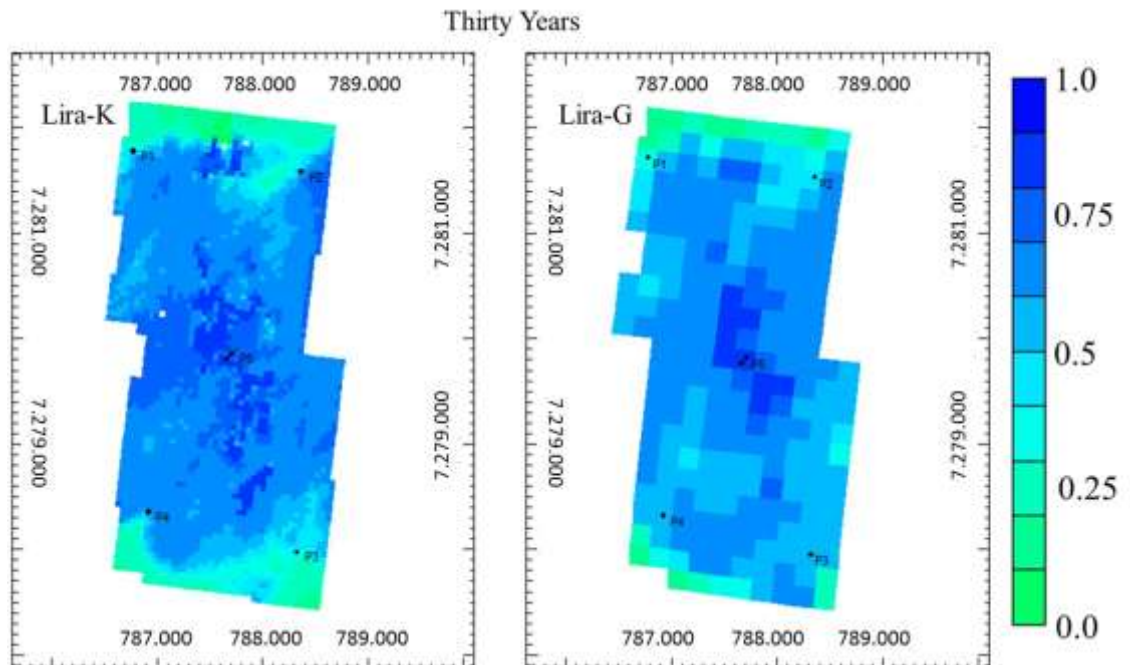


Figure 6.59 Comparison of water saturation between Lira-G and Lira-S in Zone 2 at thirty years of simulation

The maps show that the behavior of water advance is similar in both models when using adjusted curves of relative permeability. The influence of the karst can be seen in these figures.

Figure 6.60 and Figure 6.61 show the comparison of water saturation between Lira-G and Lira-S for Zone 3 at ten and thirty years of simulation, in a horizontal cut at 5360 meters depth. The influence of the karst and the similar behavior in the two models can be noticed.

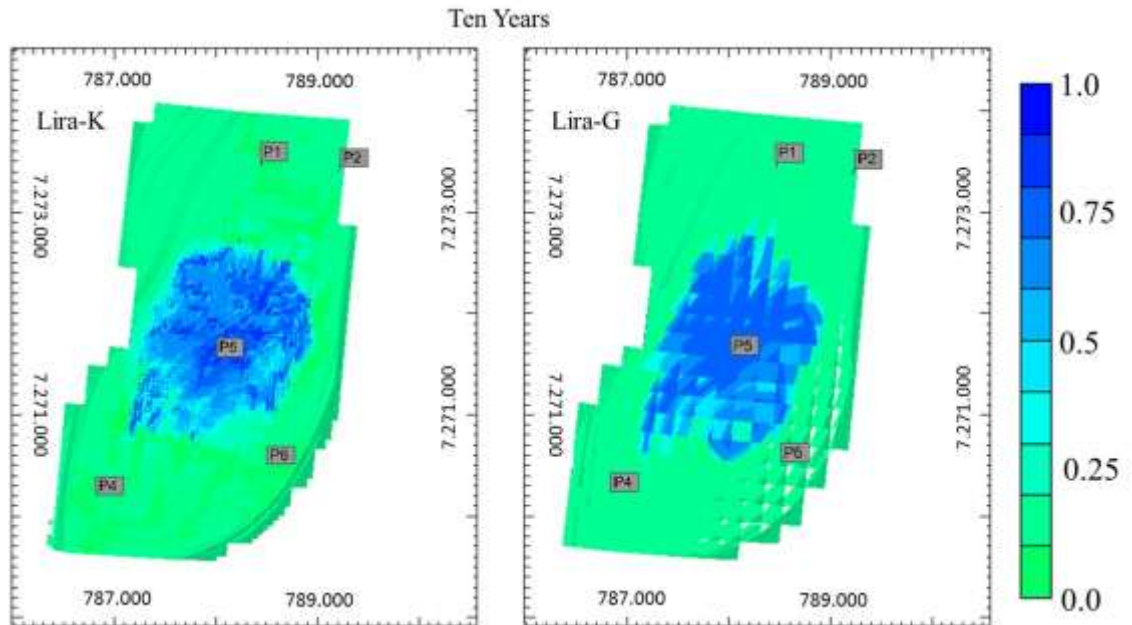


Figure 6.60 Comparison of water saturation between Lira-G and Lira-S in Zone 3 at ten years of simulation

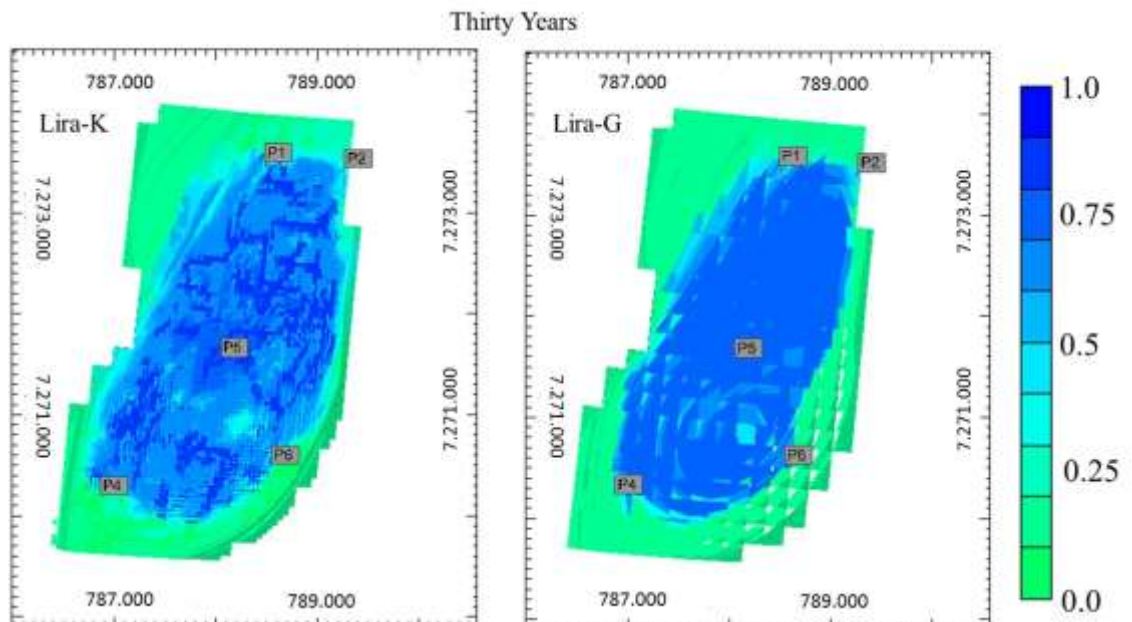


Figure 6.61 Comparison of water saturation between Lira-G and Lira-S in Zone 3 at thirty years of simulation

The validation process of Lira-S shows good dynamic matching concerning reservoir production parameters. Considering the well production parameters, it is required a local adjustment, based on a local approach of pseudo-curves and calibration of well index (Figures 6.62 to 6.65). However, these steps were not addressed in this work.

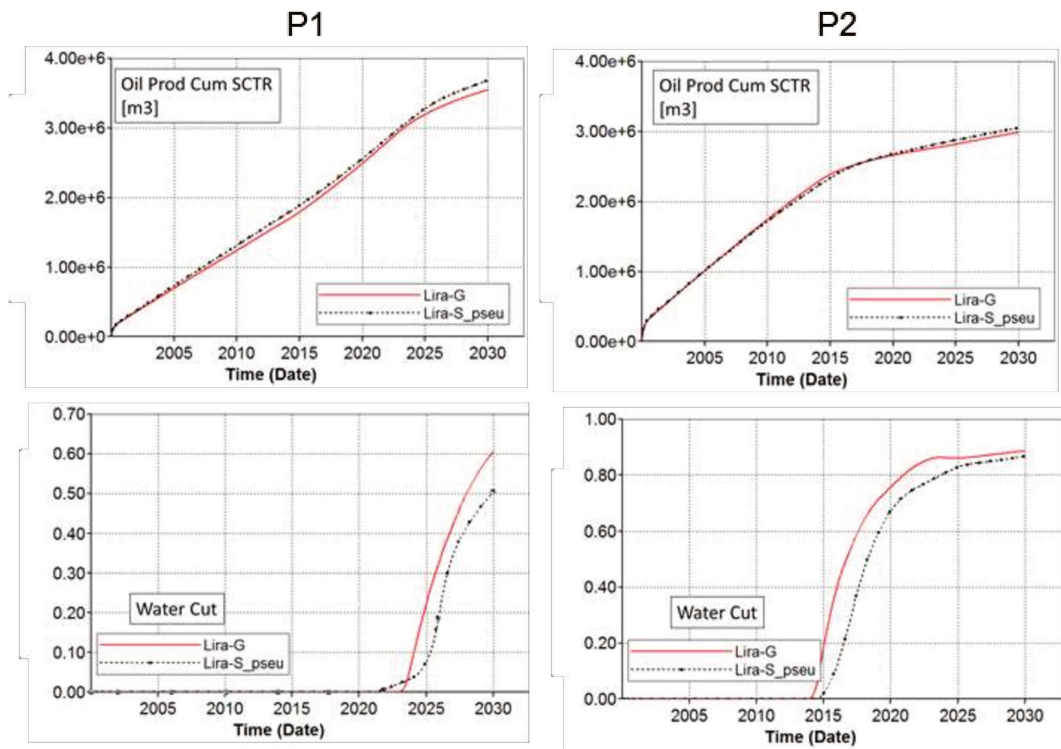


Figure 6.62 Oil production and water cut comparing production wells adjust in Lira-G and Lira-S in Zone 2 after validation.

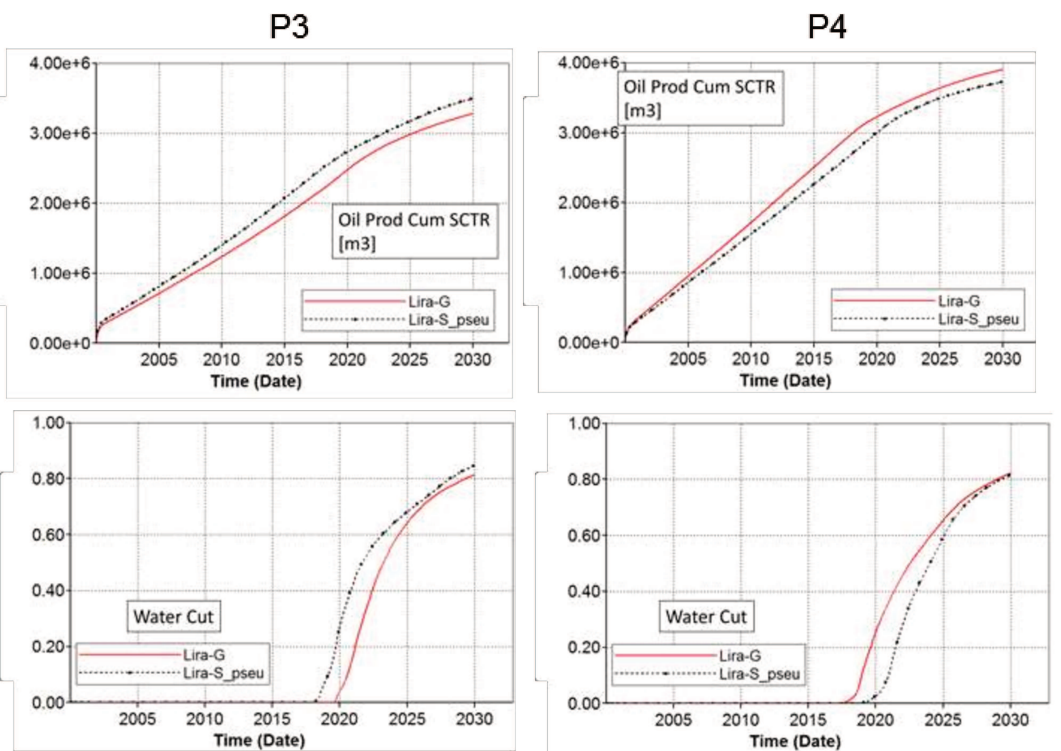


Figure 6.63 Oil production and water cut comparing production wells adjust in Lira-G and Lira-S in Zone 2 after validation.

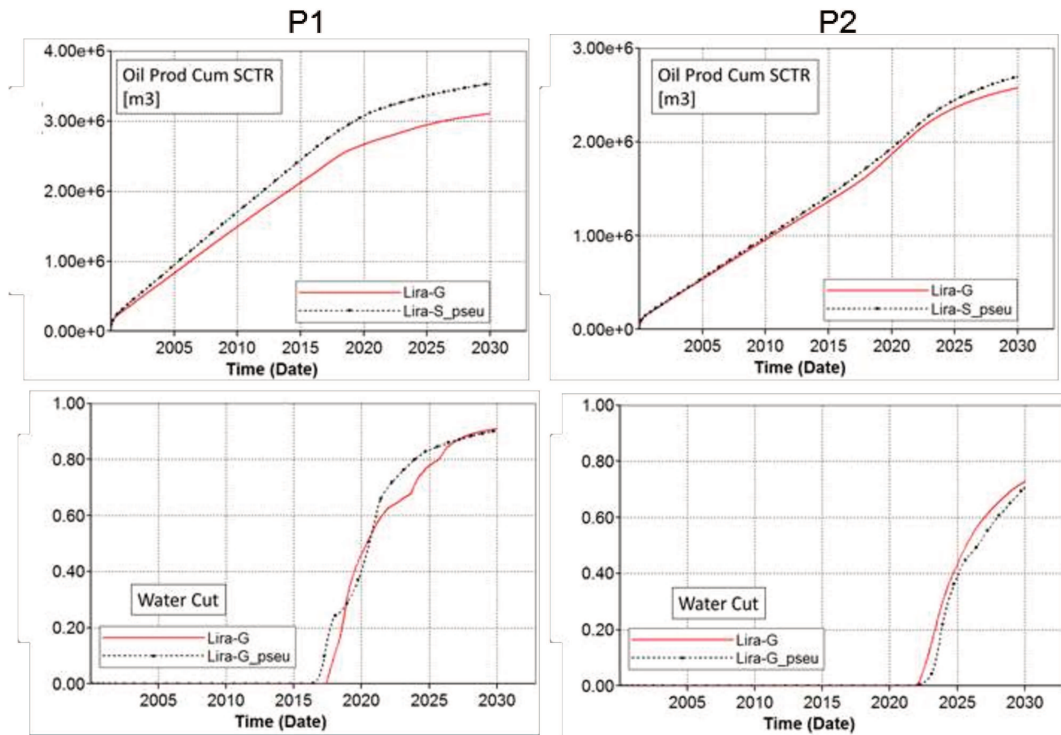


Figure 6.64 Oil production and water cut comparing production wells adjust in Lira-G and Lira-S in Zone 3 after validation.

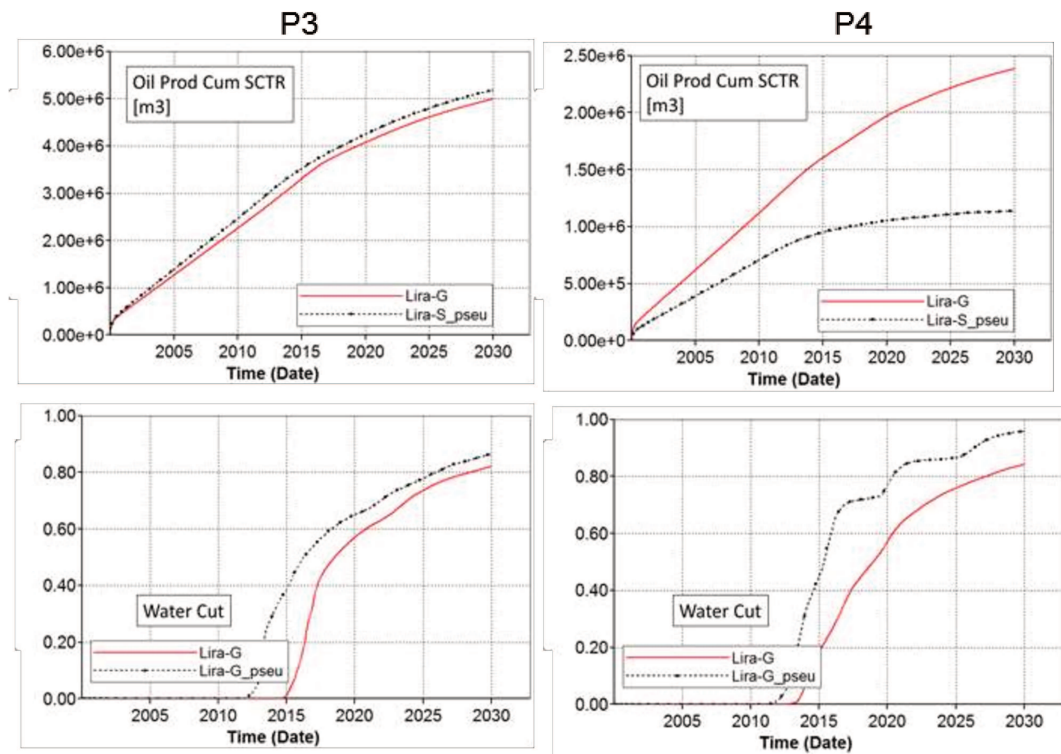


Figure 6.65 Oil production and water cut comparing production wells adjust in Lira-G and Lira-S in Zone 3 after validation.

Figure 6.66 and Figure 6.67 compare water saturation maps in Zone 2, with and without karst influence in Lira-G at ten and twenty years. Figure 6.68 and Figure 6.69 show water saturation in Lira-S in Zone 2, with and without karst influence at ten and twenty years in a horizontal cut at 5260 meters depth. In the figures is noted the influence of karst features on the dynamic behavior that creates a different distribution of water saturation when $RT = 2$ is present, and when $RT = 2$ is not present in both Lira-G and Lira-S grids.

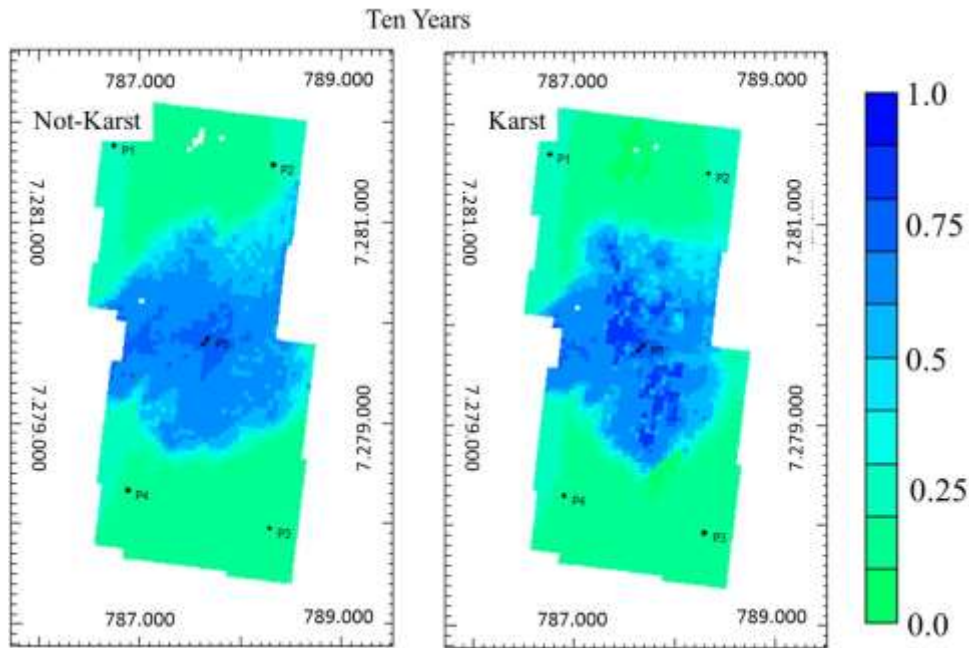


Figure 6.66 Influence of karsts features on the water advance in Lira-G, Zone 2 at ten years of simulation

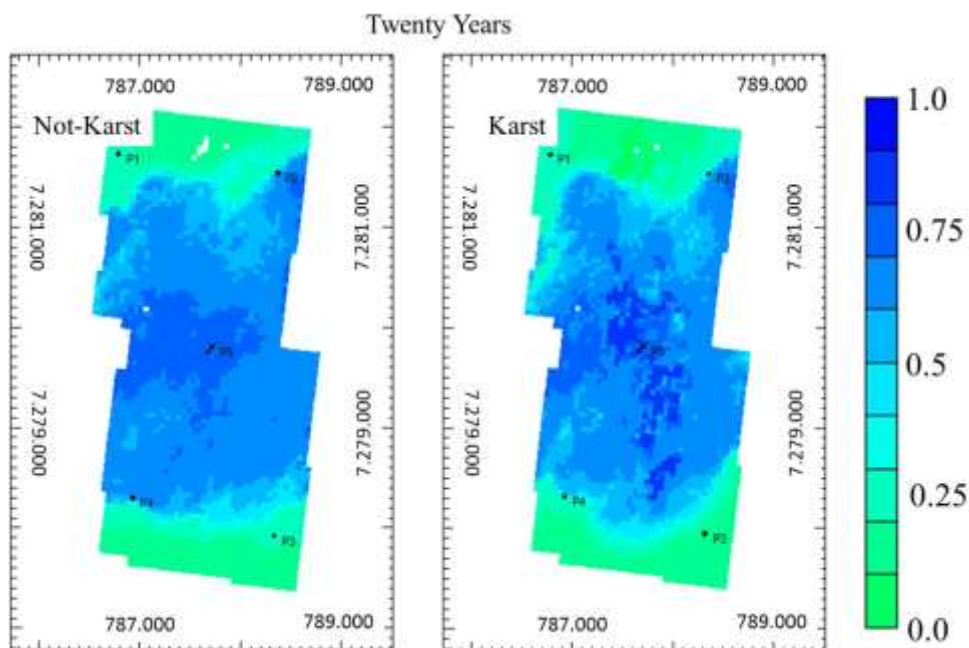


Figure 6.67 Influence of karsts features on the water advance in Lira-G, Zone 2 at twenty years of simulation

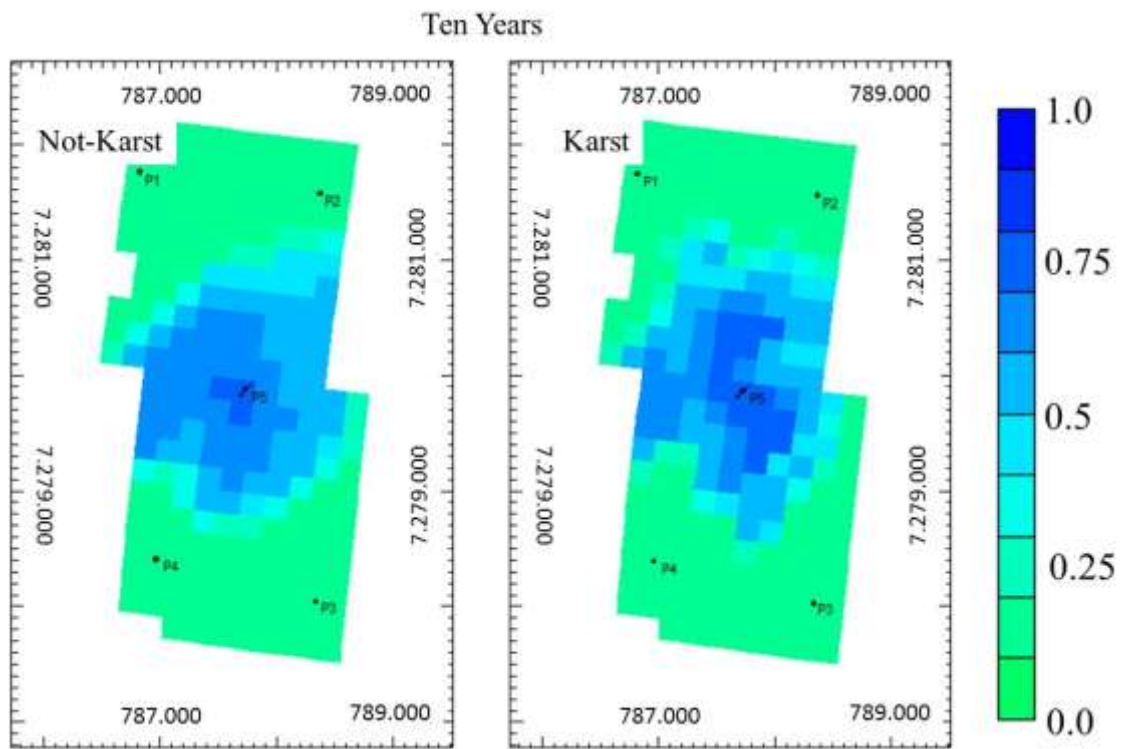


Figure 6.68 Influence of karsts features on the water advance in Lira-S, Zone 2 at ten years of simulation

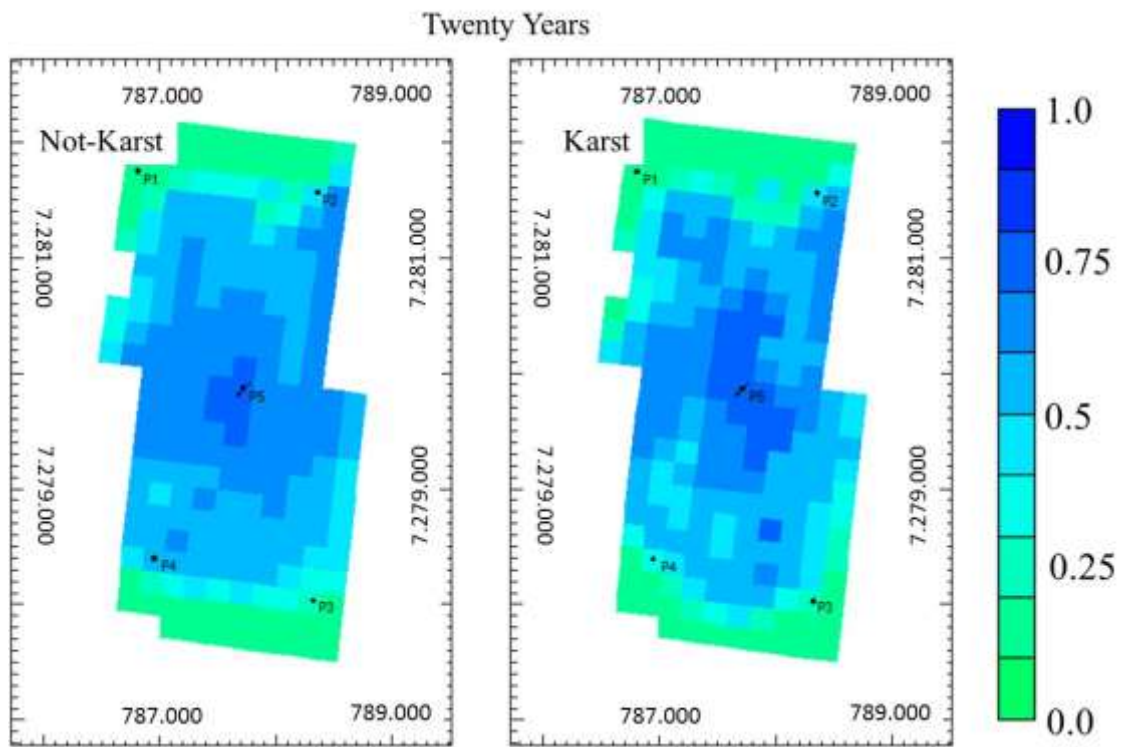


Figure 6.69 Influence of karsts features on the water advance in Lira-S, Zone 2 at thirty years of simulation

The results show the consistency of the three models after applying the multiscale approach to their development. The Lira-G and Lira-S models follow the complexity of heterogeneities presented in Lira-K, at a full field scale. The heterogeneities presented in Lira-K are identifiable in Lira-G. The matrix-karst contrast is recognizable on this scale. In Lira-S, however, this contrast is less obvious, given the order of magnitude of the block, although the trends in the distribution of static and dynamic properties remain as Lira-K.

The use of conceptual models helped in the generation of the reliable synthetic model, and the definition of reference solutions contributed to the validation of the upscale process.

Lira-K can be represented as an equivalent porous medium (single pore) given the continuity of the karst as dissolution enhanced fracture, which occupies the entire volume cell of the Lira-K model. The Lira-G and Lira S models were represented as a single porous medium adjusted by the use of pseudo-curves of properties. For the adjustment in the wells, a broader approach is necessary. The general trend in the behavior of producers presented an accepted adjustment in most of the producing wells, although others need a better adjustment. This adjustment can be addressed in future works.

The Lira -G and Lira-S models can also be represented as a double porosity model, one for each rock type. In this type of model the shape factor parameter, which conditions the exchange between the two porous media (Matrix-Karst), should be treated as an uncertainty (Medekenova et al., 2014). The analysis of this type of numerical flow model can be addressed in future works.

The Lira-G model is a deterministic model developed with the aim of being used as a reference model with known properties for further research related to oil field development and production strategy selection. However, simulation models should consider uncertainties. The uncertainty attributes include structural framework (faults, horizons), facies distribution (spatial variability, stochastic seeds), petrophysical properties (average value, spatial variability, stochastic seeds), and karstic distribution network. The critical uncertainties to karst reservoirs lie mainly in parameters related to karst volume estimates, including the determination of conduits volumes, extension and conductivity (Pauget et al., 2014, Medekenova et al., 2014). Studies like this present the opportunity to discuss decision analysis techniques and oil exploitation strategies, using deterministic and probabilistic approaches. However, in this work, we did not consider uncertainties.

7 CONCLUSIONS

The main contribution of this work is the construction of a synthetic reservoir model that represents a karstic carbonate reservoir with Brazilian pre-salt trends. This model can be used as a reference model to test (1) methodologies related to the development of geological models with limited information (managing uncertainty) and (2) comparison of approaches related to the development and management of reservoirs (ex.: upscaling procedures and production optimization strategy).

The geological model was developed by applying a multiscale approach, combining a coarser grid model where a field with Brazilian pre-salt tendencies was represented, with a finer grid model where the development of karstic features was represented. The approach integrated stages of characterization, upscaling and numerical simulation.

Lira-G and Lira-S models follow the complexity of heterogeneities presented in Lira-K, at a full field and simulation scale respectively. The heterogeneities presented in Lira-K are identifiable in Lira-G, however, in Lira-S the contrast is less obvious.

The proposed objectives were achieved carrying out the integration of critical heterogeneities at different scales in modeling and flow simulation. Main remarks about procedure:

- Geomodeling of background facies based on log data from two wells in a geological resolution grid and a cell size of 50 x 50 x 2 meters, called Lira-M. This model presents a similar petrophysical behavior to the pre-salt fields. The use of conceptual models, represented by the distribution of facies, proved useful when populating the model, limited by the information of two wells;
- Geomodeling of karst features in a finer resolution grid with a cell size of 10 x 10 x 1 meters, called Lira-K. For this model, we used conceptual models, represented by the dimensions and main orientations of the karsts;
- Upscaling of Lira-K and integration with Lira-M into a full geological model, called Lira-G, with a geological resolution grid of 50 x 50 x 2 meters. This model represents a scenario of a pre-salt field with the development of karstic features. The definition of reference solutions contributed to the validation of the upscaling process;
- Upscaling of Lira-G to the coarser grid Lira-S, to be used in flow simulation. The use of a reference solution assisted the validation of the upscaling process;

- The validation and adjustment processes portray the influence of karst features in recovery and dynamic behavior. Furthermore, based on pseudo-curves and using a reference response, it was possible to match the dynamic production data from flow simulation between the models at different scales. Water saturation maps and field parameters (oil production, water cut) were used to validate and adjust the upscaling matching procedure.

This work contributed to a hierarchical upscaling methodology to construct a karstic geological model, integrating modeling and reservoir simulation.

Additional suggestions to guide future works regarding the modeling and simulation of heterogeneities of karst features at different scales are:

- The Lira -G and Lira-S models can be represented as a double porosity model. In this type of model the shape factor parameter, which conditions the exchange between matrix and Karst should be treated as an uncertainty.
- For the adjustment in wells, a broader approach regarding well parameters is suggested.
- Based on Lira-G can be created simulation models under uncertainties. The uncertainty attributes to be analyzed include structural framework, facies distribution, and petrophysical properties and, karstic distribution network. Critical uncertainties to karst reservoirs are mainly related to karst volume estimate, distribution, extension, and conductivity.

The proposed Lira model presents an opportunity to be used as a *benchmark* to evaluate and compare different methodologies regarding modeling, upscaling procedures and reservoir numerical simulation, and to discuss decision analysis techniques and oil exploitation strategies, using deterministic and probabilistic approaches.

REFERENCES

- Avansi, G., and Schiozer, D. (2015) UNISIM-I: Synthetic model for reservoir development and management applications, *International journal of modeling and simulation for the petroleum industry* **9**, 1, 21-30.
- Beasley, C., Fiduk, J., Bize, E., Boyd, A., Frydman, M., Zerilli, A., Dribus, J., Moreira, J., Capeleiro, A. (2010). Brazil's Presalt play, *Schlumberger Oilfield Review* **22**,3.
- Biver, P., Longis, Ch., Penna, E., Ovsyannikov, A. (2012). Modeling uncertainties in carbonate karstic reservoirs: presentation of a tool and its application to a real field case in Russia. SPE 160721.
- Bourbiaux, B. (2010) Fractured reservoir simulation: a challenging and rewarding issue, *Oil & gas Science and technology – Rev. IFP* **65**, 2, 227-238.
- Carneiro, M., Bezerra, F., Silva, C., Maia, R., Cazarin, C. (2015) Controle estrutural do sistema cárstico epigenético na formação Jandaíra, Bacia Potiguar, *Geociências - UNESP*, **34**, 2, 199-209.
- Cazarin, C., Bezerra, F., Ennes-Silva, R., Balsamo, F., Auler, A. (2016) Using analogue hypogene karst system to understand the pre-salt carbonate reservoirs Offshore Brazil. *AAPG 2016 international conference and exhibition*. Cancun.
- Choquette, P., Pray, L. (1970) Geologic nomenclature and classification of porosity in sedimentary carbonates. *The American association of petroleum geologist bulletin*, **54**, 2, 207-250.
- Chang, H., Kowsmann, R., Ferreira, A., Bender, A. (1992) Tectonics and stratigraphy of the East Brazil Rift system: an overview, *Tectonophysics* **213**, 97-138.
- Correia, M. (2014). Representação de reservatórios carbonáticos naturalmente fraturados em simulação de reservatórios. Faculdade de Engenharia Mecânica, Universidade Estadual de Campinas, Tese (Doutorado), 185 p.
- Correia, M., Maschio, C., Schiozer, D (2015) Integration of multiscale carbonate reservoir heterogeneities in reservoir simulation, *Journal of petroleum science and engineering* **131**, 34–50.
- Correia, M., Hohendorff, J., Gaspar, A., Schiozer, D. (2015) UNISIM-II D: Benchmark case proposal Based on a carbonate reservoir, SPE-177140-MS.
- Curtis, A. (2015) Multiscale reservoir characterization from pore scale to simulation scale: concepts and workflows. SPE-175560-MS

- Dunham, J.R (1962) Classification of carbonate rocks according to depositional texture. In, W.E. Ham (Ed), Classification of carbonate rocks, a symposium. *American association of petroleum geologist*. 108-121.
- Embry, A.F.,Klovan, J.E (1971). A late Devonian reef tract on Northeastern Banks Island. *NWT: Canadian petroleum geology bulletin*, **19**, 730-781.
- Fernandes, A., Medeiros, W., Bezerra, F., Oliveira, J., Cazarin, C. (2014). GPR investigation of karst guided by comparison with outcrop and unmanned aerial vehicle imagery. *Journal of applied geophysics* **112**, 268 – 278.
- Folk, R.L (1962) Spectral subdivision of limestones types. In, W.E. Ham (Ed), Classification of carbonate Rocks. *AAPG memoir No 1, Tulsa, OK*. 62-84.
- Gaffney, Cline and associates (2010). *Review and evaluation of ten selected discoveries and prospects in the pre-salt play of the deepwater Santos Basin*, Report.
- Gale, L. E. (1982) Assessing the permeability characteristics of fractured rock. *Geological Society of America*, **189**, 163-181.
- Gaspar, A., Avansi, G., Santos, A., Hohendorff J., Schiozer, D (2015). UNISIM-I-D: Benchmark studies for oil field development and production strategy selection. *International journal of modeling and simulation for the petroleum industry*, **9**, 1, 47-55.
- Jahnert, R., and Collins, L. (2011) Significance of subtidal microbial deposits in Shark Bay, Australia. *Marine Geology* **286**, 106-108.
- Jahnert, R., and Collins, L. (2012). Characteristic, distribution and morphogenesis of subtidal microbial systems in Shark Bay, Australia, *Marine Geology* **303-306**, 115 – 136.
- Jones, G. (2015) Flow-based effective properties of sub-seismic karst. SPE-172648-MS.
- Klimchouk, A., Auler, A., Bezerra, F., Cazarin, C. (2016) Hypogenic origin, geologic controls and functional organization of a giant cave system in Precambrian carbonates, Brazil. *Geomorphology* **253**, 385-405.
- Lipinski, C., Franseen, E., Goldstein, R. (2013). Reservoir analog model for oolite-microbialite sequences, Miocene terminal carbonate complex, Spain, *AAPG bulletin* **97**, 11, 2035 – 2057.
- Loucks, R. (1999) Paleocave carbonate reservoirs: origins, burial-depth modifications, spatial complexity and reservoir implications. *AAPG bulletin*, **83**, 11, 1795-1834.
- Loucks, R. (2001) Modern analogs for paleocave sediment fills and their importance in identifying paleocave reservoirs. *Gulf coast association of geological society's transactions* **46**, 195-206.
- Lucia, J. (2007). *Carbonate Reservoir Characterization*. New York: Springer.

Mann, J. (2013). The Santos Basin Brazil: unlocking the Pre-Salt potential. Broadband technology: new benefits for presalt exploration. *Geo Expro* 2013.

Medekenova, A., and Jones, G. (2014) Characterization and modelling challenges associated with fracture and karst (non-matrix) in the margin area of a carbonate reservoir. SPE-172275-MS.

Mikes, D., Barzandji, O., Bruining, J., Geel, C (2006) Upscaling of small-scale heterogeneities to flow units for reservoir modeling., *Marine and petroleum geology* **23**, 931–942.

Milani, E., Rangel, H., Bueno, G., Stica, J., Winter, W., Caixeta, José., Pessoa Neto, O. (2007). Bacias sedimentares brasileiras – Cartas estratigráficas. *Boletim de geociencias – Petrobras*, **15**, 2, 138 – 208.

Moreira, J., C Madeira, J., Machado, M (2007) Bacia de Santos, *Boletim de Geociencias Petrobras* **15**, 2, 531-549.

Muniz, M., and Bosence, D. (2015) Pre-salt microbialites from the Campos basin (offshore Brazil): image log facies, facies models and cyclicity in lacustrine carbonates. *Microbial carbonates in space and time: implications for global exploration and production* **418**.

Muniz, M., and Bosence, D. (2016) Tectono-stratigraphy evolution of the continental rift Pre-salt carbonates in southern Campos basin, *Brazil. Rio Oil and gas. Expo and conference*, Rio de Janeiro.

Neillo, V., Pauget, L., Neumann, C. (2014) Integrated workflow to tackle heterogeneous karst dominated reservoirs: Kharyaga example. SPE 171204-MS.

Nelson, R. (2007). *Geologic analysis of naturally fractures reservoirs*. Butterworth-Heinemann:

Petersohn, E., Abelha, M., Pedrosa, L. (2013) *Brasil Pre-Sal 1. Libra – Avaliação geológica e diretrizes ambientais*. Brazilian National oil and gas biofuels agency - ANP.

Pauget, L., Pignot, B., Dzhafarov, D. (2014). Tackling of a complex carbonate field through a dedicated history-match scheme and software. SPE 171227-MS.

Riding, R. (2000) Structure and composition of organic reef and carbonate mud mounds: concepts and categories. *Earth science reviews*, **58**, 163-231.

Ringrose, P., and Bentley, M. (2015) *Reservoir model design. A practitioner's guide*. Springer. New York.

Salamoni, G., Spadini, A., Barros, A., Sombra, C., Zambonato, E., Costa, L., Arienti, L., Marques, M., Blauth, M., Pitella, M., Matsuda, N., Carramal, N., Moretti, P., D'Avila, R.,

Schiffer, R., Tonietto, S., Couto, S., Silva, V., Winter, W. (2010) Carbonate rock classification applied to Brazilian sedimentary basins. *Boletim de Geociências Petrobras* **18**, 1, 9-29.

Schlumberger. (2015). *Petrel Help Center*. Petrel software.

Simms, M. J. (2005) Karst and paleokarst. *Encyclopedia of Geology*, Elsevier, Belfast, pp 678-687.

Suosaari, E., Reid, R., Playford, P., Foster, J., Stolz, J., Casaburi, G., Eberli, G. (2016) New multiscale perspectives on the stromatolites of Shark Bay, Western Australia. *Nature Scientific reports*. doi:10.1038/srep20557.

Strijker, G., Bertotti, G., Luthi, S (2012) Multiscale fracture network analysis from an outcrop analogue: a case study from the Cambro-Ordovician clastic succession in Petra, Jordan. *Marine and Petroleum Geology* **38**, 104–116.

Thompson, D., Stilwell, J., and Hall, M. (2015) Lacustrine carbonate reservoirs from Early Cretaceous rift lakes of western Gondwana: Pre-Salt coquinas of Brazil and West Africa. *Gondwana research* **28**, 26-51.

Trice, R. (2005) Challenges and insights in optimizing oil production from Middle East mega karst reservoirs. SPE 93679.

Xinbian, L. (2014). An integrated approach to carbonate karstic reservoir characterization and its application to a field case in the Tarim Basin. *International petroleum technology conference*, Doha.